Dissertation

# STRUCTURAL HEALTH ASSESSMENT FOR ASR-DETERIORATED PC GIRDERS USING STATIC AND DYNAMIC EXAMINATIONS

Graduate School of
Natural Science & Technology
Kanazawa University

Division of Environmental Design

Student ID No.: 1624052012

Name: Ha Minh Tuan

Chief advisor: Professor Fukada Saiji

# Contents

## Figures

## Tables

# Abstract

For years, alkali-silica reaction (ASR), more commonly known as "concrete cancer," caused severe degradation in many civil engineering structures. The development of a damage identification method plays a significant part in determining the health of a structure affected by ASR. With the aim of contributing to efficient structural health monitoring approaches, the present study attempts to develop an evaluation approach that employs only displacement data for recognizing structural damage. The method is based on the correlation between structural damage and variations in measured responses. Two new damage indicators—displacement assurance criterion (DAC) and displacement based index (DBI)—are introduced and employed in numerous scenarios to determine damage properties. Parametric studies performed by a finite-element analysis showed that DAC could properly indicate the occurrence of degradation in structures and DBI could be utilized as a suitable pointer for damage localization. Regarding actual examinations, this study constructed three full-size prestressed concrete (PC) girders from the high-early-strength Portland cement and reactive aggregates, and then exposed them to outdoor environmental conditions. Two of the specimens were affected by the ASR whereas the third one was maintained at an inactive state by suppressing the acceleration of the ASR using the fly ash. Destructive loading tests were conducted on the PC girders to evaluate the feasibility of DAC approach on damage detection by analyzing the displacement curves obtained from the experiments. From the obtained results of the numerical and experimental methods, this study proposes a threshold of DAC index for the sound structure. If a structure performs a higher value of DAC than the threshold, it can be judged as safety structure. Conversely, the system will give warnings about the health of that structure. For long-term prospects, further studies about DAC need to be implemented in practical cases in order to obtain the suitable DAC threshold value for each kind of structure. Besides, structural responses have been used as inputs in the evaluation procedures of civil structures for many years. Apart from the degradation of a structure itself, variations in the environmental conditions affect its properties. For adequate maintenance, it is important to quantify the environment-induced changes and discriminate them from the effects due to damage. Therefore, this study also aims to present preliminary considerations for estimating the long-term behavior of ASR-affected structures and attempts to proposed recommendations about measurement noise when using structure responses as input for structural damage detection. As lab-scale efforts, this study investigated the combined effect of the changes in the environmental conditions and the ASR-induced deteriorations on the dynamic and static responses of the three PC girders, which were periodically tested for one and a half years. It was found that when the temperature and humidity increased, the frequencies and damping ratios decreased in proportion. However, no apparent variation in the mode shapes could be identified. Besides, the ambient temperature gradient

strongly affected the changes in the vertical movement of the girders. All values measured from displacement meters have positive correlations with the ambient temperature. In other words, the amplitude of the camber increased with respect to the growth in the ambient temperature. These outcomes should be considered in structural damage detection using changes in structural responses in practice because the environmental conditions might cause unexpected errors in measured responses in the measurement field.

# Chapter | 1

# Introduction

## 1.1 General Background

Structural Health Monitoring (SHM) aims to provide, at every moment during the life of a structure, a diagnosis of the soundness. The performance of the structure must remain in the safety region specified in the design, although this can be varied by normal aging due to usage, by the effect of the environment, and by unforeseen situations. Routine examinations and degradation estimates help to provide valuable information for SHM. Furthermore, early detection, timely maintenance, and recovery works can enhance the lifetime of a structure and prevent overall failure, guaranteeing its structural safety and serviceability with minimum cost. Therefore, the development of a damage identification method performs a significant role in determining the health of a structure. For instance, seawater, deicing salts, and salty environments cause grave consequences, without warning, in bridges of coastal areas. Besides, alkali-silica reaction (ASR) caused severe degradations in many civil engineering structures over the world [1]. In Japan, reactive aggregates are widely distributed. Especially, andesite is widespread in the Hokuriku region, which causes ASR degradation in concrete structures (see **Fig. 1.1**). Since the replacement of all structures deteriorated by ASR is almost impossible, quantitative and easily operated indicators should be established to evaluate the current status of a structure, before destruction occurs. Rytter suggested three levels in damage identification: the appearance of deterioration, the position of internal damage, and the amount of damage in terms of stiffness loss [2]. In other words, the main aim of a damage detection method is to identify occurrence, location, and severity of damage. In the SHM of concrete bridges, it is important to assess the relationship between structural performance and state of damage, to conduct maintenance. Therefore, the responses of a structure, which are divided into the two main groups of static and dynamic responses, are of critical importance. Developing efficient and reliable damage detection methods for daily use is a topic that has gained notable attention in the literature in recent years.

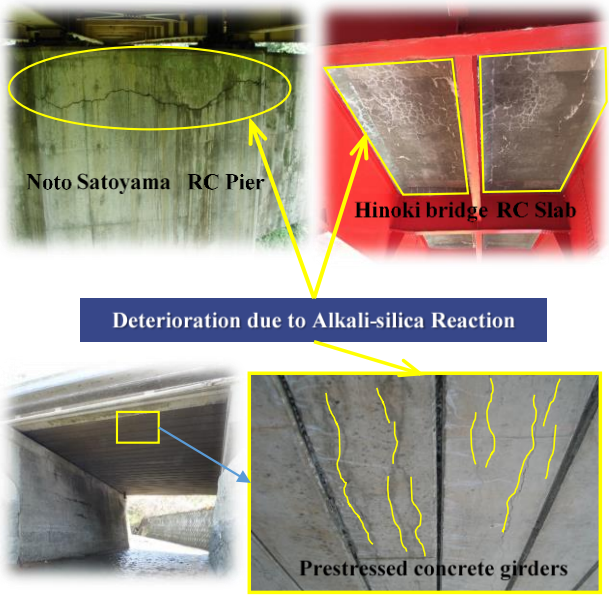


*Figure 1.1 ASR Deterioration in the Hokuriku region, Japan*

### 1.1.1 Damage detection based on dynamic responses

Over the years, many studies relating to the application of dynamic responses to damage detection have been performed [2–16], e.g., natural frequencies, mode shapes, modal curvature, and high-order mode shape derivative. A recent study demonstrated that natural frequencies, mode shapes, and damping ratios are invariant in structures [14]. Thus, the health of a structure is correlated to the changes in its modal parameters. Their alterations do not depend on the location of damage because of their global characteristics. Therefore, deterioration can be estimated by sensors mounted at any investigated positions of a structure. Specifically, changes in natural frequency have been thoroughly investigated as identifiers of stiffness reduction [3]. In addition, changes in uncertain frequency and mode shape data [4], in incomplete mode shape [5,6], in mode shape curvatures [7,8], in power spectrum density function of the response [9], and in the flexibility matrix [10] have been used for detecting and localizing damage. Variations in the element modal strain energy have been applied to improve damage quantification [11]. In 2016, by conducting a comparative study, Das et al. [12] reviewed the technical literature concerning vibration-based damage detection approaches utilized for civil engineering structures.

### 1.1.2 Damage detection based on static responses

Damage detection methods based on static data have attracted notable consideration, because static parameters depend on the stiffness matrix, and they can be obtained accurately and rapidly

by inexpensive tools of measurement [15–26]. To assess the stiffness matrix, Sheena et al. [17] introduced an analytical approach based on decreasing the deviation between the actual and the analytical stiffness matrix subjected to measured displacement constraints. In 1991, Sanayei and Onipede [18] proposed a precise method to evaluate the characteristics of structural elements from static experiment data, such as a set of applied static forces and another set of measured displacements. Based on the idea of minimizing the inconsistency between model and measurements by the constrained least-square minimization, Banan et al. [19] suggested an approach for determining member characteristics from displacements caused by an identified static load. Furthermore, Wang et al. [15] proposed a two-stage classification algorithm for recognizing structural damage based on the differences between natural frequencies and static displacements. Bakhtiari-Nejad et al. [22] presented a method to describe changes in a static displacement with certain degrees of freedom by minimizing the difference between the load vectors of damaged and undamaged structures. In another study worth mentioning, Lee and Eun [23] presented a numerical technique for damage detection by utilizing the displacement curvature and all static deflection data, which are expanded from the measured deflection data. As a result, the proposed method could efficiently detect single or multiple damages based on the exact displacement measurement, neglecting the variation between the test data and the analytical results. Five years later, Abdo [24] made a parametric investigation employing the displacement curvature for localizing damage. The results confirmed that alterations in the displacement curvature could be utilized as an effective indicator, even for a small amount of stiffness loss. Another study also assessed the effectiveness of using the displacement curvature derived from static response data for revealing the location and severity of damage in Euler–Bernoulli beams [25]. Numerical results proved that the displacement curvature obtained from static responses is sensitive to stiffness reductions (reduction of the Young's modulus). It reveals the characteristics of a damaged area, and thus, it can be used as a good indicator for damage detection. Additional research efforts attempted to detect damage properties using combined data from static and modal tests. Specifically, static and dynamic strain data from a distributed fiber optic sensor were employed to recognize the occurrence of damage to large structures [16].

### 1.1.3 Effects of environmental conditions on structural properties

Long-term monitoring data of actual structures include load-induced and temperature-induced structure responses. For many years, most researchers have concentrated on using structural responses for identifying the properties of damages (occurrence, location, and severity), whereas there are few studies concerning the effects of environmental conditions on variations of structural features (dynamic and static responses). If the effect of these uncertainties on

structural vibration properties is larger than or comparable to the effect of structural damage on its vibration properties, the structural damage cannot be reliably identified [27]. To avoid this happening, the structural response should be corrected to the same environmental conditions. For adequate maintenance, it is necessary to quantify the environment-induced changes and discriminate them from the effects due to damage. Therefore, studying the environmental effects on structural properties is important to reliably apply the monitoring methods to civil engineering structures. Cornwell [28] found that the first three natural frequencies of the Alamosa Canyon Bridge varied about 4.7%, 6.6% and 5.0% during a 24 h period as the temperature of the bridge deck changed by approximately 22 ºC. Peeters and De Roeck [29] reported that the first four vibration frequencies varied by 14%–18% during the ten months. It was also found that the frequencies of all the modes analyzed, except the second mode, decreased with the temperature increase. The second mode frequency, however, increased when the temperature was above 0 ºC. They also reported that the vibration frequencies increased significantly when temperature decreased to 0 ºC and below, which might be due to stiffening from the frozen layers. Xia [27] investigated the relation between dynamic properties and the environmental factors temperature and humidity. It is found that temperature deteriorates the modulus of elasticity of concrete significantly. Consequently, the natural frequencies decrease with temperature increase. This results can be interpreted by the fact that as concrete absorbs more water in higher humidity environment and increases the mass, the natural frequencies also decrease with humidity increase. Besides, to date, there are a few studies reported the effect of environmental conditions on static responses which are considered as upward displacement (also referred to as curling or camber) in this study.

### 1.1.4 Effects of fly ash on the soundness of ASR-affected structures

Towards the sustainable development of structures in the Hokuriku region, another concern of the present study was the possibility of applying fly ash to structures deteriorated by ASR to increase their service lives. Indeed, alkali-silica reaction is one of the prominent explanations of concrete degradation. As mentioned above, many reactive aggregates are widely distributed to many places in Japan. Especially, in Hokuriku region along the Sea of Japan, there is a wide spread of andesite which accelerates the ASR-induced expansion of concrete. The reaction begins with the expansion of reactive aggregate by forming a swelling gel of alkali silicate hydrate (N(K)-C-S-H). The ASR gel increases in volume, exerting significant pressure within the material, which causes spalling, cracking, and loss of strength in the concrete and rebar. The effects of blast furnace slag on the loading capacity of prestressed concrete (PC) specimens using reactive aggregates have been confirmed by Kunitomi et al. in 2015 [30]. Besides, it is now generally accepted that an appropriate use of fly ash can prevent expansion due to ASR in

concrete [31]. An increase in a level of replacement of a particular fly ash further reduced the expansion of concrete compared with the concrete without fly ash [32]. Since the Hokuriku region is currently able to produce a high-quality fly ash stably [33,34], the efficient use of fly ash helps improve the concrete durability and reduces the environmental burden as well as promote the regional industry due to the benefits of self-sufficiency. For example, together with the large-scale renewal project of Hokuriku Expressway using fly ash concrete precast PC slabs, the construction of new PC girder bridges in the local region also utilized fly ash for mitigating deterioration caused by ASR [35]. Indeed, the countermeasures for newly built bridges against ASR have achieved success. However, the evaluation criteria for repair and recovery work have not been clarified as regards to ASR-affected structures. Therefore, to obtain these materials and to evaluate the effectiveness of fly ash on mitigating ASR acceleration, it is necessary to study the loading capacity and mechanical properties of full-size PC girders degraded by ASR.

## 1.2 Objectives and scope

Among the numerous techniques developed for detecting structural damage, the changes in static parameters have been confirmed to be accurate in identifying the occurrence and location of structural damage [21]. Accordingly, the objective of this study is to investigate the feasibility of utilizing displacement data exclusively for structural damage detection. A numerical model of a prestressed concrete (PC) girder degraded by various damage scenarios was examined to reveal the relationship between deterioration state and static responses. Specifically, the outcome deflections at each stage of loading were obtained and used for determining two new damage indicators—displacement assurance criterion (DAC) and displacement-based index (DBI). Numerical studies were further performed utilizing finite-element commercial software to verify the correlation of DAC with severities of deterioration and the sensitivity of DBI in stiffness loss localization. Moreover, the effects of unforeseen parameters affecting the efficiency of the proposed methods, such as the number of measurements and the location of observed points, were also investigated. Besides the numerical studies, attempts have been made to evaluate the health of full-scale specimens by conducting long-term monitoring of the correlations between structural responses, ASR-caused deterioration, and environmental conditions.

As another effort, this study aims to investigate how the structural properties and load-bearing capacity of PC girders, which were affected by varying degrees of ASR-induced damages, change with and without fly ash. In other words, the effectiveness of employing fly ash to suppress ASR acceleration in structures was also discussed and analyzed through experiments and long-term monitoring approaches. To achieve this goal, three full-scale PC girders were conducted by the mixture of reactive andesite aggregates and high strength Portland cement.

Particularly, one of them was mixed with an additional amount of fly ash. After one and a half years of the exposure and monitoring of the variation in structural properties, destructive bending tests were carried out so as to clarify the difference in flexural capacity. In addition, after the bending tests, a significant number of concrete cores were taken from both girders to estimate the relationship between mechanical properties of concrete such as compressive strength, static elastic modulus, and ultrasonic wave propagation velocity. Based on the obtained results, this study clarified mechanical properties of PC girder with and without fly ash affected by ASR deterioration.

As discussed above, changes in environmental conditions also affect structural dynamic and static responses in a complicated manner. Therefore, the variation of structural performance due to environmental change should be discriminated from those caused by structural damage. In this study, the changes in the vibrational and static parameters of the three PC girders were monitored with respect to variations in ambient temperature and humidity, as well as development in ASR-induced cracks. In particular, the responses of three PC girders and the environmental conditions have been periodically monitored for one and a half years. Its vibrational properties, namely frequencies, mode shapes, damping ratios, and temperature-induced displacements at different times were measured together with the ambient temperature during each measurement. To obtain more information about the correlations of the structural responses with the environmental conditions, the obtained data were then analyzed using linear regression models concerning the variations in the temperature and humidity. Moreover, the measured data were compared with predicted values obtained using finite element analysis procedures and trend line (empirical-linear). Finite element models were proposed and employed for conducting the analysis utilizing the computer code DIANA. The different dynamic and static performances of the three specimens were also considered to evaluate the effects of fly ash on ASR-affected structures. This study presents preliminary considerations for estimating the long-term behavior of PC girders and attempts to proposed recommendations about measurement noise when using structural responses as input for structural damage detection.

The feasibility of the proposed DAC approach on practical cases was also evaluated and discussed. The displacement curves obtained from the destructive tests conducted on the PC girders were employed as the input for the DAC calculation to identify structural degradation. During the loading test, the vertical displacement was measured at seven points under the girders for computing the deflection curve at each loading step. Then, the obtained curves were analyzed to estimate the variation in the DAC value. Besides, a nonlinear finite-element model of the PC girder was produced to verify the relation between the changes in DAC with respect to structural degradation owing to applied loads in practice. Validations of the numerical analyses against the results of loading test were then considered for the evaluation of the

proposed approach. From the obtained results of the numerical and experimental approaches, this study aims to propose a threshold of DAC index for healthy structure in further researches.

### 1.3 Structure of the dissertation

This dissertation consists of 7 chapters including an introduction, and the entire study is roughly illustrated by the structure shown in **Fig. 1.2**.

**Chapter 2** provide an overview of the behaviors of actual structures affected by ASR. Specifically, this chapter presents the results of numerous experiments including long-term monitoring of structural behaviors and loading test conducted on the three PC girders placed outside the laboratory. Especially, reactive andesite aggregates were utilized for the mixtures of all girders. One of the girders was specially mixed with a controlled amount of fly ash for mitigating concrete expansion caused by ASR. Therefore, in addition to presenting changes in material properties of the structures under the influence of ASR, this chapter is also a feasibility study of using fly ash to minimize the damage caused by ASR.

In **Chapter 3**, the use of static response as the input in the evaluation procedures of prestressed concrete structures was discussed. DAC and DBI were introduced and employed in numerous scenarios to determine damage properties. This chapter shows the results of numerical studies performed by finite-element analyses to verify the feasibility of the two proposed indices. In addition, the advantage and disadvantage of the proposed approaches were also evaluated and mentioned.

**Chapters 4 and 5** show a perspective on the effect of temperature and humidity on the dynamic and static behaviors of the structure, which have been used as the inputs in many damage detection approaches. From the obtained results, this chapter aims to provide a recommendation on the direct use of measured responses for assessing the health of structures.

In **Chapter 6**, attempts have been made to utilize Displacement Assurance Criterion proposed in **Chapter 3** on practical cases. The results of the destructive loading tests were carried out to evaluate the feasibility of DAC approach on damage detection. From the obtained results of the numerical and experimental methods, this chapter introduces a threshold of DAC index for healthy structure.

**Chapter 7** summarizes the results obtained in this study.

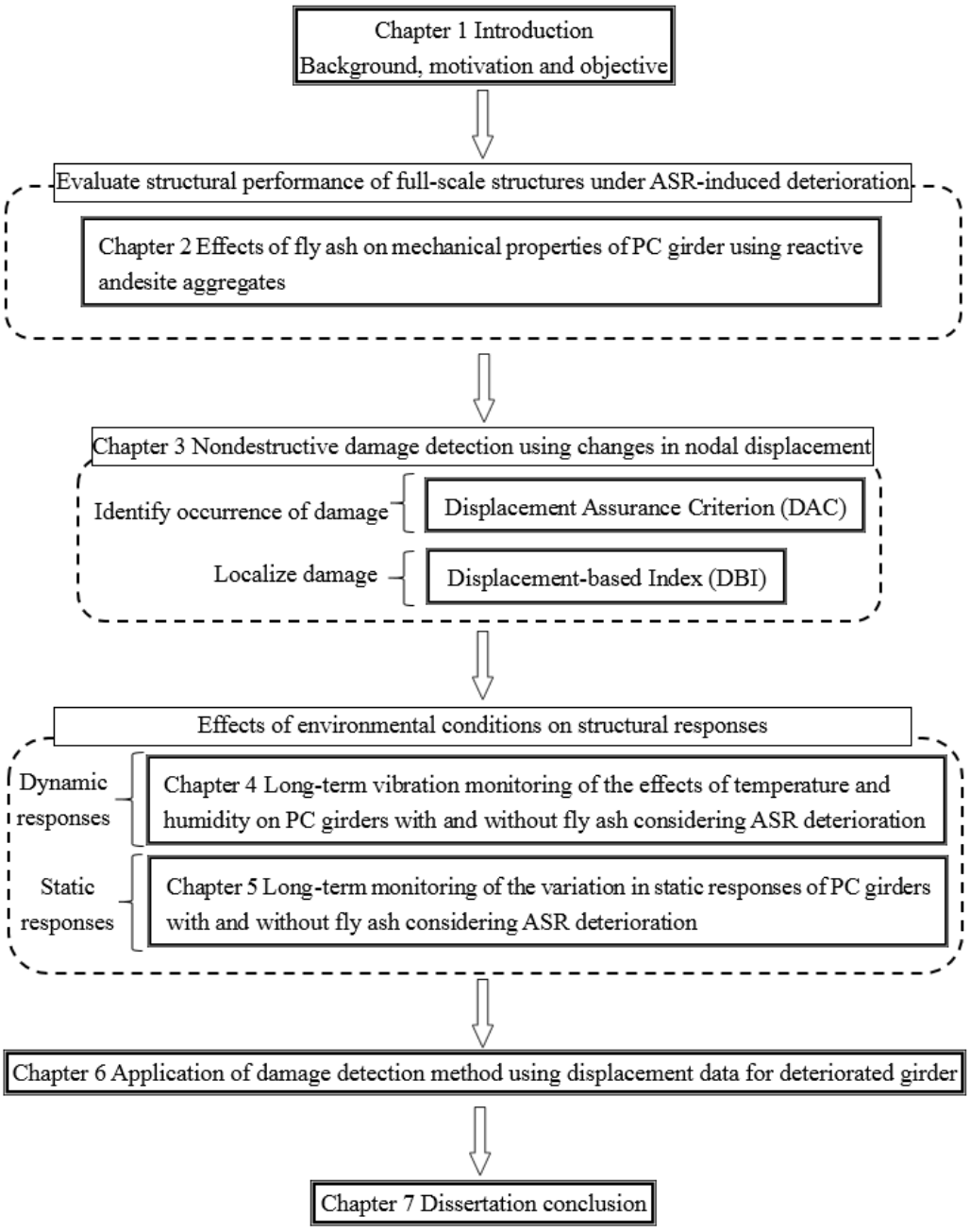


*Figure 1.2 Structure of this dissertation*

## 1.4 References

[1] T. M. Ha, S. Fukada, K. Torii, K. Kobayashi, and T. Aoyama, "Load bearing capacity of PC girders with and without fly ash affected by ASR deteriorations," in *High Tech Concrete: Where Technology and Engineering Meet - Proceedings of the 2017 fib Symposium*, 2017, pp. 321–329.

[2] A. Rytter, "Vibrational Based Inspection of Civil Engineering Structures," 1993.

[3] S. Hassiotis and G. D. Jeong, "Identification of Stiffness Reductions Using Natural Frequencies," *J. Eng. Mech.*, vol. 121, no. 10, pp. 1106–1113, 1995.

[4] Y. Xia, H. Hao, J. M. W. Brownjohn, and P. Q. Xia, "Damage identification of structures with uncertain frequency and mode shape data," *Earthq. Eng. Struct. Dyn.*, vol. 31, no. 5, pp. 1053–1066, 2002.

[5] Z. Y. Shi, S. S. Law, and L. M. Zhang, "Damage Localization by Directly Using Incomplete Mode Shapes," *J. Eng. Mech.*, vol. 126, no. 6, pp. 656–660, 2000.

[6] C. Y. Kao, X. Z. Chen, J. C. Jan, and S. L. Hung, "Locating damage to structures using incomplete measurements," *J. Civ. Struct. Heal. Monit.*, vol. 6, no. 5, pp. 817–838, 2016.

[7] A. K. Pandey, M. Biswas, and M. M. Samman, "Damage detection from changes in curvature mode shapes," *J. Sound Vib.*, vol. 145, no. 2, pp. 321–332, 1991.

[8] H. Zhong and M. Yang, "Damage detection for plate-like structures using generalized curvature mode shape method," *J. Civ. Struct. Heal. Monit.*, vol. 6, no. 1, pp. 141–152, 2016.

[9] T. Oshima, Y. Miyamori, S. Mikami, T. Yamazaki, S. Beskhyroun, and M. F. Kopacz, "Small damage detection of real steel bridge by using local excitation method," *J. Civ. Struct. Heal. Monit.*, vol. 3, no. 4, pp. 307–315, 2013.

[10] A. K. Pandey and M. Biswas, "Damage Detection in Structures Using Changes in Flexibility," *J. Sound Vib.*, vol. 169, no. 1, pp. 3–17, 1994.

[11] L. M. Z. Z. Y. Shi, S. S. Law, "Improved Damage Quantification from Elemental Modal Strain Energy Change," *J. Eng. Mech.*, vol. 128, no. 5, pp. 521–529, 2002.

[12] S. Das, P. Saha, and S. K. Patro, "Vibration-based damage detection techniques used for health monitoring of structures: a review," *J. Civ. Struct. Heal. Monit.*, vol. 6, no. 3, pp. 477–507, 2016.

[13] S. M. Seyedpoor, "Structural Damage Detection Using a Multi-Stage Particle Swarm Optimization," *Adv. Struct. Eng.*, vol. 14, no. 3, pp. 533–549, 2011.

[14] O. Huth, G. Feltrin, J. Maeck, N. Kilic, and M. Motavalli, "Damage Identification Using Modal Data: Experiences on a Prestressed Concrete Bridge," *J. Struct. Eng.*, vol. 131, no. 12, pp. 1898–1910, 2005.

[15] X. Wang, N. Hu, H. Fukunaga, and Z. H. Yao, "Structural damage identification using

static test data and changes in frequencies," *Eng. Struct.*, vol. 23, no. 6, pp. 610–621, 2001.

[16] J.-W. Lee, K.-H. Choi, and Y.-C. Huh, "Damage detection method for large structures using static and dynamic strain data from distributed fiber optic sensor," *Int. J. Steel Struct.*, vol. 10, no. 1, pp. 91–97, Mar. 2010.

[17] Z. Sheena, A. Unger, and A. Zalmanovich, "Theoretical stiffness matrix correction by static test results," *Isr J Technol*, vol. 20, no. 6, pp. 245–253, 1982.

[18] M. Sanayei and O. Onipede, "Damage assessment of structures using static test data," *AIAA J.*, vol. 29, no. 7, pp. 1174–1179, 1991.

[19] M. R. Banan and K. D. Hjelmstad, "Parameter Estimation of Structures from Static Response. I. Computational Aspects," *J. Struct. Eng.*, vol. 120, no. 11, pp. 3243–3258, 1994.

[20] I. Y. Choi, J. S. Lee, E. Choi, and H. N. Cho, "Development of elastic damage load theorem for damage detection in a statically determinate beam," *Computers and Structures*, vol. 82, no. 29–30. pp. 2483–2492, 2004.

[21] X. Z. Chen, H. P. Zhu, and C. Y. Chen, "Structural damage identification using test static data based on grey system theory," *J. Zhejiang Univ. Sci.*, vol. 6A, pp. 790–796, 2005.

[22] F. Bakhtiari-Nejad, A. Rahai, and A. Esfandiari, "A structural damage detection method using static noisy data," *Eng. Struct.*, vol. 27, no. 12 SPEC. ISS., pp. 1784–1793, 2005.

[23] E. T. Lee and H. C. Eun, "Damage detection of damaged beam by constrained displacement curvature," *J. Mech. Sci. Technol.*, vol. 22, no. 6, pp. 1111–1120, 2008.

[24] M. A.-B. Abdo, "Parametric study of using only static response in structural damage detection," *Eng. Struct.*, vol. 34, pp. 124–131, 2012.

[25] O. Yazdanpanah and S. Seyedpoor, "A crack localization method for beams via an efficient static data based indicator," *Comput. Methods Civ. Eng.*, vol. 4, no. 1, pp. 43–63, 2013.

[26] S. M. Seyedpoor and O. Yazdanpanah, "An efficient indicator for structural damage localization using the change of strain energy based on static noisy data," *Appl. Math. Model.*, vol. 38, no. 9–10, pp. 2661–2672, 2014.

[27] Y. Xia, H. Hao, G. Zanardo, and A. Deeks, "Long term vibration monitoring of an RC slab: Temperature and humidity effect," *Eng. Struct.*, vol. 28, no. 3, pp. 441–452, 2006.

[28] P. Cornwell, C. R. Farrar, S. W. Doebling, and H. Sohn, "ENVIRONMENTAL VARIABILITY OF MODAL PROPERTIES," *Exp. Tech.*, vol. 23, no. 6, pp. 45–48, 1999.

[29] B. Peeters and G. De Roeck, "One-year monitoring of the Z24-bridge: Environmental effects versus damage events," *Earthq. Eng. Struct. Dyn.*, vol. 30, no. 2, pp. 149–171, 2001.

[30] Y. Kunitomi, A. Ishii, J. Xin, and K. Torii, "Characteristic of load-bearing capacity of PC

beams using ground granulated blast furnace slag by ASR accelerated exposure test," *J. Prestress. Concr.*, vol. 57, no. 3, pp. 68–74, 2015.

[31] K. Torii, T. Kubo, C. Sannoh, and M. Kanitani, "The alkali-silica reactivity of andesitic river aggregates and ASR mitigating effect by using fine fly ashes.," in *15th International Conference on Alkali-Aggregate Reaction*, 2016.

[32] M. H. Shehata and M. D. A. Thomas, "Effect of fly ash composition on the expansion of concrete due to alkali-silica reaction," *Cem. Concr. Res.*, vol. 30, no. 7, pp. 1063–1072, 2000.

[33] T. Hashimoto and K. Torii, "The development of highly durable Concrete using classified fine fly ash in Hokuriku district," *J. Adv. Concr. Technol.*, vol. 11, pp. 312–321, 2013.

[34] T. Hashimoto and K. Torii, "The assessment on ASR of aggregates and ASR mitigation effect by fine fly ash," *Concr. Aust.*, vol. 42, no. 2, pp. 65–71, 2015.

[35] S. Yamamura, M. Sakurada, K. Kobayashi, and K. Torii, "Application of fly ash concrete to prestressed concrete bridges," *Cem. Concr.*, vol. 828, pp. 22–27, 2016.

# Chapter | 2

# Effects of Fly Ash on Mechanical Properties of PC Girder Using Reactive Andesite Aggregates

## 2.1 Introduction

During the previous years, the degradation due to alkali-silica reaction (ASR) in concrete structures has become a global concern. Many structures such as bridges, dams and concrete barriers were affected. Stanton [1] showed the loss in engineering features due to ASR for the first time in the U.S. in 1940. Since then, an increasing number of regions with different climates where civil engineering works experience deterioration problems as a result of the ASR has been reported from Argentina, Switzerland, Netherlands, Korea, Japan, Thailand and other countries [2–6]. In Japan, mineralogical and geological studies show that many reactive aggregates in the soil are widely distributed throughout the country [7]. Particularly in the Noto region, there is a wide distribution of andesite, which is the primary cause of ASR degradation in bridges [8–10]. Since 1982, ASR has been observed in highway structures in this region, where deicing salts (mainly NaCl) are used in the winter [11]. The added alkali contents from deicing salt and seawater have raised concrete alkali levels above acceptable limits, excepting concrete in cooperation with mineral admixtures such as blast-furnace slag or fly ash. Up to recent years, not only the Noto region but many infrastructures in the Hokuriku region (Fukui, Ishikawa, Toyama, and Niigata prefectures) were also degraded by ASR [12,13]. The reaction starts the expansion of reactive aggregate by forming a swelling gel of alkali silicate hydrate (N(K)-C-S-H). The ASR gel increases in volume, exerting significant pressure within the material, which causes spalling, cracking, and loss of strength in the concrete and rebar. The relations between the characteristics of ASR-induced damage and the reduction of the elastic modulus have been proved by many previous studies [14]. Detailed information on the cracking behaviors of many concrete structures damaged by ASR was presented in studies of Ono [15] and Tordoff [16]. Cracking in concrete due to ASR takes various patterns. In the portions of a reinforced concrete (RC) structure with little or no surface reinforcement, cracking tended to be irregular and maplike. The authors also suggested that, while notable and extensive corrosion had not yet been recognized, appropriate repair techniques should be considered to protect the damaged structures from further deterioration. Therefore, the development of maintenance

management methods became an important topic in the literature in recent years.

Regarding modeling approaches, the ASR gel production, expansive behavior of ASR, and its damage have been studied recently [17–19]. Saouma [19] proposed finite element method (FEM) models for ASR, considering the micro-chemical reactions while attempting to apply models to structural levels. Two years later, by utilizing a computation scheme of multi-scale poro-mechanics, Takahashi et al. [18] carried out sensitivity analyses with the permeation of produced silica gel. Since structural concrete usually experiences combined effects of ASR, carbonation, freeze-thaw cycles, steel corrosion, and high cycle fatigue loads [17], the concrete degradation is complex. Indeed, ASR and steel corrosion will consume water on which frost damage also relies. In 2017, Gong et al. [17] successfully modeled the interaction between freeze-thaw cycles and ASR form the micro-structural level, taking the ice formation and ASR gel intrusion in pores into account, as well as the effect of entrained air.

For the experimental and monitoring approaches, the effects of blast furnace slag on the loading capacity of prestressed concrete (PC) specimens using reactive aggregates have been confirmed by Kunitomi et al. in 2015 [20]. Besides, it is now generally accepted that an appropriate use of fly ash can prevent expansion due to ASR in concrete [21]. An increase in a level of replacement of a particular fly ash further reduced the expansion of concrete compared with the concrete without fly ash [22]. Since the Hokuriku region is currently able to provide a high quality fly ash stably [23,24], the efficient use of fly ash helps improve the concrete durability and reduces the environmental burden as well as promote the regional industry due to the benefits of self-sufficiency. For example, together with the large-scale renewal project of Hokuriku Expressway using fly ash concrete precast PC slabs, the construction of new PC girder bridges in the local region also utilized fly ash for mitigating deterioration caused by ASR [25]. Indeed, the countermeasures for newly built bridges against ASR have achieved success. However, the evaluation criteria for repair and recovery work have not been clarified as regards to ASR-affected structures. Therefore, to obtain these materials, it is necessary to study the loading capacity and mechanical properties of full-size PC girders degraded by ASR. Over the years, many researchers have taken the loading tests on both ASR-degraded PC and RC specimens.

Regarding RC structures, Swamy and Al-Asali [26] carried out destructive load tests on RC beams, which were made with reactive coarse and fine aggregates, to determine their structural behaviors (load versus deflection) under significant ASR expansions. Their outcomes showed that the initial stiffness and ultimate load-carrying capacity were not obviously influenced by ASR and loading conditions, whereas ASR-induced reductions in the tensile strength and dynamic modulus of elasticity of concrete beams could be perceived. Later, Shenfu and Hanson [27] made six 1500 mm long reinforced concrete beams and immersed them in a cyclically-heated alkali solution in one year to accelerate ASR. Particularly, three of them were

produced with the reactive concrete, while the nonreactive concrete was utilized for the other beams. Although ASR-caused cracks occurred on specimens made with the reactive aggregate after six months of the immersion, they performed nearly the same flexural strengths as the nonreactive beams did. Moreover, the influence of ASR on the flexural loading capacity of preloaded and cracked beams was also perceived to be insignificant. The fracture mechanism of reinforcing steels in the case of concrete structures damaged by ASR was studied thoroughly by Miyagawa et al. [28]. The authors introduced the results of the investigation on the fracture mechanism, nondestructive testing methods, and repair and strengthening methods for damaged concrete structures. Particularly, the steel bar rib shape and the bending radius were considered to have a significant causal influence on steel bar fractures due to ASR. Moreover, weather conditions (such as rainwater, sunlight, and ambient temperature) caused obvious effects on ASR-induced deterioration which also tends to be particularly severe at locations where the number of steel bars is relatively small. As long as ASR-caused expansion does not break reinforcing steels, the soundness of a structure is considered not to be endangered. In 2012, Wang and Morikawa [29] studied the deterioration situation of concrete members due to ASR and its influence on shear failure mechanism and shear resisting performance of 1200 mm RC beams in both experimental and numerical approaches. The experimental results showed that undesirable shear collapse modes were obtained and the bond slip was easy to occur in RC beam with ASR-induced cracks along the tensile reinforcing bars. Besides, ASR deterioration was considered as the thermal strain model, which utilized a series of temperature values and the linear thermal expansion coefficient of the concrete element as inputs for simulating the expansion caused by ASR degradation. Their analysis results showed a good agreement with the experimental data regarding the load-displacement response, crack pattern and rebar strain distribution. As another study of Hajighasemali et al. [30], the influence of ASR on overall serviceability, strength, ductility and deformability on RC beams under service load conditions was investigated by considering creep and ductility phenomena. Twelve 1100 mm long RC beam specimens were initially produced utilizing to nonidentical concrete mixtures containing reactive aggregates (R) and nonreactive aggregates (N). The specimens were later subjected to flexural testing after 360 days of accelerated ASR conditioning. For ductility and deformability analyses on the basis of comparison of R and N beams, ductile indices related to displacement, curvature, and energy were estimated by considering load-deflection and moment-curvature curves. Their conclusions proved that ASR has a significant effect on the R beams (where cracks occurred at lower loads) and, the N beams were stronger than their equivalent R specimens at final loading.

The structural performance of the prestressed beams made of concrete affected by ASR-affected by ASR was described by Kobayashi et al. [31] in comparison with those of corresponding healthy beams. Ten 1600 mm PC beams made of two types of concrete with

alkali-silica reactivity and sound concrete under an accelerated curing condition of 40 ºC and 100 % RH were subjected to long-term monitoring of changes in steel strains and destructive tests with shear span to effective depth ratio of 2.5 and 4.0. As their findings, longitudinal ASR expansion could be restrained by the introduction of prestressing force, although the effect depends strongly upon the amount of the prestress. Also, the reduction in the ultimate strength of ASR beam was approximately 10 % compared with that of the sound beam, even when the tensile strain in vertical stirrup exceeded $1000\times10^{-6}$ and many longitudinal cracks occurred. Takebe et at. [32] verified the effects of the presence or absence of ASR deterioration on shear strength of concrete members using two different PC specimens (height 300 mm × width 300 mm × length 2000 mm). The controlled beam contains normal aggregate and the other has ASR reactive aggregate in its mixture. Before destructive loading tests, both specimens were exposed outdoors for further progress of ASR deterioration in approximately 3 years. Their findings showed that both specimens failed in flexural mode, with final load of ASR-affected beam being about 7 % lower than that of the normal one. As recent efforts, Hiroi et al. [33] carried out the flexural loading test on real-scale large PC beams (height 1250 mm × width 1200 mm × length 7000 mm) which were exposed to 7.5 years of deterioration. After the tests, concrete core samples were collected from the beams to evaluate mechanical properties of ASR-affected concrete. Their outcomes show that the mechanical values decreased even in the longitudinal direction where there was confinement due to the prestress. Moreover, the decreases in Young's modulus and tensile strength were more obvious than that of compressive strength, and the decrease rate was higher in the vertical cores in which confinement was absent, as compared to the longitudinal cores. As another attempt of the same study, Yokoyama et al. [34] performed a visual observation of internal cracks in the cut section. Although many ASR cracks could be easily observed in the surface areas of the beam, most of them occurred outside the stirrups, with almost no further progress into the inside. Besides, the development of flexural cracks was partly interrupted by the appearance of ASR-induced horizontal cracks in the cover concrete, that resulted in a relatively decrease in stiffness.

In addition, for the investigation and inspection of an actual bridge in which main girders were placed side by side as shown in **Fig. 2.1**, concrete cores are usually taken from side surfaces which might not provide enough information about the load-carrying capacity and stiffness of the girder accurately. As the development of cracks in PC girders is also governed by the restraints of the PC strands, the mechanical properties of concrete might differ from prestressing direction (girder-axis direction) to transverse direction [20]. Therefore, it is necessary to study this anisotropy of concrete in degraded PC girders.

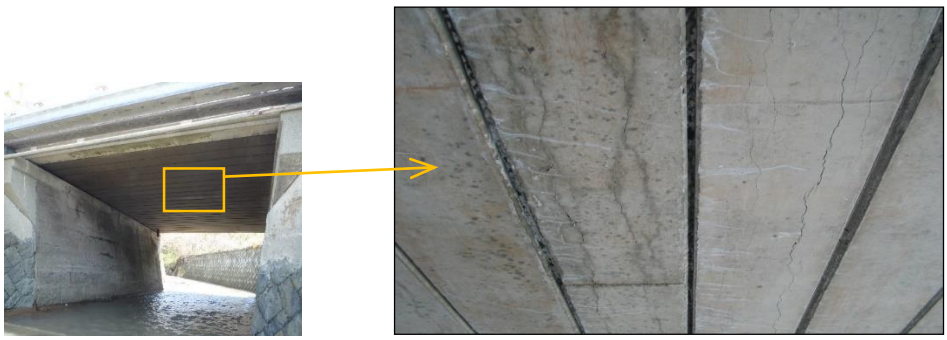

*Figure 2.1 Cracks occurs along with the PC strands (bottom surfaces).*

After all, none of above studies have been taken on the real-scale PC specimens using reactive aggregates to find the difference in flexural capacity due to the fly ash content. This study aims to investigate how the structural properties and load bearing capacity of PC girders, which were affected by varying degrees of ASR-induced damages, change with and without fly ash. Three full-scale PC girders were conducted by the mixture of reactive aggregates and high strength Portland cement for the present study. Particularly, one of them was mixed with an additional amount of fly ash. After one and a half years of the exposure, destructive bending tests were performed on two of the three girders so as to clarify the difference in flexural capacity. In addition, after the bending tests, a large number of concrete cores were taken from both girders to estimate the relationship between mechanical properties of concrete such as compressive strength, static elastic modulus, and ultrasonic wave propagation velocity. Based on the obtained results from the two girders, this study clarified mechanical properties of PC girder with and without fly ash affected by ASR deteriorations.

## 2.2 Description of the PC girders

### 2.2.1 Shape and exposure conditions

The PC girders produced in this study were the full-size JIS A5373-AS09 girder. The side and cross-sectional views of the girders were the same, as shown in **Fig. 2.2**. From this figure, the girders had a length of 9600mm, a cross-section with an upper-edge width of 640 mm, a lower edge width of 700 mm, and a height of 450 mm. It should be noted that the sheath holes for lateral tightening of transverse beams were not provided. Regarding PC strands, each objective girder contained sixteen strands (SWPR7BL1S 12.7 mm) arranged longitudinally in three layers. Specifically, four strands were put as the first layer in the compression area while the other two layers consisted six strands in each were arranged in the tension area. The girders, which were obtained using a pretensioning method, had the same profiles and dimensions as the strands and stirrups. In this study, high strength Portland cement was utilized for all girders. One of them was particularly mixed with an addition amount of fly ash (girder No.3), while the

other girders without fly ash was named as girder No.1 and girder No.2. After 14 h of steam curing at 50 ºC, the tendons were released from the external frames, and subsequently, the PC girders were continuously moistened indoor for approximately one week. Following the initial curing, they were placed in a sunshiny area of Kakuma campus in Kanazawa city so as to be exposed to outdoor environment for one and a half years, as shown in **Fig. 2.3**. During the exposure period, the average ambient temperature of Kanazawa city varied from approximately ~13.3 ºC in April to ~27 ºC in August 2015 (during summer) and then decreased gradually by ~22 ºC from the high temperature to ~5 ºC in January 2016 (between summer and winter), before rising gradually again to ~27.5 ºC in August 2016 (summer season) [35]. The average ambient humidity was around 70% [35].

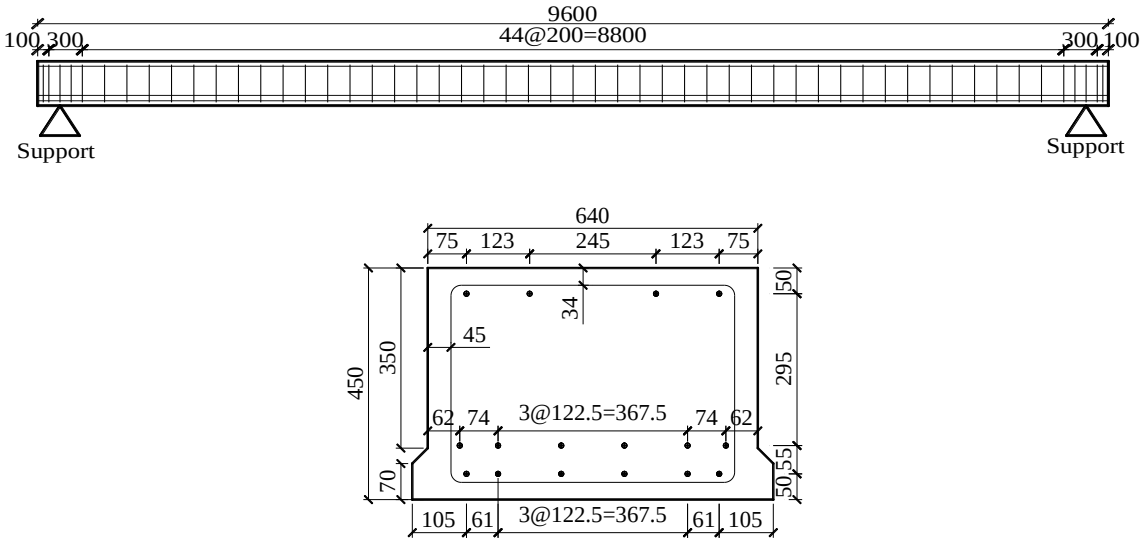


*Figure 2.2 Diagram of PC girders (unit: mm).*

*Figure 2.3 Exposure condition of the PC girders at Kakuma campus*

### 2.2.2 Materials

Materials used for the PC girders are summarized in **Table 2.1**. River sand and crushed stones from the Joganji River were used as reactive aggregates, which contain mainly cristobalite and opal. In addition, fly ash with an average grain size of up to 7μm was taken from Nanao Ohta Thermal Power Station of Hokuriku Electric Power Company.

*Table 2.1 Material properties of the girders.*

| Material | Symbol | Specification |
|---|---|---|
| Cement | C | Early-strength Portland cement, density: 3.14 kg/cm$^3$, specific surface area: 4510 cm$^2$/g |
| Admixture | FA | Classified fly ash (Nanao Ohta Thermal Power Station), density: 2.43 g/cm$^3$, specific surface area: 4500 cm$^2$/g, ignition loss value: 2.0 % |
| Fine aggregate | S | River sand (from the Joganji River), density in saturated surface-dry condition: 2.61 g/cm$^3$ |
| Coarse aggregate | G | Crushed stone (from the Joganji River), density in saturated surface-dry condition: 2.61 g/cm$^3$ |
| High-performance water-reducing agent | SP | Mighty 21LV (Kao Chemicals) |
| AE agent | AE | Vinsol (Yamaso Chemicals) |

*Table 2.2 Mixture properties.*

| Girder | Water-binder ratio W/B (%) | Fine aggregate percentage s/a (%) | Unit (Kg/m$^3$) | | | | | |
|---|---|---|---|---|---|---|---|---|
| | | | Water W | Binder B | | Sand S | Gravel G | NaCl |
| | | | | Cement C | Fly ash FA | | | |
| No.1 | 38.7 | 46.3 | 150 | 388 | - | 822 | 955 | 18.87 |
| No.2 | 38.7 | 46.3 | 150 | 388 | - | 822 | 955 | 25.5 |
| No.3 | 34.8 | 44.6 | 150 | 366 | 65 | 770 | 955 | 25.5 |

### 2.2.3 Mixtures

Three specimens were cast using the mixtures listed in **Table 2.2**. In this study, high-strength Portland cement was used for all the girders. One of them, namely girder No.3, was mixed with fly ash to mitigate the expansion of the concrete due to the ASR. The replacement rate of the fly ash to binder was set to 15% considering the quality and workability of the classified ash from a previous research result [25], wherein the effectiveness of the fly ash in reducing the

ASR-induced damage was confirmed. Moreover, to promote the expansion of the concrete via the ASR, 18.87 kg/m$^3$ NaCl in an equivalent amount of 10 kg/m$^3$ $Na_2O$ was added to the mixture of girder No.1, whereas No.2 and No.3 were mixed with 25.5 kg/m$^3$ NaCl in an equivalent amount of 13 kg/m$^3$ $Na_2O$. In the present study, the destructive loading test was only conducted on girders No.2 and No.3. Therefore, the results of the loading test on girders No.2 and No.3 are presented in the following sections of this chapter.

### 2.2.4 Material characteristics of concrete

Girders No.2 and No.3 had the same design compressive strength which were 35 N/mm$^2$ and 50 N/mm$^2$ at the ages of 1 day and 14 days after casting, respectively. **Table 2.3** shows the compressive strength of the girders at the time of stress transferring, seven days and 28 days of age. As shown in this table, girder No.2 had higher compressive strength than girder No.3 at 28-day age.

*Table 2.3 Compression strength of concrete (unit: N/mm$^2$).*

| | Stress transferring | σ 7 | σ 28 |
|---|---|---|---|
| Girder No.2 | 59.3 | 70.3 | 79.8 |
| Girder No.3 | 54.4 | 65.9 | 77.4 |

### 2.2.5 Material characteristics of steels

Material characteristics of steels are shown in **Table 2.4**. SD295 D10 rebars were used for stirrups at 200 mm intervals while sixteen high strength steel wires SWPR7BL(1S 12.7 mm) were employed as strands used for prestressing. After 14 hours of casting, the strands were released from external frames and their tensile stresses of 1271 N/mm$^2$ were transferred to the concrete.

*Table 2.4 Material characteristics of steels (unit: N/mm$^2$).*

| | Yield stress | Tensile strength |
|---|---|---|
| SD295 D10 | 375 | 512 |
| SWPR7BL1S 12.7 mm | 1832 | 2015 |

## 2.3 Deterioration situations of PC girders before the loading test

### 2.3.1 Development of ASR-caused cracks

**Figure 2.4** show the crack patterns of the three girders after one and a half years of outdoor exposure. The black lines indicate the crack widths in the range of 0.3–0.8 mm whereas the crack widths over 0.8 mm are indicated using red lines. On the side and top surfaces of girders

No.1 and No.2, many cracks formed along the girder axis, whereas a few cracks could be observed on the lower surfaces. The acceleration of ASR-induced cracks on the top and side surfaces as described above was considered to be due to the influence of water and insolation. Moreover, alligator cracks were mainly observed at the girder end, where no prestress was introduced because of the influence of the adhesion transmission length of tendons, which was considered as 65 times the strand diameter (φ = 12.7 mm). Regarding girder No.3, cracks partially formed near the ends and on the side surfaces. Because the number of cracks was considerably small, the expansion of the ASR was effectively suppressed owing to the fly ash.

### 2.3.2 Upward vertical displacement

**Figure 2.5** shows changes in convex curvature (upward vertical deflection) in the middle of the span of girders No.2 and No.3 during the exposure period, which was measured by stretching a leveling string (**Fig. 2.6**) between both ends. As regards girder No.2, the convex displacement increased up to approximately 13 mm before starting the load test. Meanwhile, almost no variation of the convex curvature over time was observed in girder No.3 mixed with fly ash. This monitoring result was also confirmed by previous researches [20,36]. Based on monitoring development of cracks in girder No.2, this study considered that ASR was accelerated by the penetration of water and the insolation. Because the top surface and both side surfaces were directly exposed to the sun, they suffered higher influences of solar radiation and rain than the bottom surface. Consequently, there were differences in ASR-induced expansion ratio of concrete between surfaces. Changes in the expansion ratio during the follow-up period of both girders are discussed in the following section. In addition, regarding the detail of PC strands, four strands were put as the first layer in the compression area while the other two layers consisted six strands in each were arranged in the tension area, as indicated in **Fig. 2.2**. Therefore, the upward curvature was generated not only by the difference in expansion amount but also by the difference in the tensioning forces of the PC strands between the upper and the lower concrete parts.

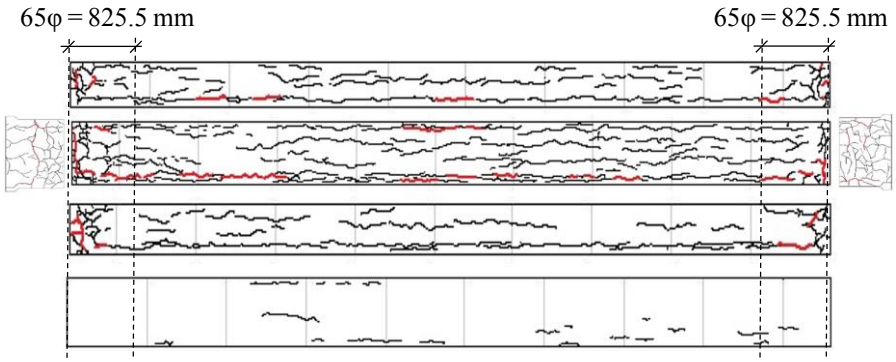


(a) Girder No.1

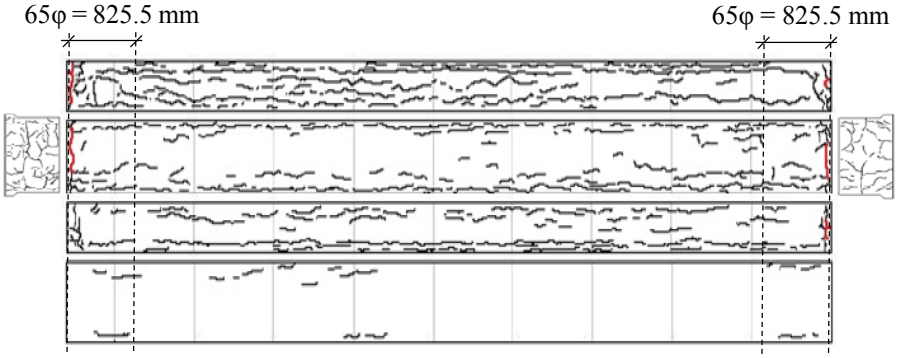


(b) Girder No.2

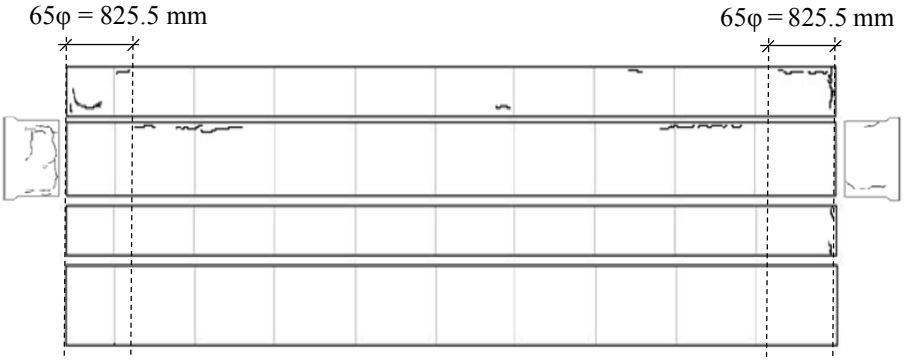


(c) Girder No.3

*Figure 2.4 Crack patterns of the three girders (From top to down: north side surface, top surface and both surfaces near both ends, south side surface and bottom surface) and the adhesion transmission length of tendons (approximately 825.5 mm) (unit: mm).*

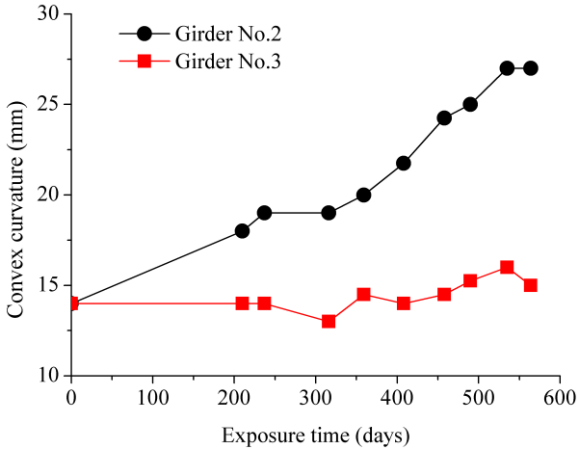


*Figure 2.5 Changes in the convex curvature.*

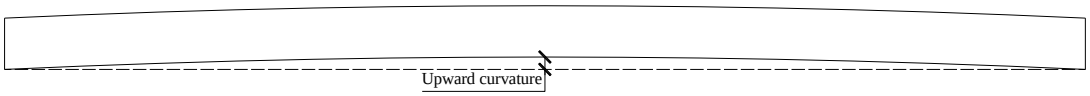


*Figure 2.6 Measurement of Convex curvature*

### 2.3.3 Expansion rates

The progress of ASR deterioration in the PC girders was also observed by monitoring expansion ratio of concrete. Specifically, the ratios in the longitudinal direction (girder-axis direction) and the perpendicular direction of all concrete surfaces (upper, side and bottom surfaces) were measured near the supports and the span center as shown in **Fig. 2.7**. For each girder, 78 gauge plugs were affixed to the measurement positions then the measurement was performed periodically using a digital type contact micron strain gauge (**Fig. 2.8**). For tracking the variation of concrete expansion due to ASR, twelve tests were performed from July 2015 to October 2016, and there were 2880 valid sets of measurement data. The ratio was calculated by a change in the distance between two plugs (initial length = 100 mm). **Figures 2.9 and 2.10** show the variation in measurement results of both girders in the longitudinal and perpendicular directions over time, respectively. Each value indicated in these figures is the average of all results obtained from strain gauges mounted on the target surface in each measurement. From these figures, the expansion ratio of girder No.2 increased in the order of the bottom surface < the side surfaces < the top surface. Regarding girder No.3, this value reduced greatly at all parts. Moreover, when comparing the measured data on the top surface of girder No.2, the expansion ratio in the transverse direction was measured as 0.35% or more before the loading test, whereas it was 0.04% or less in the longitudinal direction. Therefore, because the expansion ratio in the transverse direction of the girder without fly ash was higher than in the longitudinal direction, there was a relation between the expansion ratio of concrete and the formation of longitudinal cracks owing to ASR.

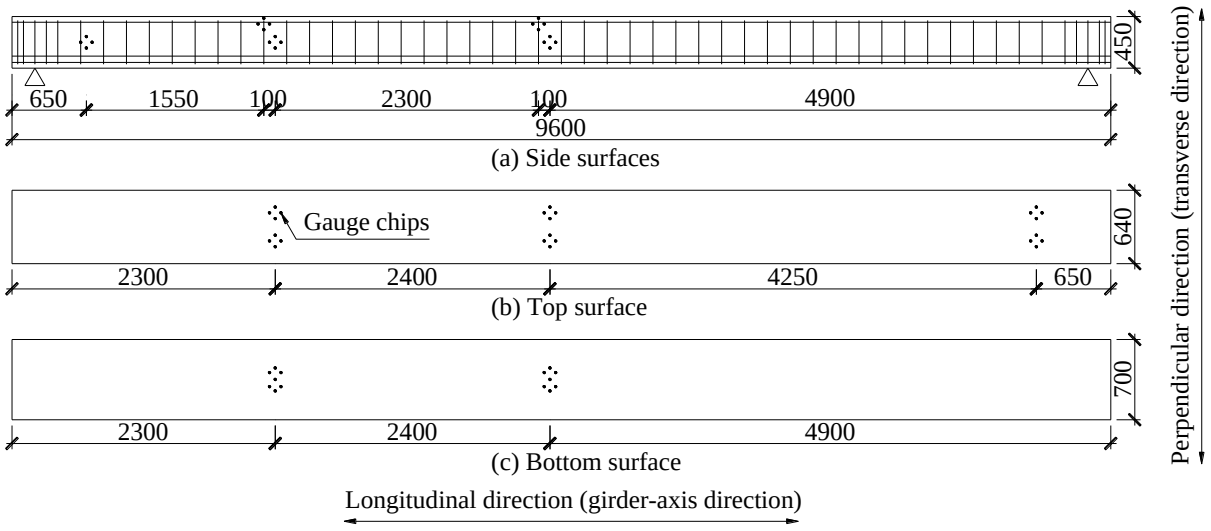


*Figure 2.7 Measurement locations (unit: mm).*

(a) Contact micron strain gauge (b) Gauge chip setup

*Figure 2.8 Expansion rate measurement.*

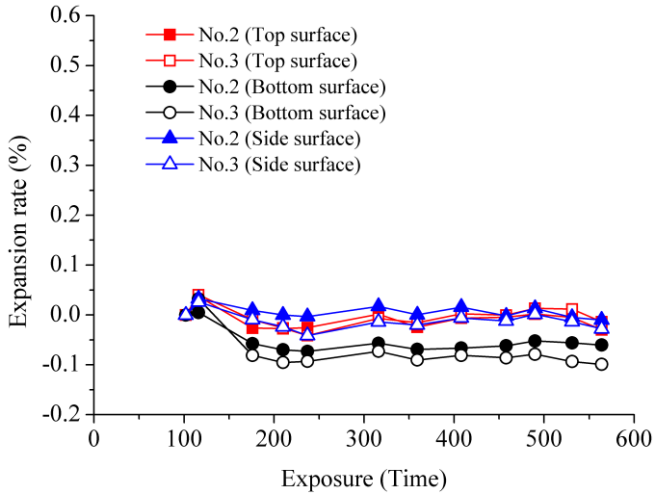


*Figure 2.9 Variation of expansion rate in longitudinal direction.*

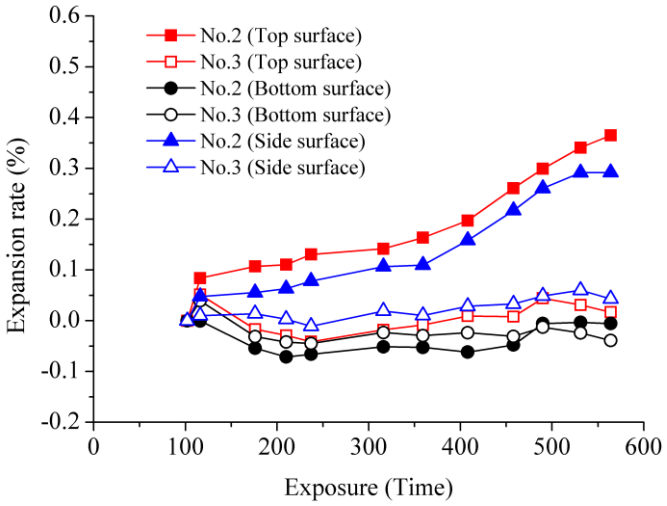


*Figure 2.10 Variation of expansion rate in transverse direction.*

## 2.4 Loading test

### 2.4.1 Testing method

Regarding the test setup, as shown in **Fig. 2.11**, each specimen with a span length of 9200 mm was subjected to the four-point bending test in which loads were applied at two points in the middle of the span. The testing girder was simply supported by two round steel bars. In addition, measurement items were load, deflection (vertical direction), crack development (girder axis direction) and concrete surface strain. The arrangement of measurement points is also summarized in this figure.

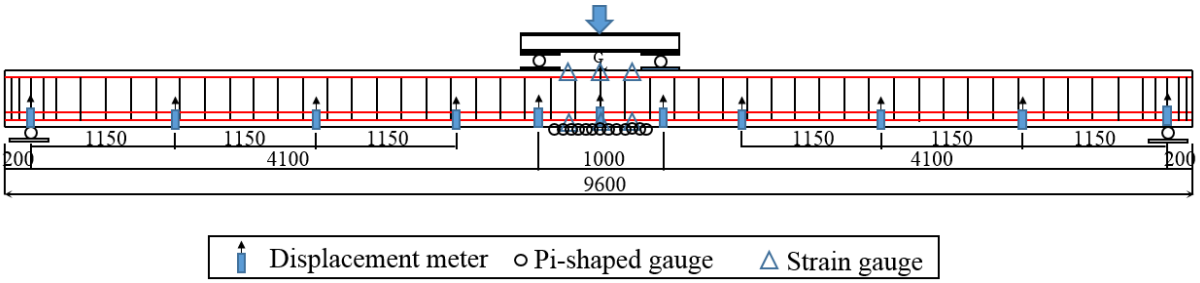


*Figure 2.11 Overview of loading test setup (unit: mm).*

### 2.4.2 Load – displacement relationship

**Figure 2.12** shows the relationship between applied load and vertical displacement at the span center of girders No.2 and No.3. As references, the design values of crack initiation load (126kN) and the bending fracture load (291kN) are also indicated in this figure. As a result of an examination of structural behavior in the elastic range, there was a difference of about 10% in the flexural rigidity between two girders. Specifically, the flexural rigidity of girders No.2

and No.3 were calculated as 11.5 kN/mm and 12.8 kN/mm when the applied load reached 50 kN, respectively. As the results of the loading tests, the final load of girders No.2 and No.3 were recorded as ~312 kN and ~330 kN, respectively, which causing failure in the upper extreme fiber of concrete as showed in **Fig. 2.13(a)–(b)**. Therefore, the load-carrying capacity of the girder without fly ash (No.2) was smaller by about 5% than that of the girder with fly ash (No.3). Compared to the specimen mixed with fly ash, the toughness of girder No.2 was deteriorated by the influence of ASR. This 5% reduction in the loading capacity is consistent with results of previous studies conducted in actual bridges [32,37]. However, a prior research of Onozato et al. [36] proved that the flexural strength did not decrease because the expansion of ASR was restrained by prestressing force. This outcome was not confirmed in the present study.

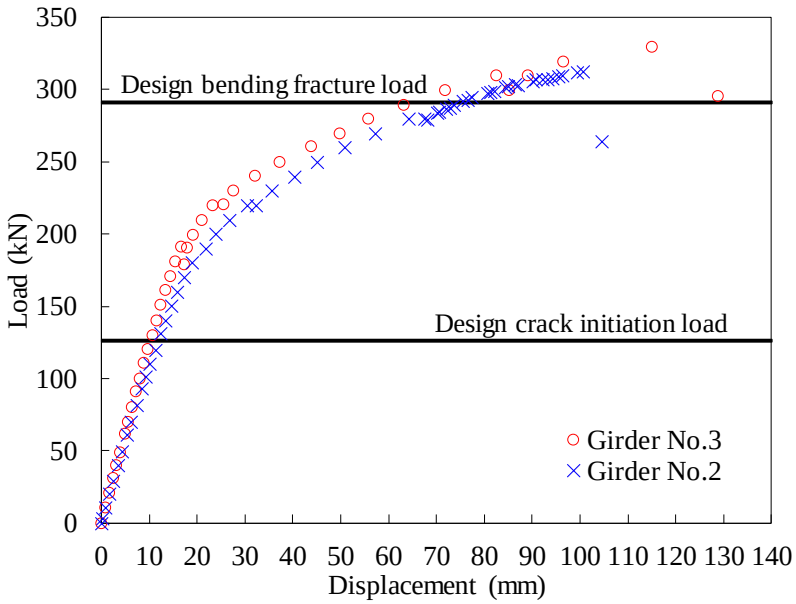


*Figure 2.12 Load-displacement relationship at midspan.*

(a) Girder No.3 (b) Girder No.2

*Figure 2.13 Compressive failure mode at the span center of girders at the final loads.*

The load-strain relationships of concrete on the top and bottom surfaces at the span center are presented in **Fig. 2.14**. From results of the experiment, the crack initiation load of girder No.2 was lower than of girder No.3 (170kN compared to 190kN, respectively). Although a slight

difference in structural behavior between two girders was observed in the elastic range, after the generation of initial crack, the strain of concrete on the upper edge (compression zone) of girder No.2 increased in higher rate in comparison to girder No.3. Furthermore, the neutral axis depth from the top edge in the elastic range was calculated to be 227.5 mm for girder No.2 and 228.7 mm for girder No.3, which was close to the effective area depth of concrete estimated as 228.2 mm. Therefore, ASR-induced cracks on the top and the side surfaces of girder No.2 did not affect the moment of inertia in the elastic region significantly.

Furthermore, in a comparison to the design, it is revealed that both specimen performed higher values in both crack initiation load and bending fracture load. Therefore, even if many cracks owing to ASR appeared on the girders, the steel strands were not broken and corroded after the exposure period. In addition, the bonding separation between steel and concrete did not occur. Although the load-carrying capacity was not significantly deteriorated, it is necessary to establish a maintenance management for these specimens to avoid further damage.

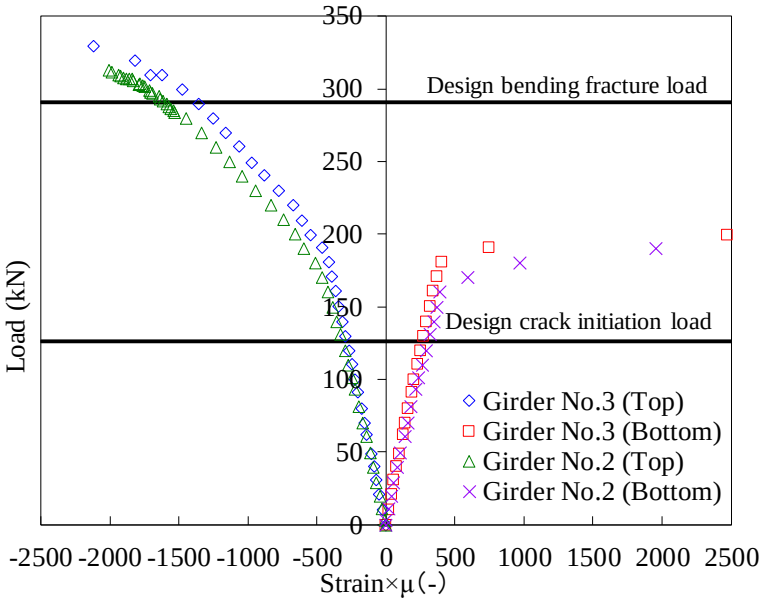


*Figure 2.14 Load-strain relationship.*

### 2.4.3 Crack observation after the loading test

**Figure 2.15(a)–(b)** shows crack patterns after the loading test of girder No.2 and No.3. Regarding figures of side surfaces, a selected mesh size was 100 mm for vertical direction (50 mm mesh was used for only the top fiber) and was 200 mm for girder-axis direction. As shown in **Fig. 2.15**, red lines express cracks owing to the load test, and black lines express stripping parts at midspan. The maximum crack interval in pure bending areas of the specimens was approximately 230 mm. Another attractive result was the development of flexural cracks during the test. Since there were many longitudinal cracks caused by ASR on the top and side surfaces

of girder No.2, vertical cracks owing to applied loads did not continuously propagate upward (**Fig. 2.16**). Therefore, it was thought that longitudinal cracks interrupted the development of bending cracks. However, an investigation of cut cross sections, which is described in the next section, shown that due to the shallow depth, longitudinal cracks could not hinder the progress of bending cracks.

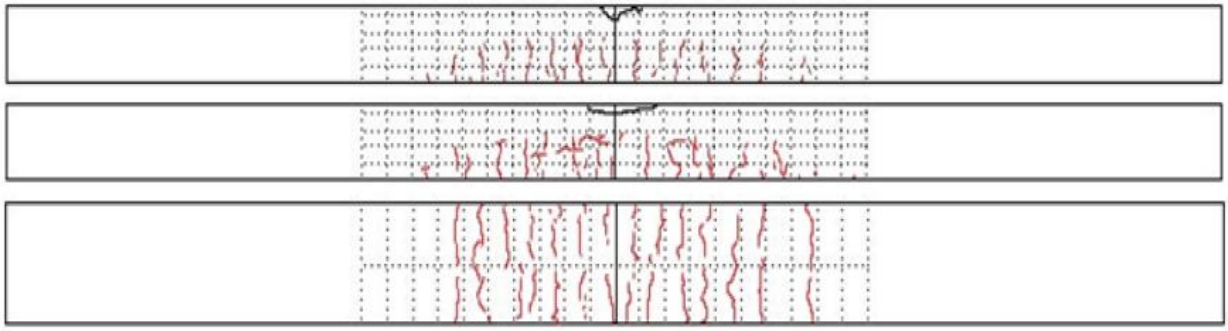

(a) Girder No.2

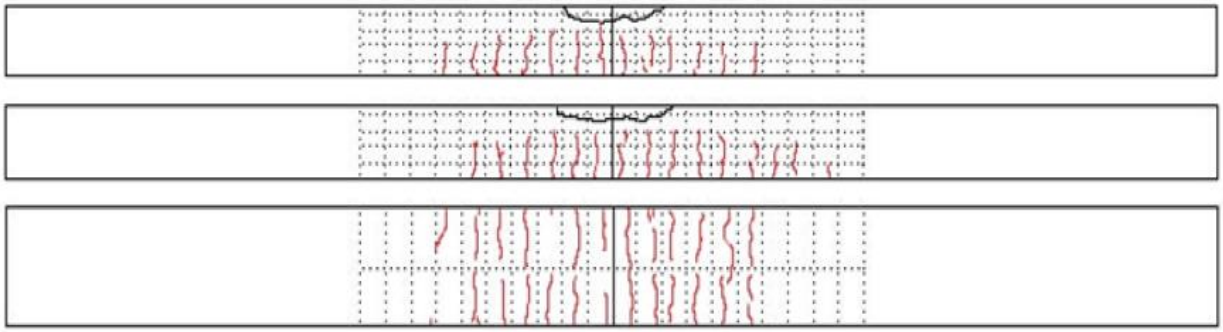

(b) Girder No.3

*Figure 2.15 Crack pattern due to loading test (from top to down: north-side, south-side and bottom surfaces).*

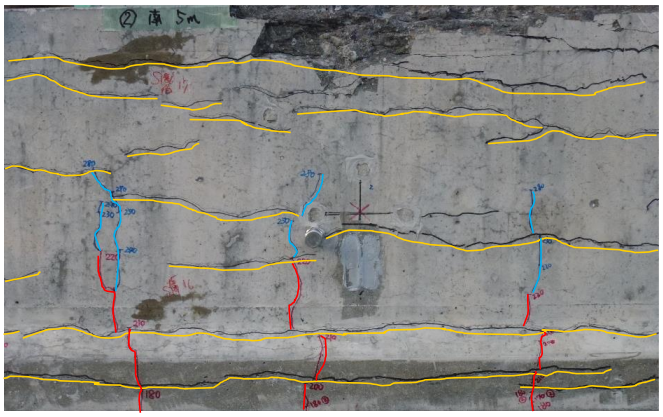

*Figure 2.16 Crack pattern at the span center after loading test.*

### 2.4.4 Investigation of the cross-section

To evaluate the condition of inner surfaces after the load test, each girder was cut into three pieces with lengths of 3150 mm, 3300 mm and 3150 mm by a wire saw. **Figure 2.17** shows a cut surface of girder No.2 between its support and the span center. In this figure, yellow lines show ASR-induced cracks, and green lines show transverse cracks observed on the upper side of tendons in the compression area. Red dots indicate PC strands. From observation results, the depth of ASR-induced cracks along the girder-axis direction varied from 5 to 20 mm on the side surfaces and the top surface, whereas no crack was found out in the area surrounded by stirrups. Moreover, no breaking of tendons was confirmed, whereas transverse cracks were significantly observed on the upper side of tendons in the compression area. After the bending test, for ascertaining the corrosion condition of PC strands, peeled concrete areas of both samples were taken away. However, no steel corrosion could be observed.


*Figure 2.17 A cut cross-sectional view of girder No.2.*

## 2.5 Diagnosis ASR-induced deteriorations using drilled cores

### 2.5.1 Overview of experiment setup

After the girder had been cut into three pieces, cylindrical core samples were collected from both girders at positions near support (end part) and at positions around the inner area between two pieces (central part) so as to investigate the mechanical properties of concrete. At each area, six cores along the girder-axis direction (longitudinal direction) and six cores along the direction perpendicular to the girder-axis direction (transverse direction) were collected for the compression tests. In addition, four more samples were collected at central area in both investigate directions for the expansion tests. Each concrete core with a diameter of 55 mm and a length of 110 mm was taken from the surface of concrete about 30 mm. **Figure 2.18(a)–(c)** shows the sampling position. The relation between the reactivity of aggregate and ASR deterioration degree was examined by the immersion method in 1N · NaOH solution [38–41]. Furthermore, the generation of ASR gel, which becomes yellow-green under ultraviolet (UV) light, was observed by the fluorescent visualization method [42]. As another observation, thin

slices (thickness 20μm) of concrete were taken from the cores and helped investigate the reactive condition of aggregates and the generation of fine cracks on the surface and inside of the cores.

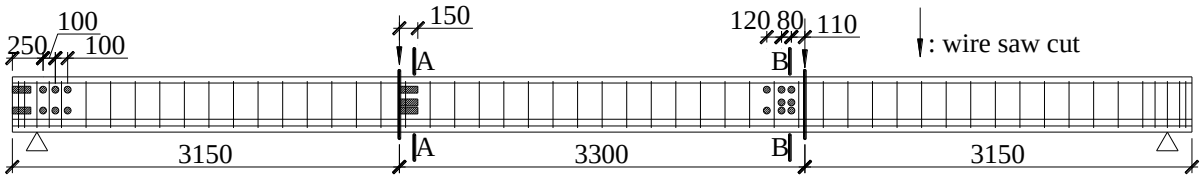


(a) Wire saw cutting positions

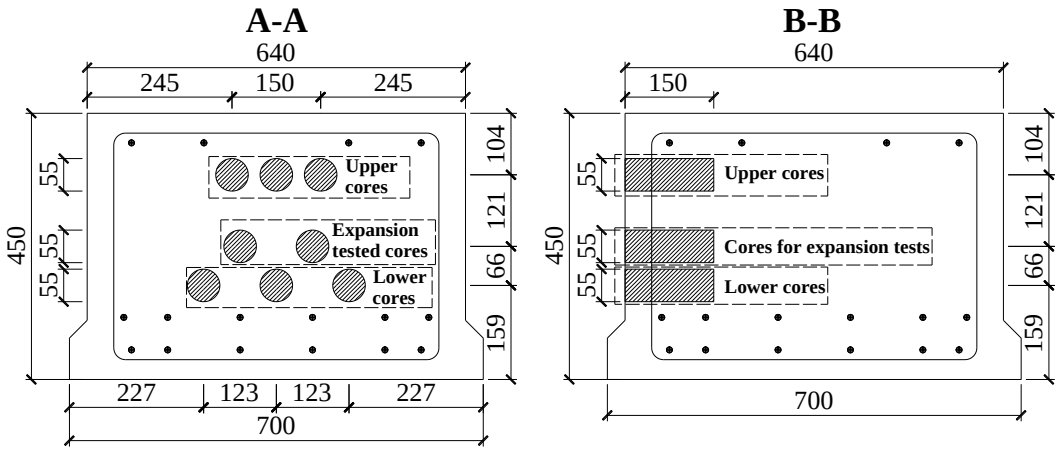


(b) longitudinal direction (c) transverse direction

*Figure 2.18 Test piece sampling locations (Unit: mm).*

### 2.5.2 Cracks and the reactivity of aggregate

**Figure 2.19(a)–(d)** indicates observation results of concrete cores of both girders obtained by the fluorescent method. The tested cores were the upper cores taken longitudinally in the central parts of the girders. As the results, regarding the specimen of girder No.2, the ASR gel under UV light appeared as yellow-green around andesite particles. However, no fluorescence was observed on samples taken from girder No.3. In addition, **Figure 2.20** shows observation results by a polarized microscope. Regarding girder No.2, andesite particles from sand and gravel of the Joganji River reacted strongly, and many fine cracks (about 0.02 mm in width) occurred from broken pieces of aggregates to cement paste. Conversely, andesite particles reacted slightly while no trace of ASR was observed with respect to girder No.3 with fly ash. In both girders, no formation of ASR gel was found in the surface layer (about 20 mm) of both specimens. It was inferred that ASR was suppressed in the surface layer of concrete due to alkali outward flow and immobilization under alternation of drying and moistening processes [43].

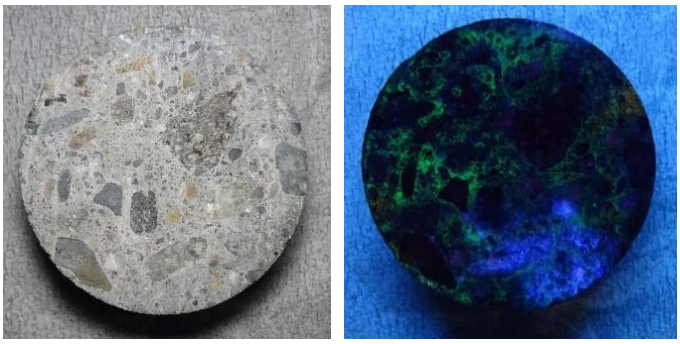

(a) white light (girder No.2) (b) UV light (girder No.2)

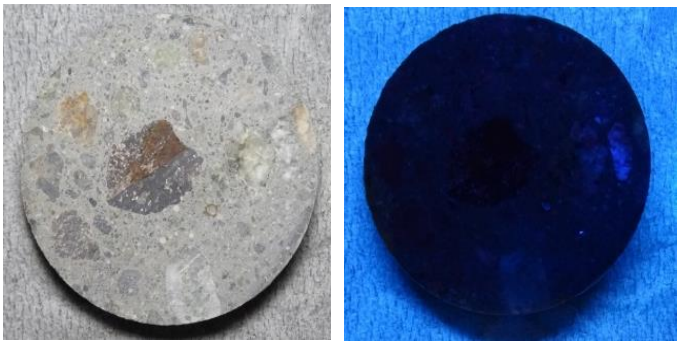

(c) white light (girder No.3) (d) UV light (girder No.3)

*Figure 2.19 Observation results of concrete cores by gel fluorescence method.*

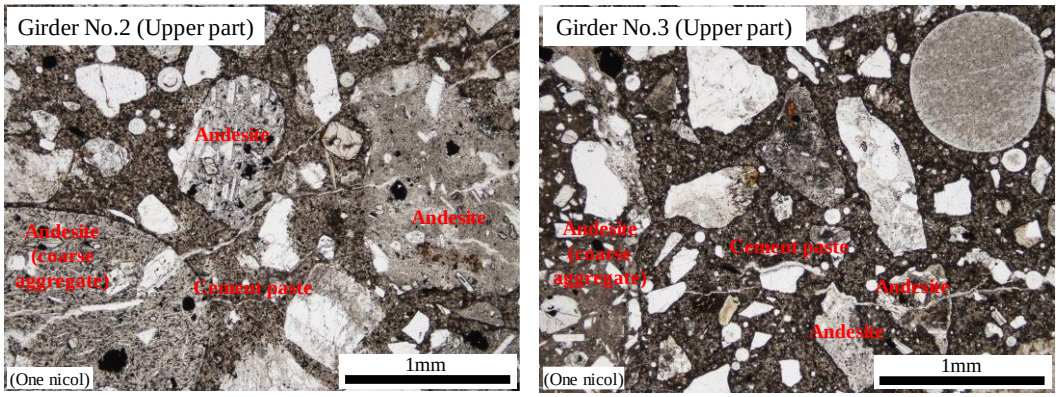


*Figure 2.20 Observation result of core slice by polarized microscope.*

### 2.5.3 Expansion rate of concrete cores

The expansion rate of core obtained by the immersion method in 1N NaOH solution is indicated in **Fig. 2.21**. After one and a half years of outdoor exposure, because there were a large number of unreacted andesite particles, the cores of girder No.2 expanded significantly up to 0.5% after being immersed in 1N NaOH solution maintained at 80 ºC. According to ASTM C1260 [38], a specimen with an expansion rate of 0.2% or more after two weeks of soaking should be evaluated as "harmful". Therefore, both specimens were judged as "harmful" in this study. From

**Fig. 2.21**, the expansion rate of girder No.2 in the transverse direction was higher than in the longitudinal direction. This result is considered to be influenced by the difference in generation degree of fine cracks due to the collecting direction and the influence of restraint of PC tendons, that is to say, by the difference in the permeability of NaOH solution at the time of the test. The effects of the confinement degree due to prestressing on mechanical properties of concrete are discussed in the next section. Regarding a reference threshold value of hydroxide ion ($OH^-$) concentration in a pore solution for ASR initiation, Diamond [44] proposed a value of 250 mmol/l (0.25 N), which was also confirmed and evaluated by other researchers [45–48]. Therefore, it can be considered that unreacted other particles also reacted and thereby accelerated ASR when the concrete cores were soaking in 1N NaOH solution. This conclusion is useful in diagnosing ASR deterioration of core utilizing the immersion method in 1N NaOH solution at 80 ºC. Meanwhile, regarding girder No.3, because of a slight generation of ASR, together with a low penetration of alkaline solutions, and an additional effect of alkaline adsorption of CSH with a low C/S ratio generated during pozzolan reaction, the measured expansion rate was remarkably lower than that of girder No.2.

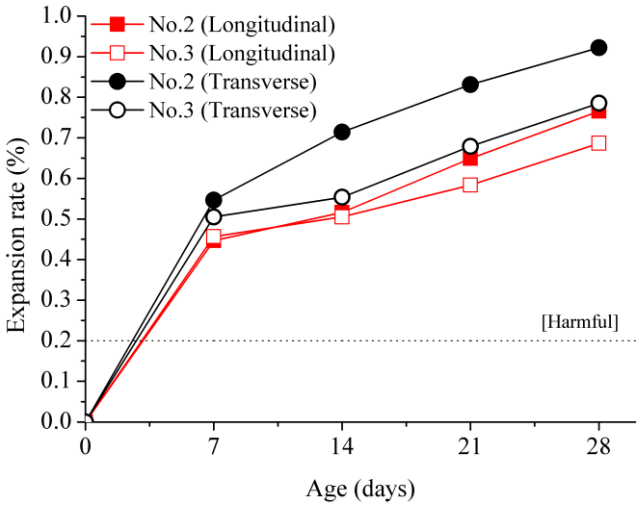


*Figure 2.21 Expansion rate of cores.*

### 2.5.4 Mechanical properties of cores and ultrasonic wave propagation velocity

**Table 2.5** indicates average values of compressive strength, static elastic modulus and ultrasonic wave velocity of concrete cores. Both the compressive strength and the elastic modulus of cores taken from girder No.2 were smaller than those from girder No.3. Owing to the influence of fly ash content, the compressive strength and the elastic modulus of girder No.3 were about 1.3 to 2 times greater than those of girder No.2. Compared to the compressive strength at 28 days (**Table 2.5**), the compressive strength of girder No.2 decreased significantly due to deteriorations caused by ASR. A previous study [49] pointed out that due to the influence

of restraint of PC tendons, the compressive strength of concrete depended on direction when taking samples, this study also found out the same conclusion. Specifically, when comparing the test results of the upper part and the lower part of a cross section, the compressive strength and the static elastic modulus of cores taken from the lower part in the girder-axis direction (near two lower layers of PC strands) were larger than those taken from the upper one. Moreover, as compared to results obtained from concrete samples of the central part, both the compressive strength and the elastic modulus of the end part were almost lower. The difference in both mechanical properties came up to approximately 30% on concrete cores collected in the longitudinal direction of girder No.2. In addition, because of the effect of restraining stress of PC strands together with the low expansion rate of concrete, the concrete samples collected longitudinally in the central part of girder No.2 performed higher compressive strength in comparison with the samples taken in the transverse direction.

*Table 2.5 Mechanical properties of core and ultrasonic wave propagation velocity.*

| Core collecting position | | | Compression strength ($N/mm^2$) | | Modulus of elasticity ($kN/mm^2$) | | Ultrasonic wave propagation velocity (m/s) | |
|---|---|---|---|---|---|---|---|---|
| | | | No.2 | No.3 | No.2 | No.3 | No.2 | No.3 |
| End part | longitudinal direction | Upper part | 49.9 | 79.4 | 16.8 | 28.9 | 3870 | 4310 |
| | | Lower part | 53.3 | 102.2 | 20.9 | 36.5 | 3990 | 4560 |
| | transverse direction | Upper part | 62.0 | 94.5 | 19.2 | 34.2 | 3970 | 4530 |
| | | Lower part | 69.4 | 103.2 | 18.2 | 38.4 | 3880 | 4790 |
| Central part | longitudinal direction | Upper part | 68.0 | 102.0 | 24.2 | 41.1 | 4130 | 4770 |
| | | Lower part | 75.7 | 89.5 | 27.8 | 42.9 | 4170 | 4800 |
| | transverse direction | Upper part | 43.4 | 109.1 | 14.5 | 36.8 | 3820 | 4620 |
| | | Lower part | 58.5 | 111.4 | 18.9 | 39.3 | 3900 | 4780 |

The relationship between compressive strength and static elastic modulus/compressive strength ratio of the concrete cores is shown in **Fig. 2.22**. In this figure, it is cleared that if the ASR damage in concrete become more severe, the measurement points will get closer to the origin from the curve showing healthy concrete [50]. In the case of girder No.3 with fly ash, the obtained results were almost close to the healthy curve. Meanwhile, all points of girder No.2 distributed away from the curve and toward the origin. It was considered that the influence of fine cracks owing to ASR and peeling of the aggregate interface was reflected by the decrease in compressive strength and static elastic modulus. **Figures 2.23 and 2.24** show the relationship between ultrasonic wave velocity with compressive strength and static elastic modulus of

concrete cores, respectively. Because ultrasonic wave propagation can be easily measured on site, it is commonly used in structural health evaluation. As can be seen in **Figs. 2.23 to 2.24**, along with the ASR progression, the compressive strength and the static elastic modulus decrease linearly, and both parameters have a substantially proportional relationship to the ultrasonic wave velocity.

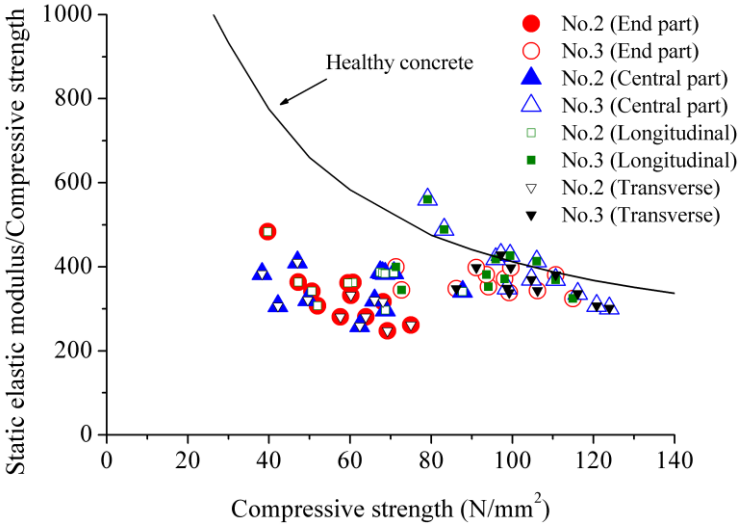


*Figure 2.22 Relationship between compressive strength and static elastic modulus/compressive strength ratio.*

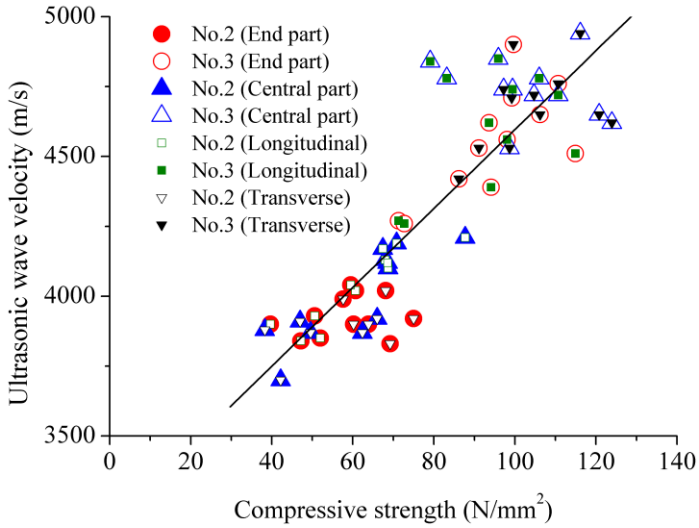


*Figure 2.23 Relationship between compressive strength of core and ultrasonic propagation velocity.*

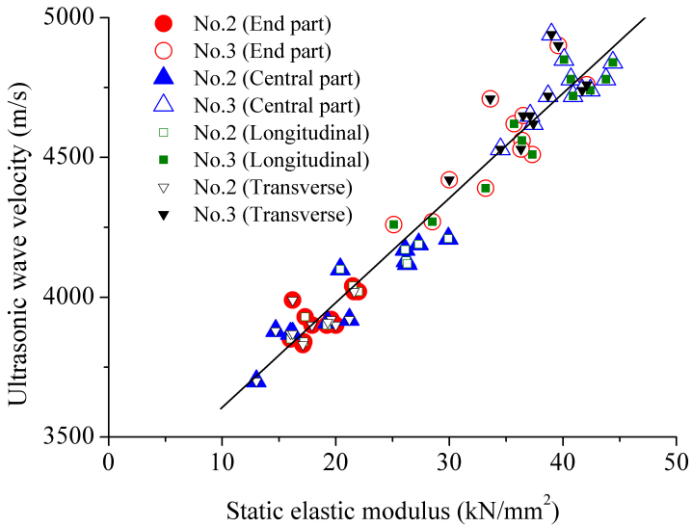


*Figure 2.24 Relationship between static elastic modulus of core and ultrasonic propagation velocity.*

### 2.5.5 Recommendations on diagnosis of ASR degradation using concrete cores

From the test results, it is necessary to pay attention to two points when studying the relationship between the compressive strength, the static elastic modulus and the ultrasonic propagation velocity.

(1) The first point is that the compressive strength of core taken from the transverse direction of central part of ASR-affected girder reduced by about 30% as compared to the value measured from the longitudinal direction. Moreover, when comparing results obtained in the central and the end parts, except for some measurement results, the concrete cores of the end part have lower mechanical properties than of the central part. Especially, with respect to concrete cores collected in the longitudinal direction of girder No.2, the difference in both mechanical properties came up to approximately 30%.

(2) The second point is that the compressive strength and the static elastic modulus of concrete cores might decrease due to the effects of water and stress release during the coring. Therefore, when calculating load-carrying capacity and reinforcement design for ASR-degraded PC girders, it is necessary to perform an appropriate correction according to the constraint degree owing to the prestress instead of using the measurement values of the cores directly.

Furthermore, as can be seen in **Fig. 2.25**, the difference in expansion rate between the upper and the lower sides of a girder induced a large deformation (upward warpage), and it might lead to new damage. Therefore, it is desirable to check the damage caused by local destruction at the girder end and by dismounting of PC anchoring parts simultaneously at the time of inspection for PC bridges. Regarding long-term prospects, further research should be carried out on the subject.

*Figure 2.25 Cracks occurred at the end of PC girder due to ASR-induced deformation.*

## 2.6 Conclusions

In this study, three PC girders, which were constructed and placed outside the laboratory, had been exposed to weather conditions for one and a half years. Girders No.1 and No.2 was affected by alkali-silica reaction while girder No.3 was kept at an inactive state with ASR acceleration due to the addition of fly ash. Then, using the destructive loading test, this study investigated the difference in load carrying capacity of two PC girders (girders No.2 and No.3) due to the presence or absence of fly ash. Moreover, after the destructive loading test, the effects of the sampling position and direction of the concrete core on changes in compressive strength, static elastic modulus, and ultrasonic wave propagation velocity were analyzed and discussed by collecting concrete cores from both PC girders affected by ASR deterioration. The main results obtained from this study are summarized as follows.

- ✓ After one and a half year of monitoring of cracks, an addition of fly ash played a significant role in mitigating the cracks caused by the expansion due to ASR.
- ✓ An increase of convex curvature was observed in the girder without fly ash. After monitoring period, the convex displacement increased up to ~13 mm before starting the load test with respect to girder No.2. Meanwhile, almost no change in convex curvature over time was observed in girder No.3 mixed with fly ash.
- ✓ An addition amount of fly ash not only increased the load bearing capacity by nearly 5% but also enhanced the initial bending stiffness of the objective PC girder by 10% after more than one year under ASR deteriorations.
- ✓ From observation results of cut cross-section after the loading test, the depth of ASR-induced cracks along the girder-axis direction varied from 5 to 20 mm on the side surfaces and the top surface. However, no crack was found out in the area surrounded by stirrups, and no breaking of tendons was confirmed.

- ✓ Regarding girder No.2, andesite particles from sand and gravel reacted strongly, and many fine cracks (about 0.02 mm in width) occurred from broken pieces of aggregates to cement paste. However, because of the slight reaction of andesite particles, no trace of ASR was observed on girder No.3.
- ✓ When the concrete cores of girder No.2 were soaking in 1N NaOH solution, unreacted andesite particles accelerated ASR leading to high expansion rate. Meanwhile, regarding girder No.3, the expansion rate was significantly low as compared to that of girder No.2.
- ✓ Proportional correlations between the compressive strength, the static elastic modulus and the ultrasonic propagation velocity of the core were found.

## 2.7 References

[1] T. Stanton, "Expansion of concrete through reaction between cement and aggregate," in *Proceedings of American Society of Civil Engineers 66*, 1940, pp. 1781–1811.

[2] S. A. Marfil and P. J. Maiza, "Deteriorated pavements due to the alkali-silica reaction: A petrographic study of three cases in Argentina," *Cem. Concr. Res.*, vol. 31, no. 7, pp. 1017–1021, 2001.

[3] A. Leemann, C. Thalmann, and W. Studer, "Alkali-aggregate reaction in Swiss tunnels," *Mater. Struct.*, vol. 38, no. 3, pp. 381–386, 2005.

[4] S.-H. Hong, S.-H. Han, and K.-K. Yun, "A Case Study of Concrete Pavement Deterioration by Alkali-Silica Reaction in Korea," *Int. J. Concr. Struct. Mater.*, vol. 1, no. 1, pp. 75–81, 2007.

[5] G. Gasparotto, G. M. Bargossi, F. Peddis, and V. Sammassimo, "A case study of alkali-silica reactions: Petrographic investigation of paving deterioration," *Period. di Mineral.*, vol. 80, no. 2, pp. 309–316, 2011.

[6] S. Hirono, Y. Ando, T. Satoh, K. Yamada, H. Kagimoto, and K. Torii, "ASR Found in Thailand and Tropical regions of southeast Asia," in *15th International Conference on Alkali-Aggregate Reaction*, 2016.

[7] K. Yamada, S. Hirona, and T. Miyagawa, "New Findings of ASR Degradation in Japan," in *13th International Congress on the Chemistry of Cement.*, 2011, pp. 1–7.

[8] K. Torii, K. Okuyama, K. Kuzume, and T. Sasatanai, "Monitoring and strengthening methods of bridge pier seriously damaged by alkali-silica reaction," in *Proc. of Inter. Conf. on CONSEC'07*, 2007, pp. 787–794.

[9] K. Torii, "The characteristic feature of fracture of steel reinforcement in ASR-deteriorated concrete structures," *Int. J. Corros. Eng.*, vol. 59, no. 4, pp. 59–65, 2010.

[10] K. Torii, I. Prasetia, T. Minato, and K. Ishii, "The feature of cracking in prestressed concrete bridge girders deteriorated by alkali-silica reaction," in *Proceedings of 14th*

*ICAAR Conference*, 2012.

[11] T. Katayama, M. Tagami, Y. Sarai, S. Izumi, and T. Hira, "Alkali-aggregate reaction under the influence of deicing salts in the Hokuriku district, Japan," in *Materials Characterization*, 2004, vol. 53, no. 2–4, pp. 105–122.

[12] K. Torii, T. Kubo, C. Sannoh, and M. Kanitani, "The Strengthening of an ASR-affected Water Intake Tower in a Hydro-Electric Dam by Using Post-Tensioned Tendons and the Long-term Monitoring of Tower," *J. Adv. Concr. Technol.*, vol. 14, pp. 384–396, 2016.

[13] T. Kubo, T. Shibata, C. Sannoh, and K. Torii, "The Reinforcement of an ASR Affected Intake Tower Using Post-Tensioned Tendons," in *15th International Conference on Alkali-Aggregate Reaction*, 2016.

[14] G. Giaccio, R. Zerbino, J. M. Ponce, and O. R. Batic, "Mechanical behavior of concretes damaged by alkali-silica reaction," *Cem. Concr. Res.*, vol. 38, no. 7, pp. 993–1004, 2008.

[15] K. Ono, "Damaged concrete structures in Japan due to alkali silica reaction," *Int. J. Cem. Compos. Light. Concr.*, vol. 10, no. 4, pp. 247–257, 1988.

[16] M. a Tordoff, "Assessment of pre-stressed concrete bridges suffering from alkali-silica reaction," *Cem. Concr. Compos.*, vol. 12, no. 3, pp. 203–210, 1990.

[17] F. Gong, Y. Takahashi, and K. Maekawa, "Strong coupling of freeze-thaw cycles and alkali silica reaction - multi-scale poro-mechanical approach to concrete damages," *J. Adv. Concr. Technol.*, vol. 15, pp. 346–367, 2017.

[18] Y. Takahashi, S. Ogawa, Y. Tanaka, and K. Maekawa, "Scale-dependent ASR expansion of concrete and its prediction coupled with silica gel generation and migration," *J. Adv. Concr. Technol.*, vol. 14, no. 8, pp. 444–463, 2016.

[19] V. E. Saouma, *Numerical modeling of AAR*. Taylor & Francis Group, London, 2014.

[20] Y. Kunitomi, A. Ishii, J. Xin, and K. Torii, "Characteristic of Load-bearing capacity of PC Beams using ground granulated blast furnace slag by ASR accelerated exposure test," *J. Prestress. Concr.*, vol. 57, no. 3, pp. 68–74, 2015.

[21] K. Torii, T. Kubo, C. Sannoh, and M. Kanitani, "The alkali-silica reactivity of andesitic river aggregates and ASR mitigating effect by using fine fly ashes.," in *15th International Conference on Alkali-Aggregate Reaction*, 2016.

[22] M. H. Shehata and M. D. A. Thomas, "Effect of fly ash composition on the expansion of concrete due to alkali-silica reaction," *Cem. Concr. Res.*, vol. 30, no. 7, pp. 1063–1072, 2000.

[23] T. Hashimoto and K. Torii, "The development of highly durable Concrete using classified fine fly ash in Hokuriku district," *J. Adv. Concr. Technol.*, vol. 11, pp. 312–321, 2013.

[24] T. Hashimoto and K. Torii, "The assessment on ASR of aggregates and ASR mitigation effect by fine fly ash," *Concr. Aust.*, vol. 42, no. 2, pp. 65–71, 2015.

[25] S. Yamamura, M. Sakurada, K. Kobayashi, and K. Torii, "Application of fly ash concrete

to prestressed concrete bridges," *Cem. Concr.*, vol. 828, pp. 22–27, 2016.

[26] R. Narayan Swamy and M. M. Al-Asali, "Effect of alkali-silica reaction on the structural behavior of reinforced concrete beams," *ACI Struct. J.*, vol. 86, no. 4, pp. 451–459, 1989.

[27] S. Fan and J. M. Hanson, "Effect of alkali silica reaction expansion and cracking on structural behavior of reinforced concrete beams," *ACI Struct. J.*, vol. 95, no. 5, pp. 498–505, 1998.

[28] T. Miyagawa, K. Seto, K. Sasaki, Y. Mikata, K. Kuzume, and T. Minami, "Fracture of Reinforcing Steels in Concrete Structures Damaged by Alkali-Silica Reaction- Field Survey, Mechanism and Maintenance-," *J. Adv. Concr. Technol.*, vol. 4, no. 3, pp. 339–355, 2006.

[29] J. Wang and H. Morikawa, "Study on shear behavior of deteriorated RC beams due to alkali-silica reaction," in *37th Conference on our world in concrete & structures*, 2012, p. 10 pages.

[30] S. Hajighasemali, A. Ramezanianpour, and M. Kashefizadeh, "The effect of alkali-silica reaction on strength and ductility analyses of RC beams," *Mag. Concr. Res.*, vol. 66, no. 15, 2014.

[31] K. Kobayashi, S. Inoue, T. Yamasaki, and K. ichi Nakano, "Alkali aggregate reaction in prestressed concrete beams," *Int. J. Cem. Compos. Light. Concr.*, vol. 10, no. 4, pp. 233–240, 1988.

[32] Y. Takebe, T. Tokoyama, H. Yonekawa, K. Nakamura, and T. Miyagawa, "Strengthening effect on prestressed concrete members affected by alkali-silica reaction (ASR)," in *Third International Conference on Sustainable Construction Materials and Technologies*, 2013.

[33] Y. Hiroi, T. Yamamoto, Y. Toda, H. Manabe, and T. Miyagawa, "Experimental and analytical studies on flexural behaviour of post-tensioned concrete beam specimen deteriorated by alkali-silica reaction (ASR)," in *15th International Conference on Alkali-Aggregate Reaction*, 2016.

[34] T. Yokoyama, T. Miyagawa, Y. Hiroi, T. Yamamoto, H. Manabe, and T. Ookubo, "Long-term deterioration of quasi-actual scale prestressed concrete beam due to alkali-silica reaction," in *15th International Conference on Alkali-Aggregate Reaction*, 2016.

[35] Japan Meteorological Agency, "http://www.jma.go.jp/jma/index.html." .

[36] M. Onozato, T. Kobayashi, S. Ogawa, and Y. Matsubayashi, "Flexural bearing capacity of prestressed concrete damaged by ASR," *Proc. Symp. Dev. Prestress. Concr.*, vol. 15, pp. 97–100, 2006.

[37] J. Tomiyama, K. Yamada, K. Kaneda, S. Iraha, and T. Oshiro, "ASR diagnosis by petrographic investigation and evaluation of mechanical performance of ASR deteriorated pretensioned PC beam," *J. Japan Soc. Civ. Eng. Ser. E2 (Materials Concr.*

*Struct.*, vol. 67, no. 4, pp. 578–595, 2011.

[38] ASTM Committee C09.26, "ASTM C1260-14 Standard Test Method for Potential Alkali Reactivity of Aggregates ( Mortar-Bar Method)," in *Annual Book of ASTM Standards Volume 04.02*, 2014, pp. 1–5.

[39] R. E. Oberholster and G. Davies, "An accelerated method for testing the potential alkali reactivity of siliceous aggregates," *Cem. Concr. Res.*, vol. 16, no. 2, pp. 181–189, 1986.

[40] B. Fournier and M. A. Bérubé, "Application of the NBRI accelerated mortar bar test to siliceous carbonate aggregates produced in the St. Lawrence Lowlands (Quebec, Canada) part 2: Proposed limits, rates of expansion, and microstructure of reaction products," *Cem. Concr. Res.*, vol. 21, no. 6, pp. 1069–1082, 1991.

[41] B. Fournier and M. A. Bérubé, "Application of the NBRI accelerated mortar bar test to siliceous carbonate aggregates produced in the St. Lawrence lowlands (Quebec, Canada) part 1: Influence of various parameters on the test results," *Cem. Concr. Res.*, vol. 21, no. 5, pp. 853–862, Sep. 1991.

[42] C. Sannoh, T. Maruyama, H. Yamato, and K. Torii, "Development of simple ASR diagnostic technique by gel fluorescence method," *Proc. Japan Concr. Inst.*, vol. 35, no. 1, pp. 973–978, 2013.

[43] M. Kawamura, *Alkali-silica reaction in concrete*. Seiunsha, 2010.

[44] S. Diamond, "ALKALI REACTIONS IN CONCRETE-PORE SOLUTION EFFECTS," in *6th International Conference. Alkalis in Concrete. Research and Practice. Copenhagen*, 1983, pp. 155–166.

[45] Rasheeduzzafar and S. Ehtesham Hussain, "Effect of microsilica and blast furnace slag on pore solution composition and alkali-silica reaction," *Cem. Concr. Compos.*, vol. 13, no. 3, pp. 219–225, 1991.

[46] H. Kagimoto, M. Sato, and M. Kawamura, "Evaluation of the degree of deterioration in asr damaged concretes and analyses of their pore solutions," *J. Japan Soc. Civ. Eng.*, vol. 46, no. 641, pp. 241–251, 2000.

[47] H. Kagimoto, M. Sato, and M. Kawamura, "OH- ion concentration limit of pore solution of mortar using 2, 3 different reactive aggregates," *Proc. Japan Concr. Inst.*, vol. 23, no. 2, pp. 589–594, 2001.

[48] Y. Kawabata, K. Yamada, and H. Matsushita, "Relation of phase composition of cement hydrates with supplementary cementitious materials to the suppressing effect on ASR expansion," *J. Japan Soc. Civ. Eng. Ser. E2 (Materials Concr. Struct.*, vol. 69, no. 4, pp. 402–420, 2013.

[49] T. Inagaki, Y. Obana, T. Ishii, and K. Torii, "Mechanical Properties of Core Collected from ASR Degraded PC Beam Specimen," *Proc. Japan Concr. Inst.*, vol. 31, no. 1, pp. 1237–1242, 2009.

[50] Japan Society of Civil Engineers Concrete Committee, *Standard specifications for concrete structures: design code*. Concrete committee, 2012.

# Chapter | 3

# Nondestructive Damage Detection in Deteriorated Girders Using Changes in Nodal Displacement

## 3.1 Theoretical background

### 3.1.1 Displacement assurance criterion (DAC)

This section proposes a damage detection method to identify the occurrence of damage by evaluating correlations among measured displacement data. It can be noticed that a damaged girder provides different deflections compared to the original one, because of its deteriorated flexural rigidity [1]. Assuming the nodal deflections of a finite-element model described by a displacement vector $u = [u_1 \ u_2 \ \cdots \ u_n]^T$, the static equilibrium formula of the structure at the intact state is expressed by the following equation:

$$F = Ku \tag{3.1}$$

where $K$ is a $n \times n$ stiffness matrix and $F$ depicts an $n \times 1$ applied static force vector. Then, the displacement vector u can be obtained by $u = K^{-1}F$. Therefore, any structural changes are associated with changes in the displacement vector $u$. Specifically, if the structure has been damaged by environmental conditions or applied loads, the structural stiffness matrices are modified, and the measured displacements at the deteriorated state of the structure do not correspond with the measured displacements at the intact state.

In this study, a novel damage indicator, DAC, is proposed and utilized for detecting the existence of a stiffness loss. DAC illustrates the degree of relationship between two displacement curves at different states of a structure and it can be computed by **Eq. (3.2)** using the normalized displacement at each observation point:

$$DAC = \frac{\left(\sum_{j=1}^{n+1} \psi_{Fj}\psi_{Hj}\right)^2}{\sum_{j=1}^{n+1} \psi_{Fj}{}^2 \sum_{j=1}^{n+1} \psi_{Hj}{}^2} \tag{3.2}$$

where $\psi_{Fj}(j=1\sim n+1)$ is the normalized displacement of the $j^{th}$ point caused by the external applied static load at a reference state. $\psi_{Hj}(j=1\sim n+1)$ is the normalized displacement of the $j^{th}$ point caused by the external applied static load at a different state of the structure, and n indicates the number of observation points. In this study, a normalized displacement curve at the elastic state is considered as the reference curve. In the case where the two normalized displacement curves are identical, the DAC value would be equal to unity, while any

degradation in structural properties would generate a value less than unity.

### 3.1.2 Displacement-based index (DBI)

As it was mentioned in the literature review, various damage detection techniques can be utilized for identifying damages in a structure [1–25]. For instance, changes in the displacement curvature [1,23,24] and the strain energy method [25] are sensitive and can be employed to localize the damage region. To evaluate the feasibility of directly using the displacement at each monitored position for verifying the occurrence and location of structural damage, this study performs parametric analyses on a numerical model of a PC girder that undergoes different damage scenarios. From the stand point of the correlation between nodal deflections and degradation of structural stiffness, a new damage identification method using a displacement-based index, DBI, is proposed. In particular, **Eq. (3.1)** illustrates the correlation of displacement with structural stiffness. Therefore, a change in structural stiffness at a section subjected to deterioration leads to a variation in deflection at that location. The relationship between the properties of damage and the reduction of the Young's modulus of a structure has been proved by the previous research [26]. In this study, it is assumed that there is a decrease in the Young's modulus, which is associated with the increase in the degree of damage at each observed section. For investigating the changes in the static response owing to the presence of damage, the displacement of some marked points of the objective girder is measured. Then, the DBI values are calculated to identify locations and occurrences of stiffness losses. Based on the former considerations, the following damage detection algorithm is proposed:

• A girder subjected to an arbitrarily applied load is treated as it is divided into a finite number of elements *n* (*n+1* nodes), as shown in **Fig. 3.1**.

• The nodal displacements are calculated by commercial finite-element software for both the healthy girder and the deteriorated one, which contains a hypothetical damage in an arbitrary segment.

• Assuming the coordinate geometry of *u* and *x* shown in **Fig. 3.2**, then nodal displacements of the intact girder and the deteriorated one can be illustrated as **Eqs. (3.3) and (3.4)**, respectively:

$$[x, u_i] = [(x_1, u_{i1}), (x_2, u_{i2}), \cdots, (x_{n+1}, u_{in+1})] \tag{3.3}$$

$$[x, u_d] = [(x_1, u_{d1}), (x_2, u_{d2}), \cdots, (x_{n+1}, u_{dn+1})] \tag{3.4}$$

• In this study, the DBI values obtained from **Eq. (3.6)** are employed to determine the properties of damage:

$$\Delta u_j = \left| u_{dj} - u_{ij} \right| \tag{3.5}$$

$$DBI_j = max\left[0, \frac{\Delta u_j - mean(\Delta u_j)}{std(\Delta u_j)}\right] \quad (3.6)$$

where $u_{dj}$ *(j=1~n+1)* and $u_{ij}$ *(j=1~n+1)* stand for nodal displacements in the deteriorated and the normal girders, respectively. In addition, $mean(\Delta u_j)$ and $std(\Delta u_j)$ illustrate the mean and the standard deviation of $\Delta u_j$, in that order. The factor $DBI_j$ evaluates the point-relation degree at the $j^{th}$ point between the two girders. Particularly, $DBI = 0$ indicates that the structure is undamaged at the observation location, whereas DBI reaches the highest value at the damage location.

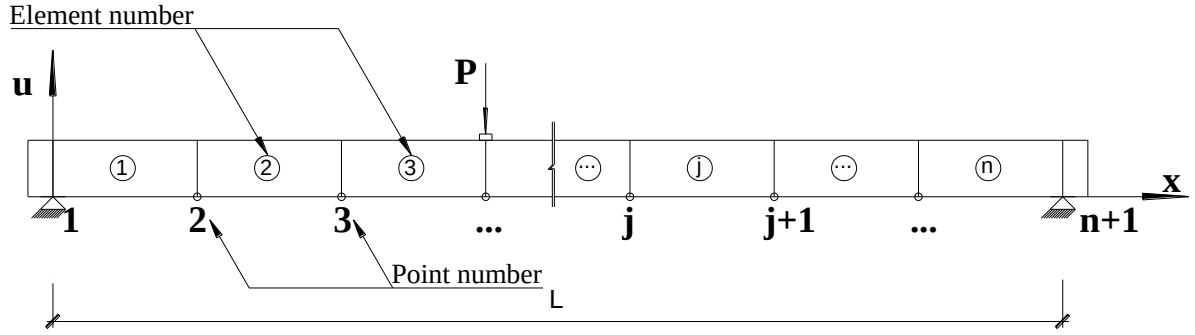


*Figure 3.1 Girder's segments and measuring positions*

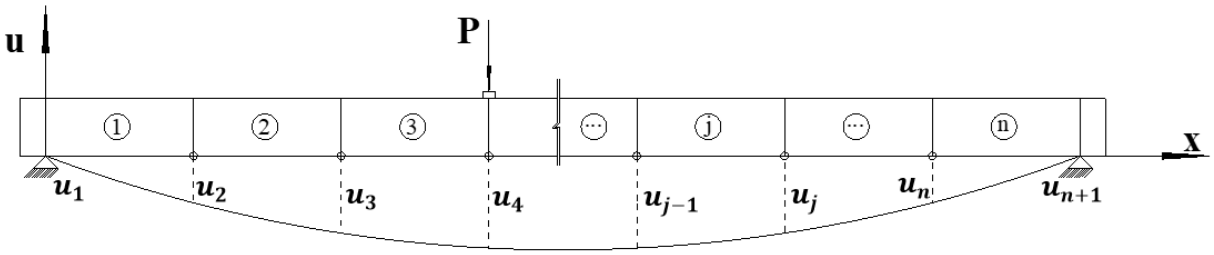


*Figure 3.2 Displacement curve of the simply supported girder*

### 3.2 Displacement assurance criterion (DAC)

To assess the performance of the proposed index, a nonlinear finite-element model of a PC girder is produced. Moreover, three other linear examples are also employed to evaluate the sensitivity of the DAC index to damage detection.

#### 3.2.1 Nonlinear analysis of a PC girder

A 2D numerical model is produced in accordance with the specifications of a full-size JIS A5373-AS09 girder [27] by FX+ for DIANA, which is a commercially available program for nonlinear finite-element analysis. **Figure 3.3** presents an overview of the full-scale destructive

test setup performed on a PC girder with a span of L = 9200 mm. The PC girder is subjected to two concentrated loads in the middle of the span, and the distance between the two loading points is 1000 mm. The objective girder contains 16 PC steel strands (12φ7 mm). Each strand has D10-type stirrups arranged around it. The analysis model is shown in **Fig. 3.4**. In particular, the PC strands and stirrups are modeled as the bar in plain stress type. The bonding force between the concrete and bars is assumed as complete. The thickness of the concrete element is represented by simplifying the haunches. The rotating total strain crack model for the concrete [28], which includes the JSCE tension softening model for tensile behavior and the multi-linear model for compressive behavior, was employed here. All parameters for the rotating strain crack model are presented in **Table 3.1**. The fracture energy of concrete is the energy consumed to form cracks per unit area, and is calculated by the following equation [29].

$$G_f = 10(d_{max})^{1/3} {f'_{ck}}^{1/3} \tag{3.7}$$

where, the values of $G_f$, $d_{max}$ and $f'_{ck}$ are related to the fracture energy (N/m), the maximum aggregate size (mm), and the compressive strength of concrete (N/mm$^2$), respectively. In the present study, the value of $d_{max}$ is assumed as 20 mm. Also, owing to the absence of experimental data, the estimation of the tensile strength of concrete $f_{tk}$ can be done by **Eq. (3.8)** based on the characteristic compressive strength $f'_{ck}$ [29].

$$f_{tk} = 0.23 {f'_{ck}}^{2/3} \tag{3.8}$$

where, the unit of strength is N/mm$^2$.

Moreover, the stirrups are assumed as in the linear elastic material model with a Young's modulus $E_s = 210000\ N/mm^2$, and Poisson ratio $\nu = 0.15$. Also, the PC steel strands are defined by the property "PCbar" made of steel with a Young's modulus $E_s = 210000\ N/mm^2$ and a Von Mises yield stress $\sigma_y = 1580\ N/mm^2$.

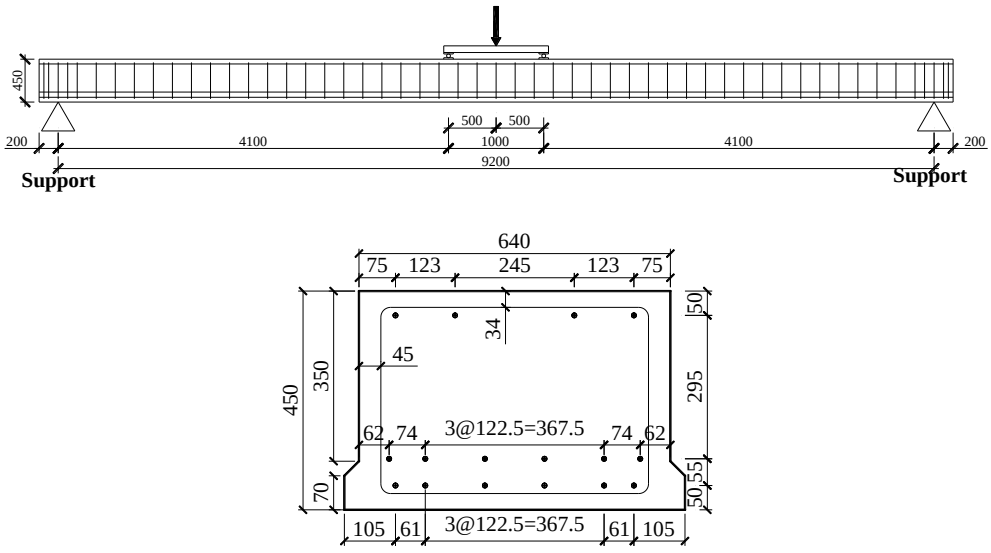


*Figure 3.3 Shape and size of PC girder*

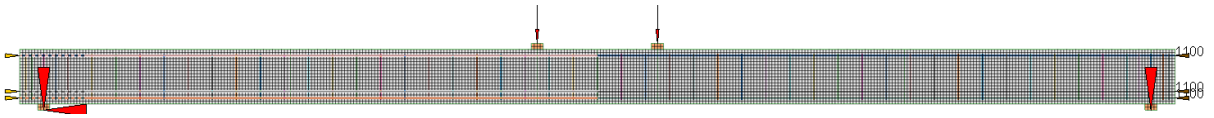

*Figure 3.4 Analysis model*

*Table 3.1 Material parameters for total strain crack model*

| | | | |
|---|---|---|---|
| Young's modulus | $E_c$ | 33000 | $N/mm^2$ |
| Poisson's ratio | ν | 0.15 | |
| Tensile strength | $f_{tk}$ | 3.53 | $N/mm^2$ |
| Fracture energy | $G_f$ | 0.1063 | N/mm |
| Compressive strength | $f'_{ck}$ | 60 | $N/mm^2$ |

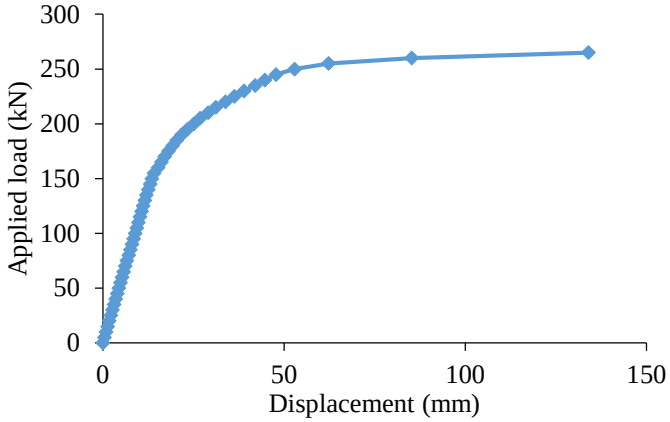


*Figure 3.5 Relationship between load and displacement*

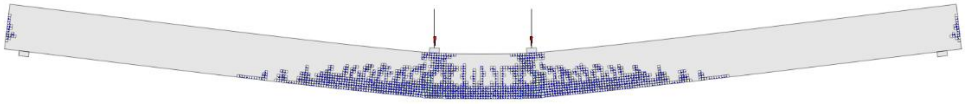

*Figure 3.6 Crack pattern at maximum loading*

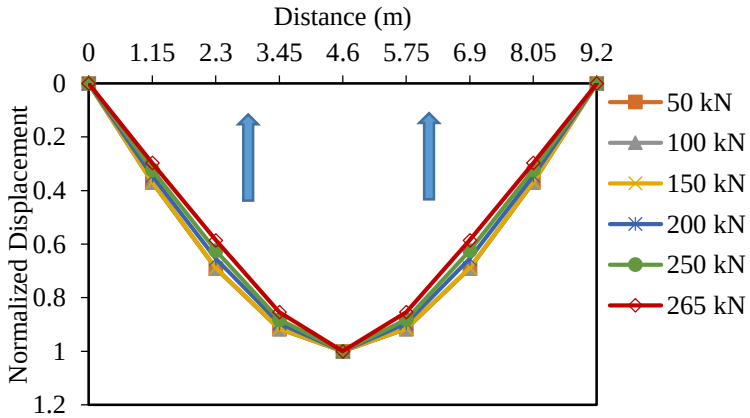


*Figure 3.7 Normalized displacement at some load cases*

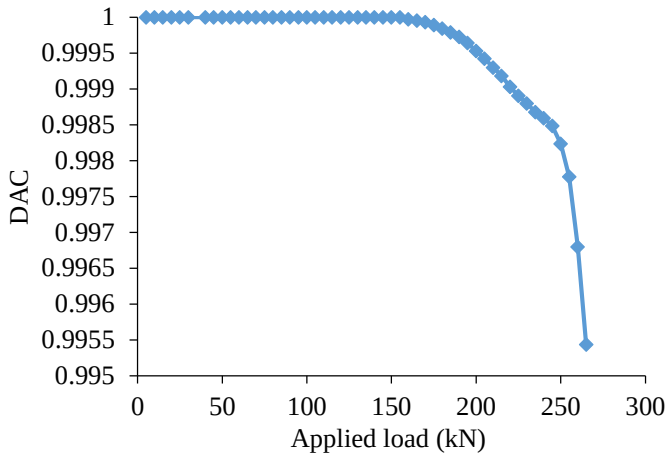


*Figure 3.8 Decrease of DAC with the increasing of applied load*

The load–displacement relationship is presented in **Fig. 3.5**. Cracks occurred when the displacement at the center of the span reaches approximately 11 mm with a corresponding load of up to 130 kN. After that, the displacement increases moderately, and the load is later terminated when the displacement at the span center exceeds 134 mm. Finally, the model collapses on the compression side and the crack pattern at maximum loading is shown in **Fig. 3.6**. During the test, the displacement is computed at every finite-element node for both the intact (elastic state) and the damaged state. It is assumed that the cause leading to changes in static properties is the growth of deterioration. In this study, the simple index named as DAC is considered to track the variation in the measured displacement owing to the presence of damage. The displacement at each finite-element node is extracted from analysis results and normalized with the largest one, at each loading step. Then, the normalized displacement curve of some of the nominated load cases can be estimated and represented in **Fig. 3.7**. In this figure, a decrease in the magnitude of the normalized displacement curve can be observed. In other words, the normalized displacement curve shows clearly a narrow tendency, in agreement with the increase in applied load. For determining DAC indices, the normalized displacement curve of the numerical model when it undergoes an applied load of 5 kN is regarded as the reference curve. If the two curves are identical, the DAC value would be equivalent to the unity, and any degradation in structural performance would produce a DAC value less than the unity. DAC values can be obtained by **Eq. (3.2)** using the normalized displacement for each segment. The variation in DAC under various load cases is depicted in **Fig. 3.8**. As shown in **Fig. 3.8**, DAC values are equal to the unity if the structure itself behaves linearly elastic. After the elastic limit is reached, DAC value performs decreased amplitude associated with the increased load and the development of cracks. Since the normalized displacement curves estimated when the model behaves in a wholly elastic manner are identical, one of these curves can be considered as the reference curve for tracking the degradations in structural performance. Despite its

relatively small range of variation, the DAC value is lower when the applied load increases and cracks occur in the structure. Consequently, it is clear that there is a correlation between changes in DAC and the occurrence of damage. In terms of this destructive test, the variation with temperature is negligible.

### 3.2.2 Sensitivity of DAC in damage detection

The relation between the variations in DAC with structural degradation has been proven in the previous section. In this part, three simulated damage scenarios are analyzed to clarify the sensitivity of the factor DAC in detecting the existence of deterioration. **Table 3.2** explains the characteristics of the three scenarios. Specifically, the scenarios of damage (Scenarios D1–D3) denote a single damage with different sizes and severities. Moreover, in this study, the increase in damage at each observed section is presumed to be associated with a decrease in the Young's modulus. Therefore, three numerical models are produced by FX+ for DIANA for the structural linear static analysis, as shown in **Fig. 3.9(a)–(c)**. In these figures, the blue areas illustrate the damage. In terms of this assessment, the same loads are employed for all cases.

*Table 3.2 Damage characteristics of the objective model*

| Scenarios of damage | Area of damage location | Percentage reduction in the Young's modulus | Number of damage locations |
|---|---|---|---|
| | $cm^2$ | % | |
| Scenarios 1 (D1) | 575 | 10,20,30,40,50,60,70 | 1 (0,125L-0.25L) |
| Scenarios 2 (D2) | 2300 | 10,20,30,40,50,60,70 | 1 (0,125L-0.25L) |
| Scenarios 3 (D3) | 4600 | 10,20,30,40,50,60,70 | 1 (0,125L-0.25L) |

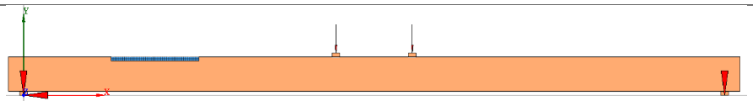

(a) Scenarios 1 (D1)

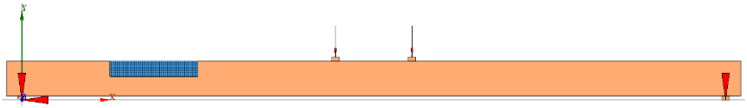

(b) Scenarios 2 (D2)

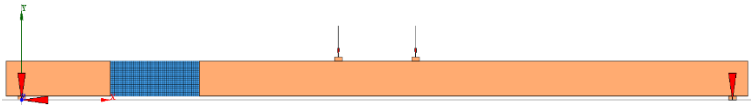

(c) Scenarios 3 (D3)

*Figure 3.9 Three scenarios of damage.*

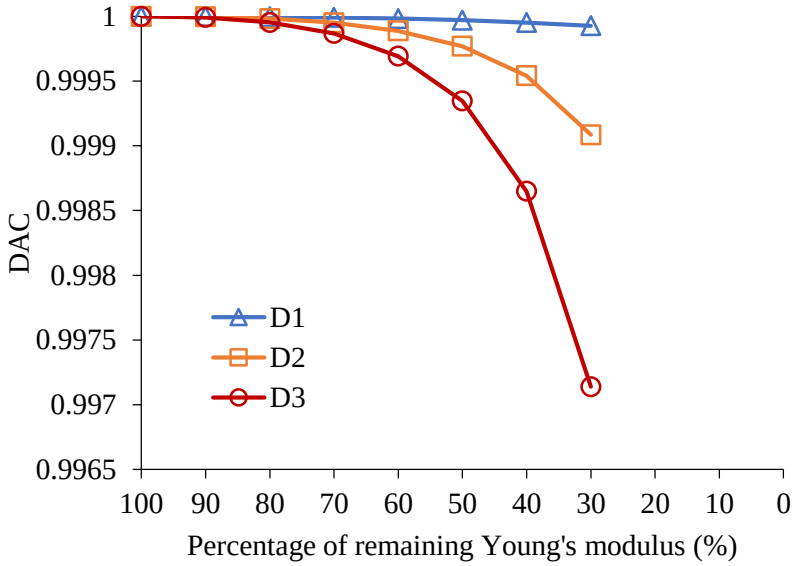


*Figure 3.10 Sensitive of DAC on the damage detection*

To identify the changes in structural responses caused by the presence of damage, the deflections of some points marked under the target girder are obtained to estimate the DAC factor. The effect of stiffness loss on DAC values in the three damage scenarios is presented in **Fig. 3.10**. According to **Fig. 3.10**, the increase in percentage reduction of the Young's modulus generates DAC values lower than the unity in all cases. Moreover, DAC values in Scenarios D1 and D2 are higher than in Scenario D3, and the deviations increase significantly when the modification of the Young's modulus reaches 70%. These results demonstrate the theoretical standpoint that there is a relation between damage severity and changes in nodal displacement, represented in this study as the factor DAC. Furthermore, it also shows that DAC has the capability to identify the occurrence of damage even in the small damage case of D1.

### 3.2.3 Effect of number of measurements upon DAC coefficient

A critical parameter in utilizing the variation in DAC for damage detection is the number of measurement points. As mentioned in the former section, DAC illustrates the relationship between two displacement curves at different states of structure. Consequently, it is assumed that the more points are measured, the more accurately the curve and DAC coefficient can be determined. Due to the economic situation and limitations of facilities, the number of measurement points is not always abundance for actual experiments. Therefore, the effect of limited measurement points on DAC should be investigated thoroughly. In this study, eight different measuring systems are used for the same modeling girder. The nodal displacements are taken at evenly distributed points under the girder. The first case (coarse) consists of three

observation points over the length of the girder (the distance between each point is equal to 0.25L), as shown in **Fig. 3.11(a)**. The other seven cases including 5, 7, 9, 15, 19, 29, and 31 measurements (the last is the fine case) are shown in **Fig. 3.11(b)–(h)**, respectively. For seven-point, 15-point, and 31-point measuring cases, the distances between two observed points were selected as L/8, L/16, and L/32, respectively. In this study, the approach, which measures the nodal displacement at 31 points under the girder, is supposed to give the best fit to the deflection curve of the girder as compared to the other considered number of measurements. Therefore, the DAC value of the 31-point system is taken as the target DAC factor. **Figure 3.12** shows the effect of the number of observation points upon the DAC value. According to **Fig. 3.12**, all the deviations vary under 0.0009%, which is a relatively low rate. This result implies that the number of measurements does not perform a significant role in the variation in DAC when the number of points is more than seven. Moreover, it is also important to mention that the DAC coefficients obtained from the measurement system using seven points are nearly identical to those obtained using 9, 15, 19, 29, and 31 points, because the estimated deviations are equal to or less than 0.0001%. Accordingly, when considering the efficiency and economy of the utilization of the DAC coefficient for identifying the occurrence of structural damage, the seven-point measurement system can provide relatively reasonable results.

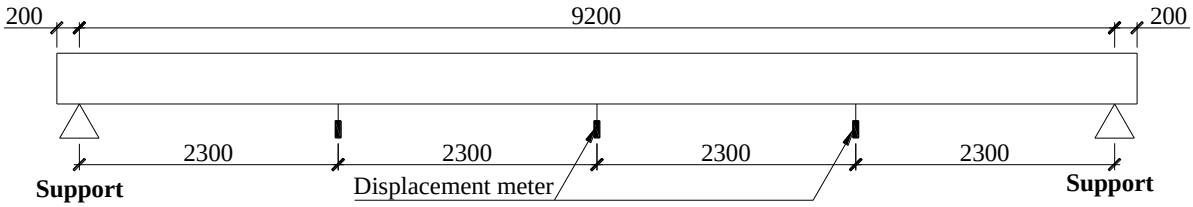


(a) 3-point measurement system

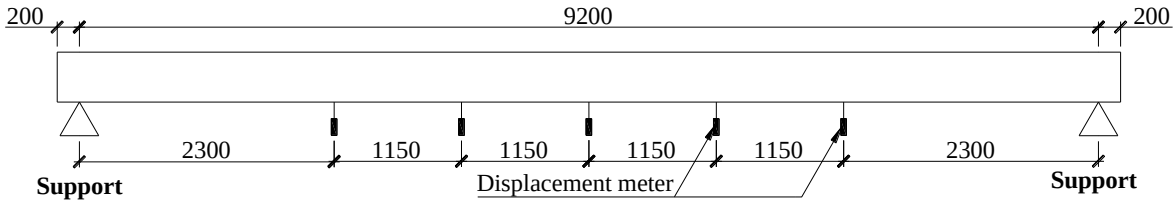


(b) 5-point measurement system

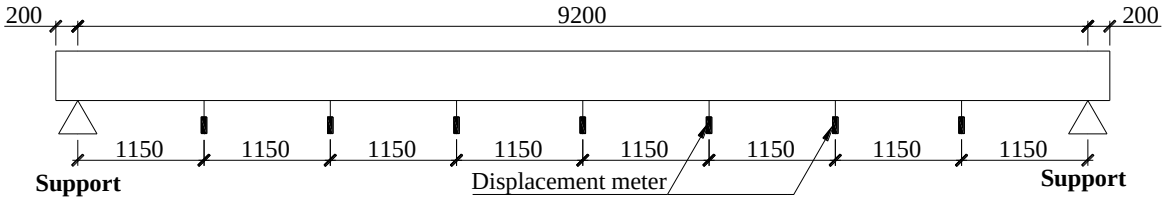


(c) 7-point measurement system

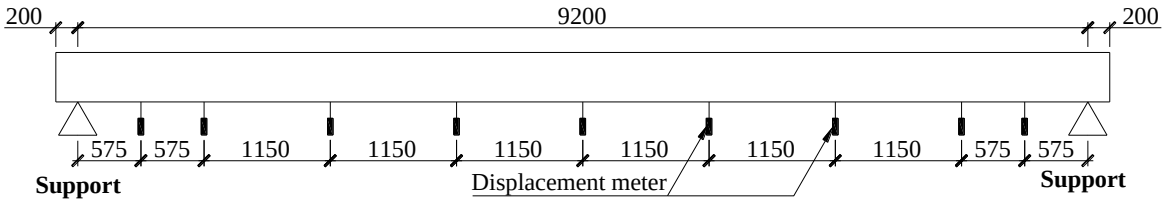


(d) 9-point measurement system

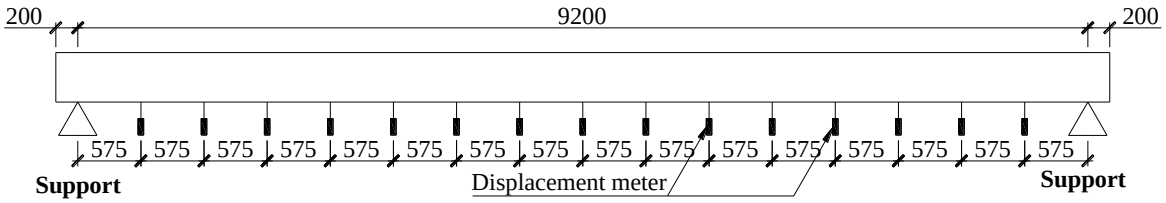


(e) 15-point measurement system

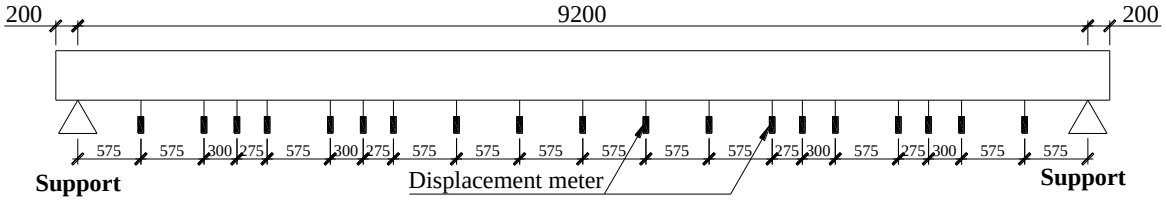


(f) 19-point measurement system

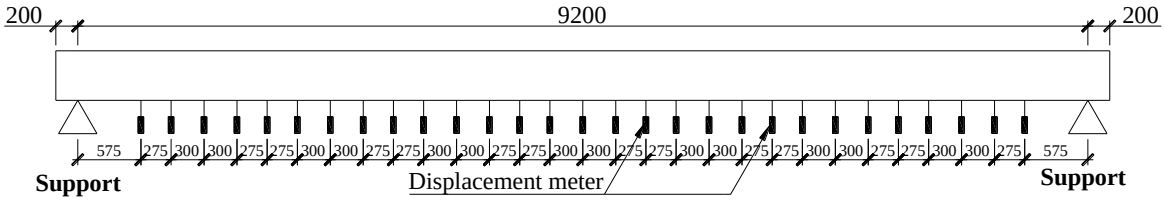


(g) 29-point measurement system

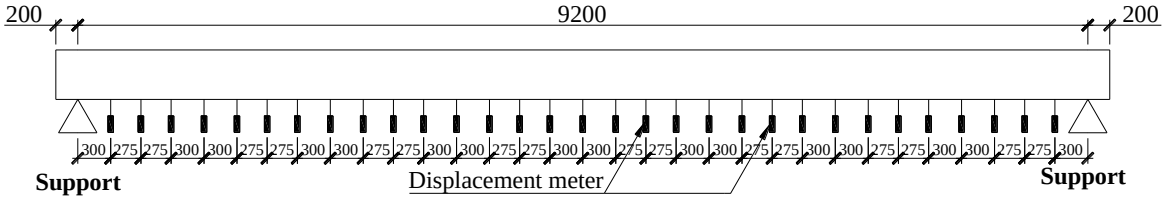


(h) 31-point measurement system

*Figure 3.11 Eight measuring cases (Unit: mm)*

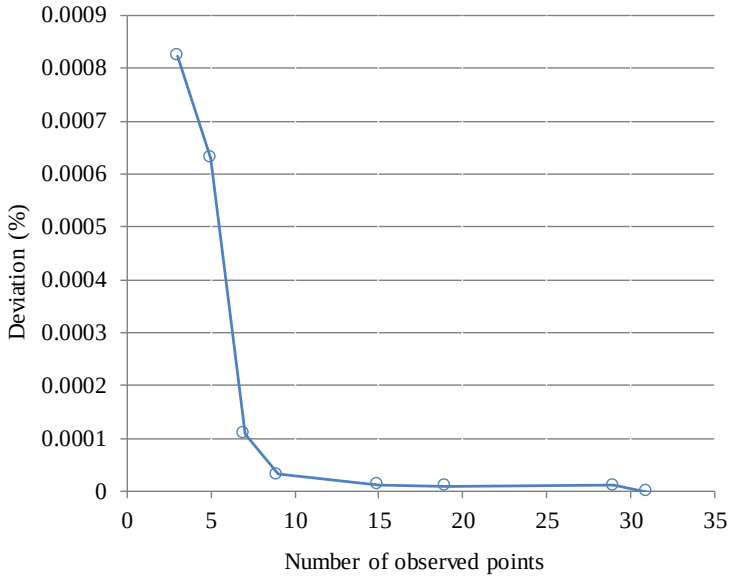


*Figure 3.12 Effect of the number of measurements upon DAC coefficient*

## 3.3 Displacement-based index (DBI)

For clarifying the feasibility of structural damage localization using the DBI approach, obtained from static responses, two numerical models are considered in this study. In particular, a simply supported PC girder (statically determinate structure) and a two-span continuous girder (statically indeterminate structure) are utilized as examples. Various parameters, which might influence the performance of the proposed method, are also analyzed and discussed. The damage considered in this study is assumed to only affect the stiffness, which is modeled by a decline in the Young's modulus at the location of damage.

### 3.3.1 Example 1: a simply supported PC girder (statically determinate structure)

#### (1) Overview of the example

As a statically determinate structure, the structure chosen for the first study is the same as the model analyzed in **Sect. 3.2.1**. **Figure 3.4** shows a 2D model of the objective PC girder with a span of L = 9200 mm which is supported at two points. The material parameters also remain the same as in the previous model. As shown in **Table 3.3** and **Fig. 3.13**, ten different damage scenarios are considered for evaluating the DBI factor. The first three scenarios (Scenarios 1–3) are taken into account for identifying single and double damages near the supports. The fourth and fifth scenarios are employed to study the competence of DBI in recognizing damage with different locations using the same loading case.

*Table 3.3 Damage characteristics of the simply supported model*

| Scenario of damage | Damage location x | Percentage reduction in the Young's modulus | Area of damage location | Load case | Number of measures |
|---|---|---|---|---|---|
| | mm | % | $cm^2$ | | |
| Scenario 1 | 100 | 10 | 200 | Case-1 | 9 |
| Scenario 2 | 100 | 10 | 200 | Case-1 | 92 |
| Scenario 3 | 100, 9100 | 10, 10 | 200, 200 | Case-1 | 92 |
| Scenario 4 | 4600 | 10 | 400 | Case-2 | 9 |
| Scenario 5 | 1150 | 10 | 400 | Case-2 | 9 |
| Scenario 6 | 1150 | 10 | 400 | Case-3 | 9 |
| Scenario 7 | 1150 | 10 | 400 | Case-4 | 9 |
| Scenario 8 | 2300 | 10 | 400 | Case-5 | 9 |
| Scenario 9 | 2300 | 10 | 400 | Case-1 | 9 |
| Scenario 10 | 2300 | 25 | 400 | Case-1 | 9 |

To analyze the influences of different types and intensities of load, five loading cases are considered in this example. Therefore, the fifth, sixth, and seventh scenarios are studied for applying the DBI on single damage detection using different load cases. Specifically, the first case of loading (Case 1) is a concentrated load, P = 10 kN at mid-span. The second instance of loading (Case 2) consists of two concentrated loads in the middle of the span and the distance between the two loading points is 1000 mm. For considering the effect of loading position, the third case of loading (Case 3) is similar to Case 1, but the load is located at the 3/4L position. The fourth case of loading (Case 4) is a uniformly distributed load with an intensity of q = 10 N/mm over the girder length. In addition, the influence of the load value on damage localization is also considered with the eighth and ninth scenarios. Accordingly, the fifth loading case (Case 5) is comparable to the first instance, but the intensity of force is decreased by two times.

Moreover, this paper attempts to study on the correlation of DBI with the severity of damage. For this reason, the damage of the ninth and tenth scenarios is assumed to occur at the same location, whereas their severities are different. In addition, the increase in degradation at each observation section is presumed to be related to the decrease in the Young's modulus. Specifically, the damaged element of the ninth scenario undergoes a reduction of 10% in the Young's modulus, while it is reduced by 25% in the tenth scenario.

One of the critical parameters when using changes in displacement for estimating the location of damage is the number of measurement points. Therefore, it is essential to evaluate the effect

of sufficient measurement points upon the sensitiveness of the DBI approach. In this study, a mesh size of 25 mm is assigned to all cases, and two different measurement systems are utilized for the model. The first instance (coarse) consists of nine observed points over the length of the girder (the distance between each point is equal to L/8 = 1150 mm), and the fine case includes 92 measures (the distance between each point is equivalent to 100 mm).

For calculating the index DBI given in **Eq. (3.6)**, the displacements of measurement points are obtained by the linear static analysis of FX+ for DIANA for both the intact model and the deteriorated one, which contains hypothetical damage in arbitrary segments. Then, the DBI value at each observed point is estimated using **Eqs. (3.5) and (3.6)** for each damage scenario. Finally, the DBI values are plotted to illustrate the damage locations.

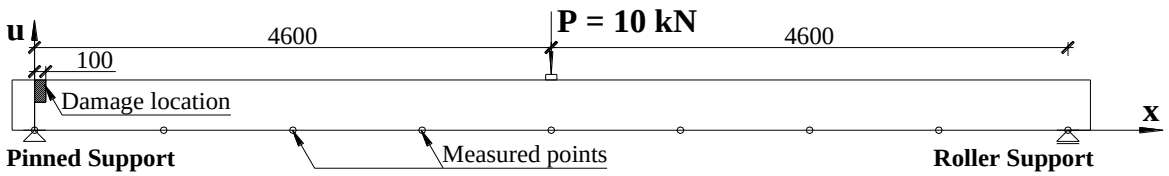


(a) Scenario 1

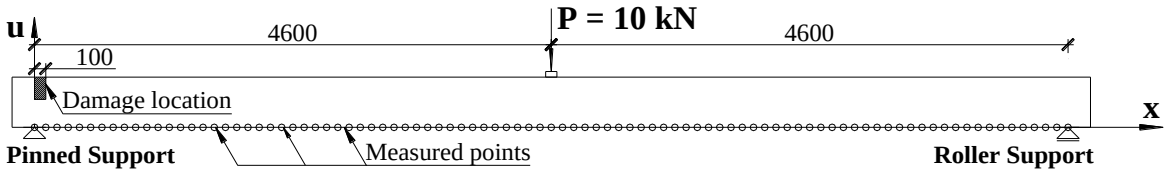


(b) Scenario 2

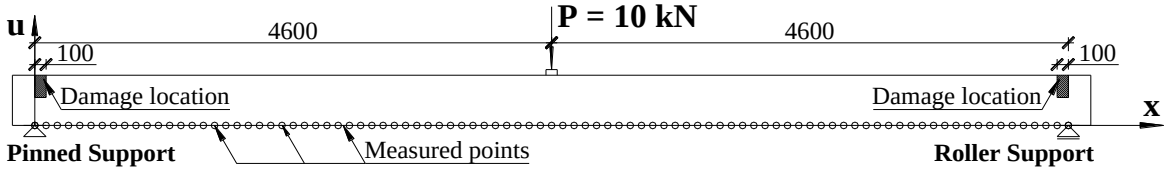


(c) Scenario 3

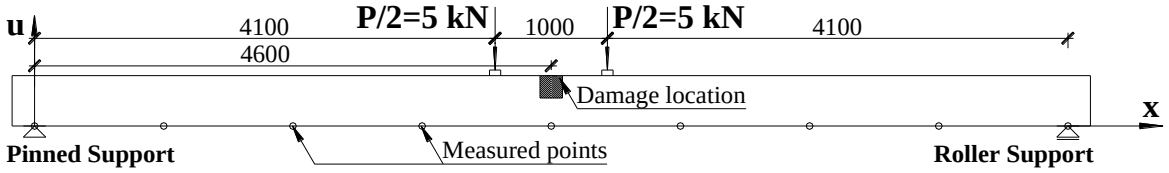


(d) Scenario 4

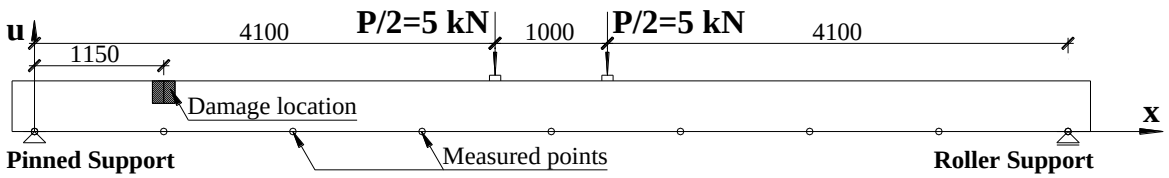


(e) Scenario 5

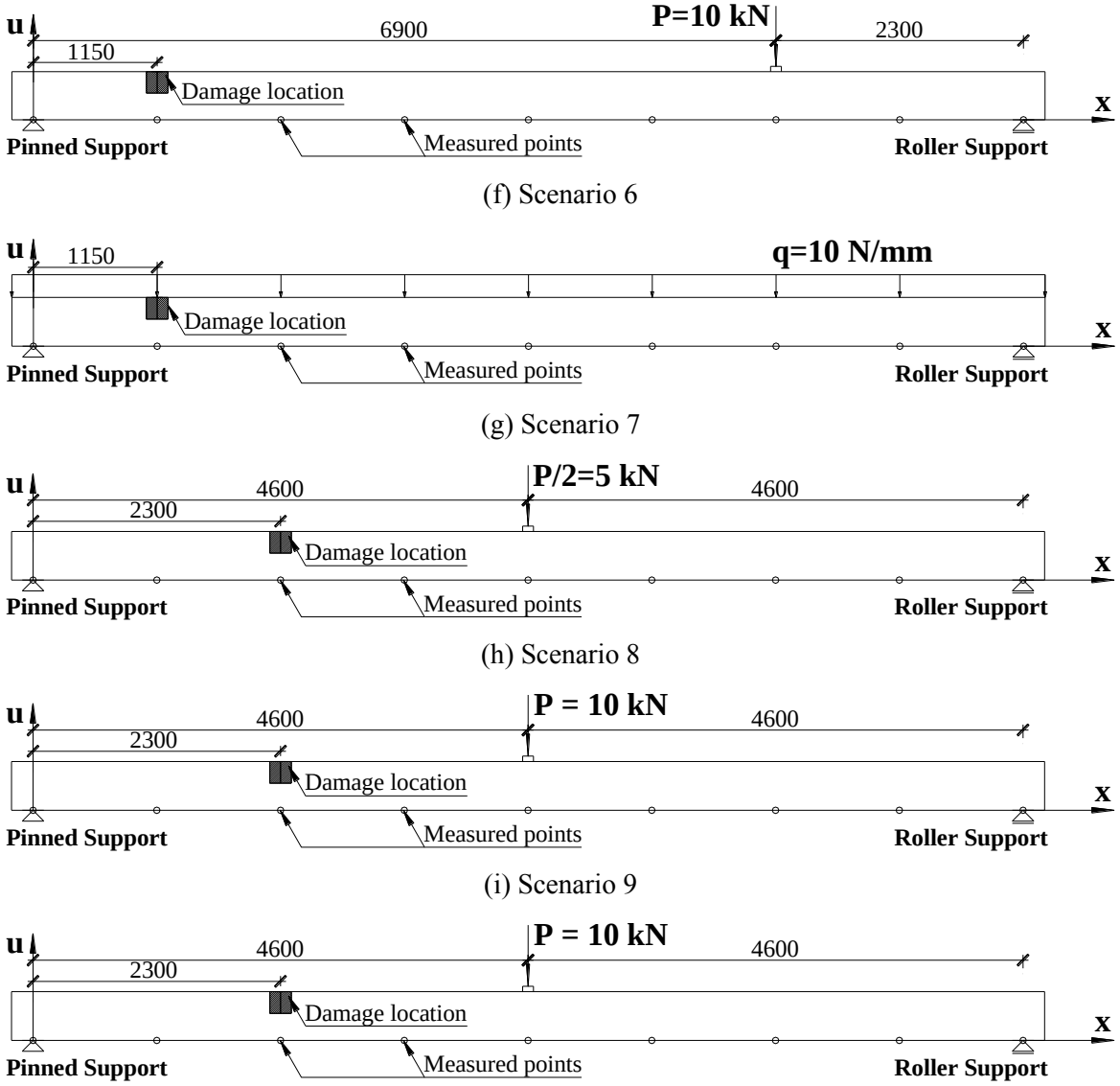


(f) Scenario 6




(g) Scenario 7




(h) Scenario 8




(i) Scenario 9




(j) Scenario 10

*Figure 3.13 Ten different damage scenarios for the simply supported girder (unit: mm).*

**(2) Results and discussion**

*Number of measurements*

Damage localization charts for ten different damage scenarios of the simply supported girder are illustrated in **Fig. 3.14(a)–(j)**. From these figures, the DBI value increases gradually and develop peaks at some positions, indicating the locations of the simulated damage. Scenarios 1 and 2 represent similar damage near the supports of the actual model under the loading Case 1. However, two different measuring situations, i.e., 9 and 92 measures, are, respectively, employed for Scenarios 1 and 2. As outcome of the calculation process, the DBI values of Scenarios 1 and 2 are plotted in **Fig. 3.14(a) and (b)**. These results reveal that the location of

damage is accurately identified in Scenario 2, whereas DBI performs a relative localization in Scenario 1. Another outcome, which is shown in **Fig. 3.14(c)** for Scenario 3 of damage, presents two peaks at the damage locations near both ends. Therefore, because all the simulated damage with different properties can be accurately located, for single and multiple damages, DBI can be proposed as a useful damage localization method. Nevertheless, it is important to note that limitations on measurement data play a significant role in the accuracy of the proposed method, as a sufficient number of points provides more accurate results than with a rough measurement case. For preventing uncertainties in the results, it is recommended that the number of measures should be as fine as possible. Moreover, the distance between the observation points and damage locations is another vital factor for a precise estimation.

*Case of loading*

The values of DBI for the damage Scenarios 4–7 subjected to different loading cases are plotted in **Fig. 3.14(d)–(g)**, respectively. By forming peaks at some observation locations, the DBI values correctly point out the simulated stiffness losses in all damage scenarios. All the damages in the Scenarios 4–5, which have different positions with the same severity, can be predicted by utilizing the Case 2 of loading alone. Furthermore, Scenarios 6–8 are considered for evaluating the flexibility of the approach for single damage detection using different loading cases. Specifically, a stiffness loss at x = 1150 mm is assumed in the girder, and the DBI values are obtained by alternately applying three different loading cases, which are a concentrated load at x = 6900 mm, two concentrated loads in the middle of the span, and a uniformly distributed load all over the girder length. The results show that the DBI charts are identical in all three cases, and the damage can be accurately located. Therefore, DBI shows a good performance in damage localization under all five loading cases employed in this study.

*Intensity of loading*

For assessing the influence of the load value on the amplitude of DBI, the results of Scenarios 8 and 9 concerning the same damage characteristics are examined with loading Cases 1 and 5, respectively. The corresponding DBI charts are shown in **Fig. 3.14(h) and 3.14(i)**. According to these figures, the DBI values from Case 1 of loading are equal to those obtained by the loading Case 5 at all observation points, although the static responses for all measures in Scenario 8 are half of those obtained from Scenario 9. The explanation of this similarity is that there is a twofold increase in the values of both the numerator and the denominator of the DBI equation, leading to the same results for the fraction. Therefore, it is proposed that there is no correlation between the DBI values and the intensity of load when using DBI as a damage localization approach.

*Severity of damage*

In this section, the relation between the severity of damage with the amplitude of DBI is studied to assess the capability for quantifying the deterioration. **Figure 3.14(i) and 3.14(j)** shows DBI charts for the damage Scenarios 9 and 10, respectively, which represent a girder subjected to the same damage location but with different severities. It is found that the DBI values in Scenario 9 are similar to those obtained in Scenario 10. Therefore, as all damages in Scenarios 9 and 10 are accurately located, this result implies that DBI can pinpoint and localize damage, but it does not comprise information on the magnitude of damage.

*Measurement noise*

Unavoidable errors cannot be excluded in the fieldwork. Regarding the proposed method, it is necessary to analyze the effect of uncertainties. In this study, noise is incorporated into the precise measurements as an error term by adding a series of pseudorandom numbers to the theoretically calculated displacement. The pseudorandom numbers are obtained by the Excel RAND function to get a random number between –1 and 1. Then, the nodal displacements of the damaged model are randomly interfered with a uniformly distributed number by the following equation:

$$u_{dj}^{n} = u_{dj} \times \{1 + [2 \times RAND() - 1] \times k\} \tag{3.9}$$

where $u_{dj}$ stands for the nodal displacements of the damaged structure, $u_{dj}^{n}$ represents the noisy nodal displacements and RAND() is a function in Microsoft Excel [30] for getting a random number between 0 and 1. In addition, k stands for the percentage of simulated noise.
In the present study, the assumption is made that the nodal displacements of the damaged girder in Scenario 5 (S5) are polluted by a measurement noise with an error of 1, 0.2, and 0.1%. **Tables 3.4, 3.5, 3.6** present DBI values for Scenario 5 under loading Case 2 with an artificial measurement noise of 1, 0.2, and 0.1%, respectively. The results show that the DBI approach accurately points out the locations of stiffness loss when the pseudorandom noise is less than 0.1% with respect to the simply supported model. Therefore, it is possible to use the proposed method to detect and localize structural deterioration under the condition that the measurement displacement is obtained with high accuracy.

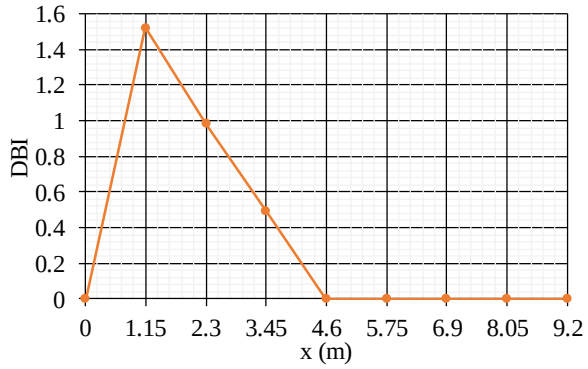


(a) Scenario 1

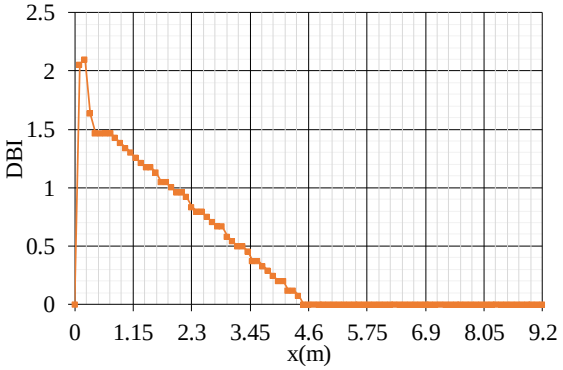


(b) Scenario 2

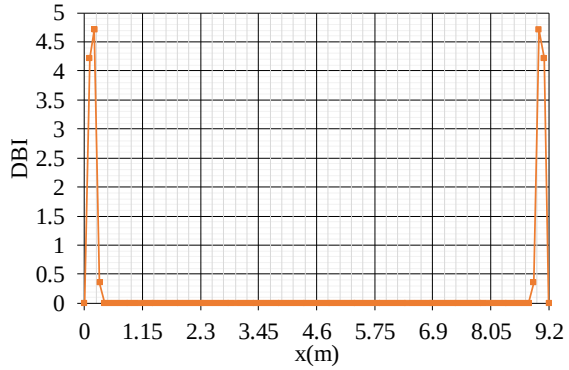


(c) Scenario 3

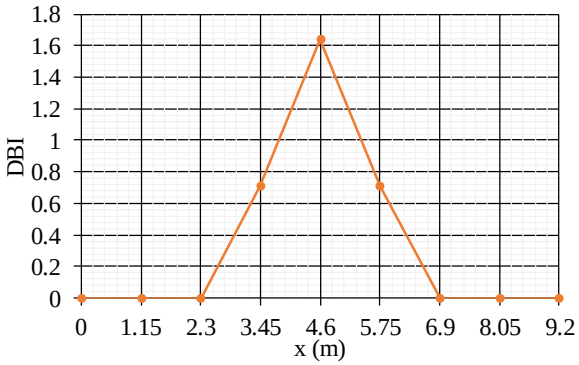


(d) Scenario 4

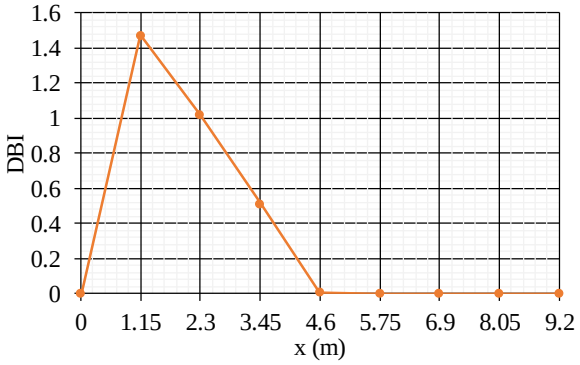


(e) Scenario 5

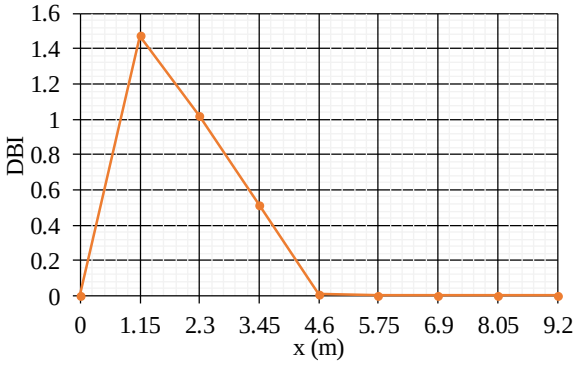


(f) Scenario 6

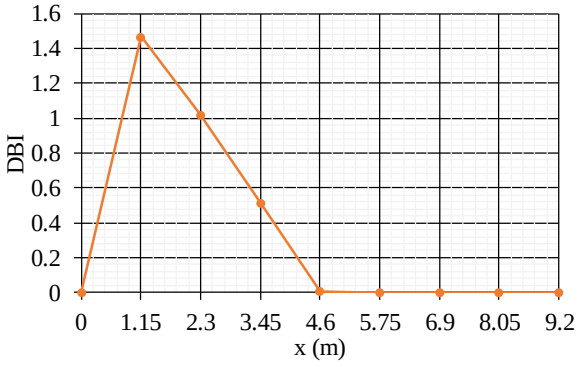


(g) Scenario 7

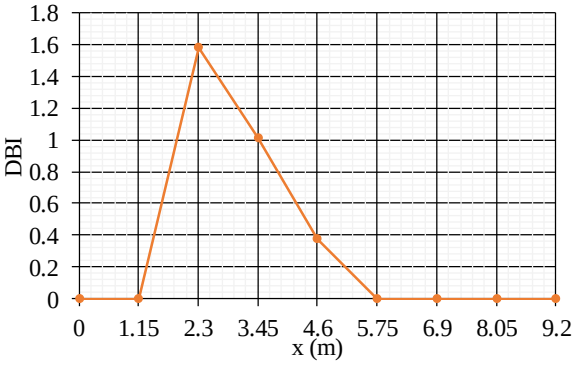


(h) Scenario 8

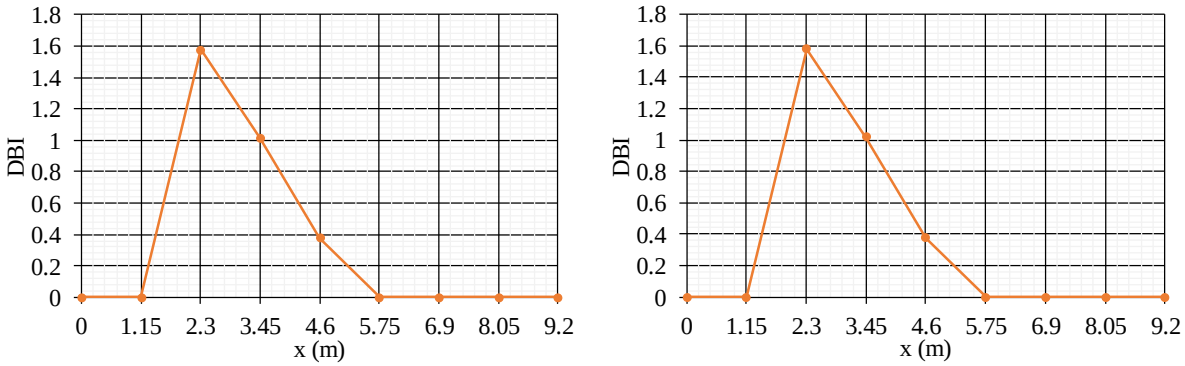


(i) Scenario 9 (j) Scenario 10

*Figure 3.14 Damage localization for ten different damage scenarios of the simply supported girder.*

*Table 3.4 DBI values for scenario 5 with 1% measurement noise*

| Case | DBI at positon x | | | | | | | | | Result | |
|---|---|---|---|---|---|---|---|---|---|---|---|
| | x1=0 | x2=L/8 | x3=2L/8 | x4=3L/8 | x5=4L/8 | x6=5L/8 | x7=6L/8 | x8=7L/8 | x9=L | with noise | noise-free |
| S5_x2 | 0 | 0 | 0 | 0.350 | 0.815 | 0.978 | 0.726 | 0 | 0 | x6 | x2 |
| S5_x3 | 0 | 0.090 | 1.839 | 0.890 | 0 | 0 | 0 | 0 | 0 | x3 | x3 |
| S5_x4 | 0 | 0 | 0.467 | 1.743 | 0.799 | 0 | 0 | 0 | 0 | x4 | x4 |
| S5_x5 | 0 | 0 | 0 | 0.670 | 1.742 | 0.670 | 0 | 0 | 0 | x5 | x5 |
| S5_x6 | 0 | 0 | 0 | 0 | 0.872 | 1.725 | 0.379 | 0 | 0 | x6 | x6 |
| S5_x7 | 0 | 0 | 0 | 0 | 0.025 | 0.890 | 1.839 | 0.090 | 0 | x7 | x7 |
| S5_x8 | 0 | 0.118 | 0.821 | 0.516 | 0 | 0 | 0 | 1.504 | 0 | x3; x8 | x8 |

*S5 represents the damage scenario 5 and xj (j=1~9) stands the assumed damage location of the noise-free case.*

*Table 3.5 DBI values for scenario 5 with 0.2% measurement noise*

| Case | DBI at positon x | | | | | | | | | Result | |
|---|---|---|---|---|---|---|---|---|---|---|---|
| | x1=0 | x2=L/8 | x3=2L/8 | x4=3L/8 | x5=4L/8 | x6=5L/8 | x7=6L/8 | x8=7L/8 | x9=L | with noise | noise-free |
| S5_x2 | 0 | 0.850 | 0.995 | 0.775 | 0.370 | 0 | 0 | 0 | 0 | x3 | x2 |
| S5_x3 | 0 | 0 | 1.519 | 1.037 | 0.441 | 0 | 0 | 0 | 0 | x3 | x3 |
| S5_x4 | 0 | 0 | 0.405 | 1.601 | 0.896 | 0.145 | 0 | 0 | 0 | x4 | x4 |
| S5_x5 | 0 | 0 | 0 | 0.719 | 1.613 | 0.719 | 0 | 0 | 0 | x5 | x5 |
| S5_x6 | 0 | 0 | 0 | 0.184 | 0.948 | 1.581 | 0.334 | 0 | 0 | x6 | x6 |
| S5_x7 | 0 | 0 | 0 | 0 | 0.441 | 1.037 | 1.519 | 0 | 0 | x7 | x7 |
| S5_x8 | 0 | 0 | 0 | 0 | 0.191 | 0.676 | 1.081 | 1.116 | 0 | x8 | x8 |

*S5 represents the damage scenario 5 and xj (j=1~9) stands the assumed damage location of the noise-free case.*

*Table 3.6 DBI values for scenario 5 with 0.1% measurement noise*

| Case | DBI at positon x | | | | | | | | | Result | |
|---|---|---|---|---|---|---|---|---|---|---|---|
| | x1=0 | x2=L/8 | x3=2L/8 | x4=3L/8 | x5=4L/8 | x6=5L/8 | x7=6L/8 | x8=7L/8 | x9=L | with noise | noise-free |
| S5_x2 | 0 | 1.701 | 0.986 | 0.368 | 0 | 0 | 0 | 0 | 0 | x2 | x2 |
| S5_x3 | 0 | 0 | 1.605 | 1.006 | 0.347 | 0 | 0 | 0 | 0 | x3 | x3 |
| S5_x4 | 0 | 0 | 0.424 | 1.645 | 0.871 | 0.082 | 0 | 0 | 0 | x4 | x4 |
| S5_x5 | 0 | 0 | 0 | 0.706 | 1.650 | 0.706 | 0 | 0 | 0 | x5 | x5 |
| S5_x6 | 0 | 0 | 0 | 0.125 | 0.929 | 1.625 | 0.348 | 0 | 0 | x6 | x6 |
| S5_x7 | 0 | 0 | 0 | 0 | 0.347 | 1.006 | 1.605 | 0 | 0 | x7 | x7 |
| S5_x8 | 0 | 0 | 0 | 0 | 0 | 0.500 | 1.074 | 1.475 | 0 | x8 | x8 |

*S5 represents the damage scenario 5 and xj (j=1~9) stands the assumed damage location of the noise-free case.*

### 3.3.2 Example 2: a two-span continuous girder (statically indeterminate structure)

#### (1) Overview of the example

As a statically indeterminate structure, the next structure considered for this analysis is a two-span continuous PC girder. The girder is supposed to have the same cross section and material features as the objective girder utilized in the previous examples, but it is supported by a hinged and two roller supports, as depicted in **Fig. 3.15**. In addition, the selected span length between supports is 4600 mm. To investigate the applicability of DBI in the indeterminate case, five different damage scenarios, which are indicated in **Table 3.7** and **Fig. 3.16(a)–(e)**, are studied. The first two scenarios of damage (Scenarios 1 and 2) are considered to evaluate the ability of DBI for recognizing single damage with different locations. Moreover, regarding multiple damage identification, the model utilized for three other scenarios of deterioration (Scenarios 3–5) is subjected to three loading cases, and consists of two damage instances in both portions. In particular, the first case of loading (Case 1) outlines a concentrated load (P = 10 kN) located in the pin-roller supported portion, whereas the second instance accounts for two concentrated loads (P = 10 kN) located in both parts of the continuous girder. Furthermore, a uniformly distributed load is taken into consideration as Case 3. As mentioned above, the correlations of DBI with the severity of damage and intensity of applied load, which were discussed in the previous parts, are not considered in this section. In addition, the damage in this analysis is assumed to be associated with the reduction of the Young's modulus at some areas of the target girder. Linear static analyses are performed to examine the effectiveness of the proposed method in damage detection. Then, the pre- and post-damage structural responses are obtained numerically using the software FX+ For DIANA. In this section, a mesh size of 25 mm is

assigned to all cases of analysis, and the results of 92 measuring points (the distance between each measurement is equivalent to 100 mm) are utilized. The DBI values are estimated by **Eq. (3.6)** for each scenario and are plotted to localize damage.

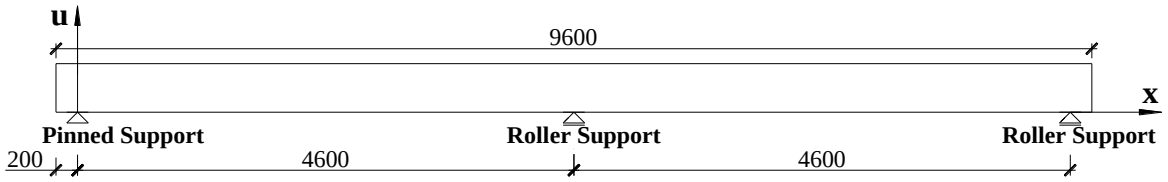


*Figure 3.15 Geometry of the two-span continuous girder*

*Table 3.7 Damage characteristics of the two-span continuous model*

| Scenario of damage | Damage location x | Percentage reduction in the Young's modulus | Area of damage location | Load case | Number of measures |
|---|---|---|---|---|---|
| | mm | % | $cm^2$ | | |
| Scenario 1 | 100 | 10 | 200 | Case-1 | 92 |
| Scenario 2 | 6900 | 10 | 200 | Case-1 | 92 |
| Scenario 3 | 1200,8000 | 10,10 | 200,200 | Case-1 | 92 |
| Scenario 4 | 1200,8000 | 10,10 | 200,200 | Case-2 | 92 |
| Scenario 5 | 1200,8000 | 10,10 | 200,200 | Case-3 | 92 |

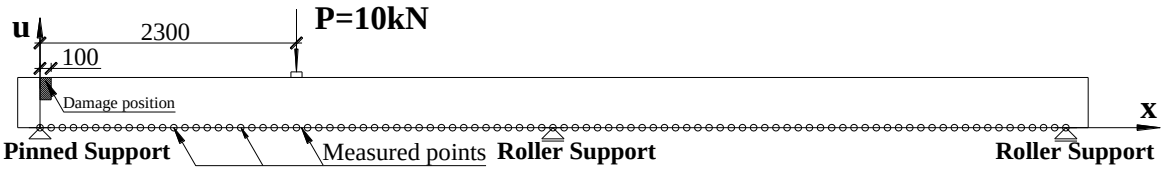


(a) Scenario 1

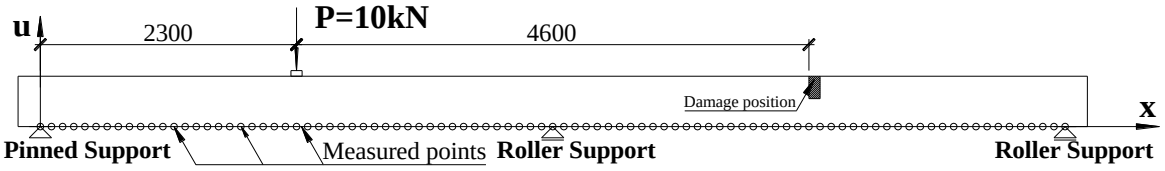


(b) Scenario 2

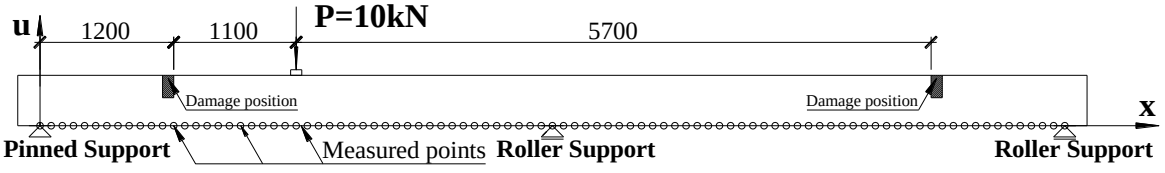


(c) Scenario 3

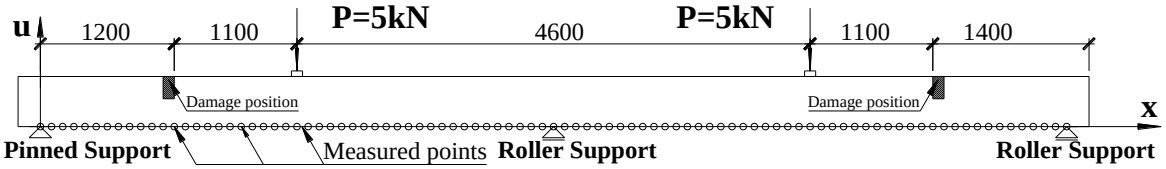


(d) Scenario 4

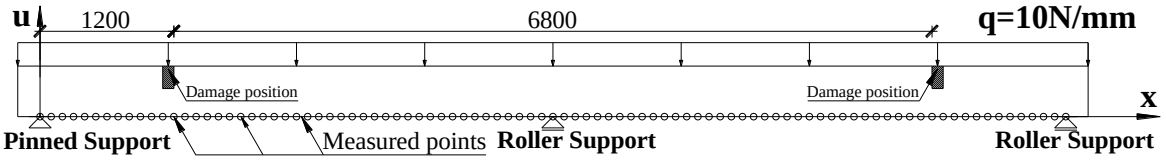


(e) Scenario 5

*Figure 3.16 Five different damage scenarios for the two-span continuous girder (unit: mm).*

**(2) Results and discussion**

*Applicability of proposed method*

As mentioned earlier, the first two scenarios of damage represent single damage with different locations, whereas Scenarios 3–5 are studied to show the capability of the proposed algorithm to pinpoint multiple damage using different cases of loading. The DBI values for the differences in nodal displacement between the intact and the deteriorated girder under five scenarios of damage are sketched in **Fig. 3.17(a)–(e)**. As can be seen in these figures, the DBI values develop considerable peaks at some positions of damage. In particular, Scenarios 1 and 2 show similar damage localized on the pin-roller supported and the roller–roller supported parts, respectively. The results described in **Fig. 3.17(a) and 3.17(b)** show that the damage can be localized even if the applied load is on a different portion. In regard to multiple damage identification, **Fig. 3.17(c)–(e)** presents the assessment results for dual damage scenarios (x = 1200 mm and x = 8000 mm) of the target girder subjected to loading Cases 1, 2, and 3, respectively. As can be seen in these figures, the DBI values at the deteriorated positions form significant peaks, while the values of the other elements remain unchanged as zero. The results show that the locations of damage, which are illustrated by the two peaks, are accurately identified in the three loading circumstances of this example. Because all damages are successfully recognized as significant peaks in these figures, it can be stated that the DBI approach can accurately locate different damage characteristics. Therefore, the applicability of the proposed method for damage detection is confirmed in the statically indeterminate case.

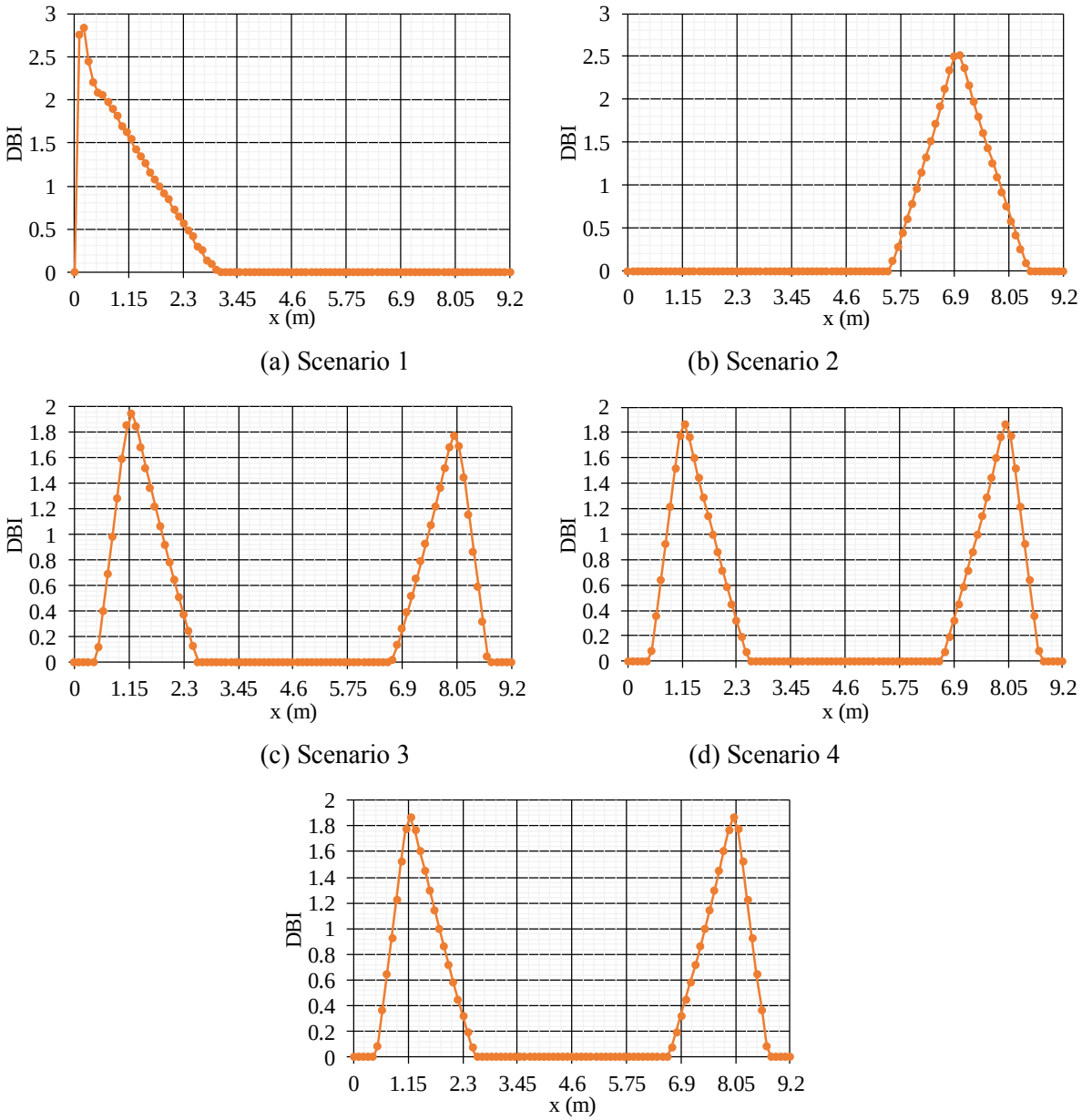


*Figure 3.17 Damage localization for five different damage scenarios of the two-span continuous girder.*

*Measurement noise*

The effects of measurement noise on the DBI method using variations in nodal displacements are also investigated for the two-span continuous case. **Figure 3.18(a)–(d)** plots the DBI values for the changes in nodal displacement interfered with a measurement noise of 0.2 and 0.1% for Scenario 2 (S2) and Scenario 5 (S5). As an outcome obtained from these figures, the DBI approach provides accurate answers only when the measurement noise is less than 0.1%.

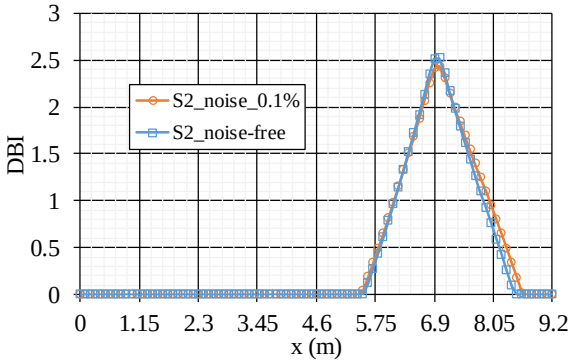


(a) Scenario 2 with 0.1% Noise

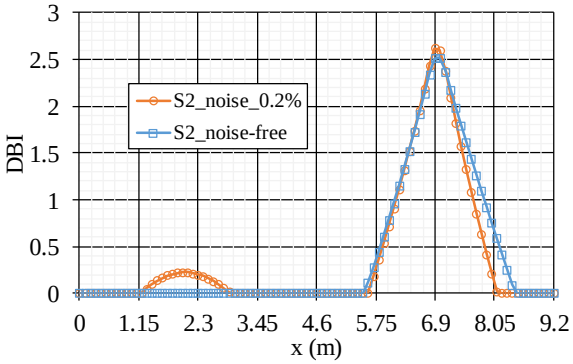


(b) Scenario 2 with 0.2% Noise

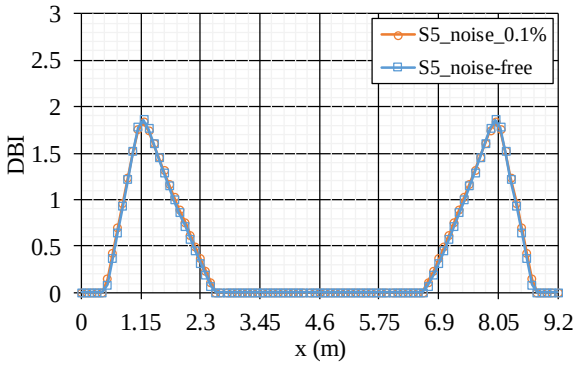


(c) Scenario 5 with 0.1% Noise

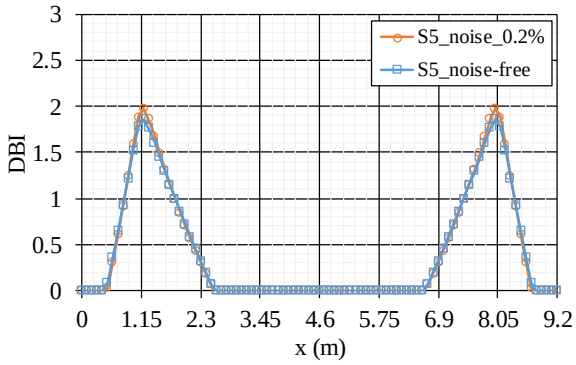


(d) Scenario 5 with 0.2% Noise

*Figure 3.18 Damage localization of scenario 2 and scenario 5 for two-span continuous girder with measurement noise.*

### 3.4 Conclusions

In this study, new damage indicators, called displacement assurance criterion (DAC) and displacement-based index (DBI), based on changes in the displacement of observation points, have been proposed and found as sensitive methods for damage detection in structures.

- ✓ The outcome of numerical studies reveals that, although its variation is relatively small, the DAC value decreases when the applied load increases and cracks occur in the structure. Therefore, there is a correlation between changes in DAC and damage state, and the decrease in DAC can indicate the occurrence of damage in structures.
- ✓ From the theoretical standpoint, the number of measurements does not play a major role in the change in DAC when there are more than seven observation points. It is also important to notice that the calculated DAC coefficient in the seven-measurement case is nearly identical to those obtained using more points, with estimated deviations under 0.0001%. Consequently, when considering the effectiveness and the economy of using the DAC coefficient to identify the occurrence of structural damage, the seven-point measuring system can provide relatively reasonable judgments.
- ✓ Another damage indicator, DBI is proposed as a suitable factor to identify damage locations, as the results of the numerical study reveal that all damages, with different characteristics and for two different static structures, can be accurately located. As another outcome worth mentioning, DBI shows a good performance for damage localization in all load cases utilized in this study.
- ✓ However, there is no correlation between the DBI values and the intensity of applied loads when using DBI as a damage localization approach.
- ✓ It is also important to note that limitations on measured static data play a significant role in the accuracy of DBI, and a sufficient number of points provides more accurate results than a rough measurement case. Moreover, the most critical factors for determining damage location are the selection of observed points at or near the damage locations, and the accuracy in measurements. For preventing uncertainty in the results, it is suggested that the number of measures should be as fine as possible.
- ✓ The DBI method is effective for damage detection only when the measurement noise is less than 0.1%. Therefore, the nodal displacement should be measured with high accuracy when using DBI for identifying structural deterioration.

The results in the present study are obtained purely from the numerical analyses, this work is a start point for a simple damage identification based on only displacement curve evaluation, and further research is needed on the subject. Regarding long-term prospects, further research should be carried out to apply DAC and DBI in actual situations, and future projects can target improvements in relation to dynamic strain and displacement influence lines.

### 3.5 References


[1] E. T. Lee and H. C. Eun, "Damage detection of damaged beam by constrained displacement curvature," *J. Mech. Sci. Technol.*, vol. 22, no. 6, pp. 1111–1120, 2008.

[2] A. Rytter, "Vibrational Based Inspection of Civil Engineering Structures," 1993.

[3] S. Hassiotis and G. D. Jeong, "Identification of Stiffness Reductions Using Natural Frequencies," *J. Eng. Mech.*, vol. 121, no. 10, pp. 1106–1113, 1995.

[4] Y. Xia, H. Hao, J. M. W. Brownjohn, and P. Q. Xia, "Damage identification of structures with uncertain frequency and mode shape data," *Earthq. Eng. Struct. Dyn.*, vol. 31, no. 5, pp. 1053–1066, 2002.

[5] Z. Y. Shi, S. S. Law, and L. M. Zhang, "Damage Localization by Directly Using Incomplete Mode Shapes," *J. Eng. Mech.*, vol. 126, no. 6, pp. 656–660, 2000.

[6] C. Y. Kao, X. Z. Chen, J. C. Jan, and S. L. Hung, "Locating damage to structures using incomplete measurements," *J. Civ. Struct. Heal. Monit.*, vol. 6, no. 5, pp. 817–838, 2016.

[7] A. K. Pandey, M. Biswas, and M. M. Samman, "Damage detection from changes in curvature mode shapes," *J. Sound Vib.*, vol. 145, no. 2, pp. 321–332, 1991.

[8] H. Zhong and M. Yang, "Damage detection for plate-like structures using generalized curvature mode shape method," *J. Civ. Struct. Heal. Monit.*, vol. 6, no. 1, pp. 141–152, 2016.

[9] T. Oshima, Y. Miyamori, S. Mikami, T. Yamazaki, S. Beskhyroun, and M. F. Kopacz, "Small damage detection of real steel bridge by using local excitation method," *J. Civ. Struct. Heal. Monit.*, vol. 3, no. 4, pp. 307–315, 2013.

[10] A. K. Pandey and M. Biswas, "Damage Detection in Structures Using Changes in Flexibility," *J. Sound Vib.*, vol. 169, no. 1, pp. 3–17, 1994.

[11] L. M. Z. Z. Y. Shi, S. S. Law, "Improved Damage Quantification from Elemental Modal Strain Energy Change," *J. Eng. Mech.*, vol. 128, no. 5, pp. 521–529, 2002.

[12] S. Das, P. Saha, and S. K. Patro, "Vibration-based damage detection techniques used for health monitoring of structures: a review," *J. Civ. Struct. Heal. Monit.*, vol. 6, no. 3, pp. 477–507, 2016.

[13] S. M. Seyedpoor, "Structural Damage Detection Using a Multi-Stage Particle Swarm Optimization," *Adv. Struct. Eng.*, vol. 14, no. 3, pp. 533–549, 2011.

[14] O. Huth, G. Feltrin, J. Maeck, N. Kilic, and M. Motavalli, "Damage Identification Using Modal Data: Experiences on a Prestressed Concrete Bridge," *J. Struct. Eng.*, vol. 131, no. 12, pp. 1898–1910, 2005.

[15] X. Wang, N. Hu, H. Fukunaga, and Z. H. Yao, "Structural damage identification using static test data and changes in frequencies," *Eng. Struct.*, vol. 23, no. 6, pp. 610–621, 2001.

[16] J.-W. Lee, K.-H. Choi, and Y.-C. Huh, "Damage detection method for large structures using static and dynamic strain data from distributed fiber optic sensor," *Int. J. Steel Struct.*, vol. 10, no. 1, pp. 91–97, Mar. 2010.

[17] Z. Sheena, A. Unger, and A. Zalmanovich, "Theoretical stiffness matrix correction by static test results," *Isr J Technol*, vol. 20, no. 6, pp. 245–253, 1982.

[18] M. Sanayei and O. Onipede, "Damage assessment of structures using static test data," *AIAA J.*, vol. 29, no. 7, pp. 1174–1179, 1991.

[19] M. R. Banan and K. D. Hjelmstad, "Parameter Estimation of Structures from Static Response. I. Computational Aspects," *J. Struct. Eng.*, vol. 120, no. 11, pp. 3243–3258, 1994.

[20] I. Y. Choi, J. S. Lee, E. Choi, and H. N. Cho, "Development of elastic damage load theorem for damage detection in a statically determinate beam," *Computers and Structures*, vol. 82, no. 29–30. pp. 2483–2492, 2004.

[21] X. Z. Chen, H. P. Zhu, and C. Y. Chen, "Structural damage identification using test static data based on grey system theory," *J. Zhejiang Univ. Sci.*, vol. 6A, pp. 790–796, 2005.

[22] F. Bakhtiari-Nejad, A. Rahai, and A. Esfandiari, "A structural damage detection method using static noisy data," *Eng. Struct.*, vol. 27, no. 12 SPEC. ISS., pp. 1784–1793, 2005.

[23] M. A.-B. Abdo, "Parametric study of using only static response in structural damage detection," *Eng. Struct.*, vol. 34, pp. 124–131, 2012.

[24] O. Yazdanpanah and S. Seyedpoor, "A crack localization method for beams via an efficient static data based indicator," *Comput. Methods Civ. Eng.*, vol. 4, no. 1, pp. 43–63, 2013.

[25] S. M. Seyedpoor and O. Yazdanpanah, "An efficient indicator for structural damage localization using the change of strain energy based on static noisy data," *Appl. Math. Model.*, vol. 38, no. 9–10, pp. 2661–2672, 2014.

[26] A. E. K. Jones and L. A. Clark, "The effects of ASR on the properties of concrete and the implications for assessment," *Eng. Struct.*, vol. 20, no. 9, pp. 785–791, 1998.

[27] Japanese Standards Association, *JIS A 5373:2016 Precast prestressed concrete products*. Tokyo, Japan, 2016.

[28] Tnodiana.com, "User's manual of FX+ for DIANA version 9.6." [Online]. Available: https://support.tnodiana.com/manuals/d96/Diana.html. [Accessed: 01-Jul-2016].

[29] Japan Society of Civil Engineers Concrete Committee, *Standard specifications for concrete structures: design code*. Concrete committee, 2012.

[30] Support.office.com, "RAND function for Microsoft Excel." .

# Chapter | 4

# Long-term Vibration Monitoring of the Effects of Temperature and Humidity on PC Girders with and without Fly Ash considering ASR Deterioration

## 4.1 Introduction

In the structural health monitoring of concrete bridges, it is important to assess the relationship between the structural performance and the state of damage to conduct maintenance. Hence, the responses of a structure, which are divided into static and dynamic responses, are vital.

Over the years, many studies have been performed on the application of dynamic responses and damage detection [1–7] in terms of the natural frequencies, mode shapes, modal curvature, and high-order mode shape derivative. A recent study demonstrated that natural frequencies, mode shapes, and damping ratios are invariant in structures [1]. Thus, the health of a structure is correlated to the changes in its modal parameters. The variations in these parameters do not depend on the location of the damage because of their global characteristics. Hence, the deterioration can be estimated using sensors mounted at any position on a structure. In particular, the changes in the natural frequency have been thoroughly investigated as identifiers of stiffness reduction [2]. In addition, the changes in the uncertain frequency, mode shape data [3], incomplete mode shape [4], mode shape curvatures [5], and flexibility matrix [6] were used to localize the damage. The variation in the elemental modal strain energy was applied to improve damage quantification [7]. Hence, most of the studies focused on using structural responses to identify the properties of damage (occurrence, location, and severity), whereas only a few studies discussed the effects of environmental conditions on the variations in the structural characteristics (dynamic and static responses). If the effects of these uncertainties on the structural properties are greater than or comparable to the effects of structural damage, the structural damage cannot be reliably identified [8]. Therefore, studying the environmental effects on the structural properties is important to effectively apply the monitoring methods to civil engineering structures.

During the past few decades, the correlations between the vibrational characteristics and temperature changes have attracted considerable interest in technical literature and have been

investigated using different approaches such as numerical analysis via finite element (FE) methods [9,10], laboratory tests [8,11], and monitoring approaches in civil structures [1,12,13].

*Theoretical derivation method*

Macdonald and Daniell [9] performed modal analyses under two different temperature conditions using an FE model of a cable-stayed bridge with a main span of 456 m. A uniform change of 5 ºC in the entire structure was considered under the first condition, whereas a temperature gradient of +10 ºC was assumed between the top of the deck and the rest of the structure under the second condition. With regard to the FE model, beam elements and four shell elements were used to model the longitudinal girders and reinforced concrete (RC) slab of the deck, respectively. The results showed that the natural frequencies of approximately one-third of the modes shifted by up to ± 0.2% under both the cases, whereas no clear variation was observed in the others. Xu and Wu [10] investigated the effects of uniform and non-uniform temperature fluctuations on the frequency and changes in the mode shape curvature of a cable-stayed concrete box girder bridge using three-dimensional FE analysis. Their results proved that the variation behaviors in the frequency and mode-shape curvature under the effect of a non-uniform change in the temperature were the same as that under the effect of a uniform change in the temperature. Moreover, the maximum variation ratio of the frequency was ~2% when the uniform temperature gradient increased by ~60 ºC. The effect of the temperature on the frequencies was significant in the vertical bending mode.

*Laboratory test approach*

With regard to the laboratory test approach, previous studies provided rational conclusions about the variations in the vibrational responses under different environmental conditions. Xia et al. [8] performed periodic vibration tests on a reinforced concrete slab for approximately two years. It was perceived that the frequencies of the first four modes had a strong negative correlation with the temperature, whereas the increases in the damping ratios with the increase in the temperature were insignificant, and no clear correlation of the mode shapes could be observed with respect to the temperature difference. In particular, the natural frequencies of the three bending modes decreased by 0.13–0.23% when the temperature increased by 1 ºC. However, the sensitivities of the torsional mode and bending rigidity to the temperature were different. Kim et al. [11] observed similar outcomes. They reported that the bending modes were more sensitive than the torsional modes. With regard to the lower modes, the effect of the temperature on the change in the natural frequency is relatively greater. Moreover, two levels of damage were inflicted on a girder near the center of the structure: the bottom flange was cut halfway in from the outside, and the bottom flange was cut completely in from either side. Consequently, the changes in the vibration properties due to the damage were largely similar to

those due to the temperature fluctuations.

*Trend analysis approach*

So far, only a few studies have monitored the changes in the structural responses of full-scale bridges considering environmental effects [1,12,13]. Cornwell et al. [12] reported that the first three natural frequencies of the Alamosa Canyon Bridge varied by approximately 4.7, 6.6, and 5.0% during a 24 h period as the temperature of the bridge deck changed by approximately 22 ºC. Later, with the support of the European SIMCES-project, Peeters and De Roeck [13] monitored the Z24 Bridge in Switzerland for one year. In particular, black-box models were developed from the healthy-bridge data to describe the variations in the eigenfrequencies due to the changing environmental conditions. The monitored data were then analyzed with the reference data, and the damage was recognized when an eigenfrequency varied beyond certain confidence intervals from the proposed model. In addition, the results of the monitored data show that the first four vibration frequencies varied by 14–18% during the ten months of analysis. The frequencies of all the modes analyzed, except the second mode, decreased with the increase in the temperature. In another study worth mentioning, Huth et al. [1] identified the damage using modal data for the Romeo Bridge in Switzerland. The results suggested that a criterion for the damage detection based on the mode shape area might perform better than that based on the variations in the natural frequencies. Furthermore, the obtained monitoring data showed that the effects of the environmental parameters were considerable, particularly that of the change in the temperature, on the natural frequencies.

Among the different laboratory approaches employed for evaluating the changes in the vibration properties with respect to the environmental conditions, simultaneous effects of structural degradation over the monitoring period on the observation data has not been explicitly reported. Ha et al. [14] showed that the natural frequency of the first bending mode decreased gradually until the destruction of the objective girder. Before the yielding load, the decreasing rate was estimated to be within ~6%. However, this rate clearly increased to approximately 31% when the natural frequencies measured before the test and at the final loading state were compared. Thus, there was a decrease in the natural frequency of the first bending mode in accordance with the increase in the structural degradation, i.e., cracks due to loading. With the aim of contributing to efficient structural health monitoring approaches, this study investigates the effects of environmental conditions on the vibrational properties of prestressed concrete (PC) girders, which were affected by varying degrees of deteriorations induced by an alkali–silica reaction (ASR), as introduced in Chapter 2. Because the environmental conditions induce complicated uncertainties in the structural responses, this study only examines the variations in the frequencies, mode shapes, and damping with respect to the changes in the temperature and humidity. Three full-size PC girders, which were periodically vibration tested for one and a half

years to obtain their dynamic properties, were exposed to outdoor weather conditions outside a laboratory. Two of the PC girders were affected by the ASR whereas the third girder was kept at an inactive state by suppressing the acceleration of the ASR using the fly ash. First, the vibration characteristics of the girders, such as the vibration frequencies, mode shapes, and damping ratios, were extracted from the measurement data along with the ambient temperature and humidity during each test. The frequencies and damping ratios were then analyzed using linear regression models with respect to the variations in the temperature and humidity. The temperature and humidity increased in proportion with the decreases in the frequency and damping ratio, whereas no clear correlation of the mode shapes with the changes in the temperature and humidity could be observed. In addition, different dynamic behaviors were well observed in the three PC girders over the monitoring period. In particular, along with fewer ASR-induced cracks, the girder with fly ash exhibited higher vibration frequencies and lower damping ratios compared to the girders without the fly ash. Thus, the fly ash significantly affected the vibration properties of the PC girders subjected to the ASR-induced deteriorations. Because the Young's modulus of concrete is temperature dependent, the changes in the natural frequencies of the PC girders due to the ambient temperature can be simulated using a finite element (FE) model [15]. Another objective of this study includes performing validation tests of the numerical analyses against the results of the measurement by assuming the Young's modulus of concrete as a function of the temperature. The results showed that the validation model provided reasonable illustrations for the changes in the natural frequency of the vibration modes due to the changes in the ambient temperature.

### 4.2 Experimental procedure

To obtain free damped vibrations of the three PC girders, 14 accelerometers were placed on the girder with a constant interval of 1.15 m, as shown in **Fig. 4.1**. During each test, the impact excitations were applied alternately via a person jumping vertically from a chair (see **Fig. 4.2**) at four locations depicted as "x" in **Fig. 4.1**. At every impact location, the measurement was conducted two times, with 10000 data points collected at a sampling period of 5e−3 s each time. The vibration parameters of the PC girders were extracted from the measured data using the eigensystem realization algorithm (ERA) [16]. An FE model was then employed to conduct a structural eigenvalue analysis and estimate the natural frequency of the PC girder to compare the results with the measurements. Moreover, the ambient temperature and humidity were recorded simultaneously during the test using a thermometer. To track the variation in the vibrational parameters due to the environmental effects and ASR, eight tests were performed from May 2015 to September 2016 with 192 valid sets of vibration data.

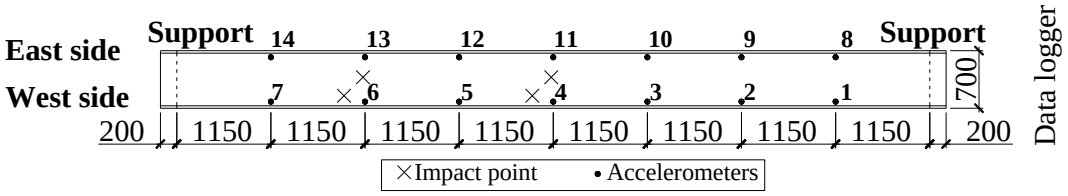


*Figure 4.1 Sensor layout on the PC girder.*

*Figure 4.2 Impact test and sensor layout on the PC girder.*

### 4.3 Environmental effect of PC girders on vibrational parameters

In this study, the first three modal properties were extracted from the measured data using the ERA [16]. **Figures 4.3(a)–(c)** show their typical shapes for modes 1, 2 and 3, respectively. In particular, modes 1 and 2 are the first and second bending modes, respectively, whereas mode 3 is the first mode of the torsional vibration. To evaluate the effects of the ambient temperature and humidity on the changes in the dynamic responses, linear regression analyses were performed on all modal properties of the girders. The results and discussions are presented in the following sections.

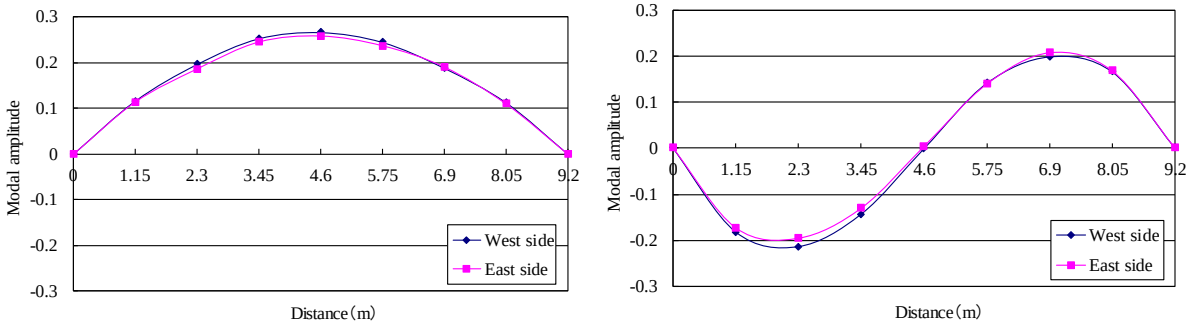


(a)The 1st bending mode (mode 1), f=9.593 Hz (b) The 2nd bending mode (mode 2), f=34.506 Hz

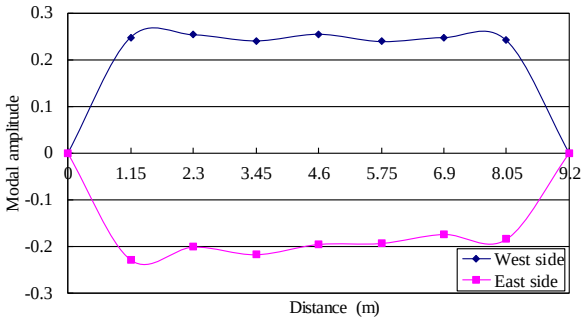


(c) The 1st mode of torsional vibration (mode 3), f=22.360 Hz

*Figure 4.3 Measured frequencies of girder No.3 in May 2015.*

### 4.3.1 Changes in natural frequencies

**(1) Evaluation of ambient-temperature effects**

**Figures 4.4(a)–(c), Figures 4.5(a)–(c), and Figures 4.6(a)–(c)** show the negative correlations between the three first modal frequencies of the girders and the ambient temperature (specified in degree Celsius throughout this study), which were measured during the monitoring period. These figures show that the amplitude of the vibrational frequency decreased with respect to the increased ambient temperature.

To obtain more information about the linear relationships of the natural frequencies with respect to the temperature, a linear regression model was proposed. The corresponding empirical equation of the natural frequency ($f$) as a function of the temperature ($T$) is as follows.

$$\mathrm{f} = \alpha_0 + \beta_t T + \varepsilon_f, \tag{4.1}$$

where $f$ is the natural frequency, $\alpha_0$ and $\beta_t$ are the regression coefficients named the intercept and the gradient, respectively, and $\varepsilon_f$ is the regression error. The measured ambient temperature was used as an explanatory variable. In this study, R was employed for statistical computing [17]. With regard to the results of the statistical analyses, **Tables 4.1–4.3** list the estimated regression coefficients for girders No.1, No.2, and No.3, respectively.

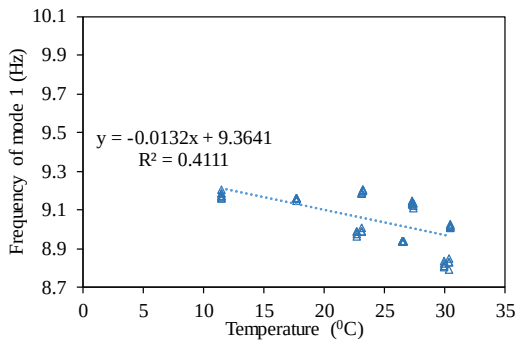


(a) Girder No.1

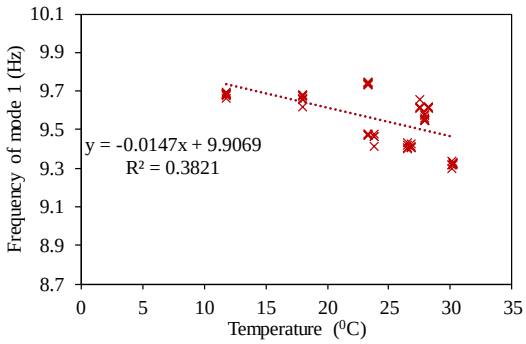


(b) Girder No.2

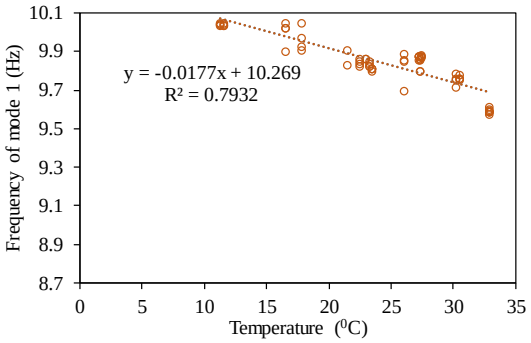


(c) Girder No.3

*Figure 4.4 Relation of frequencies of mode 1 to temperature.*

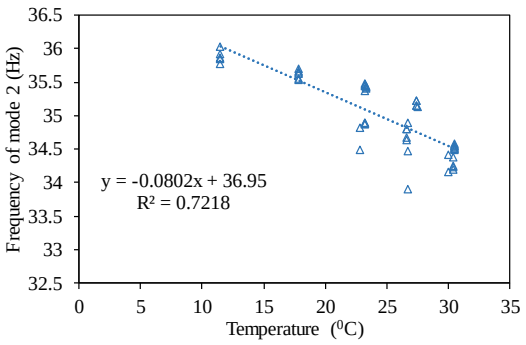


(a) Girder No.1

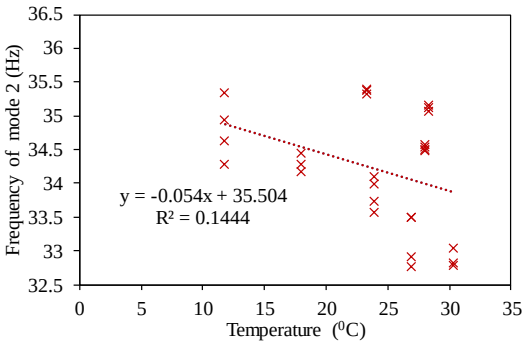


(b) Girder No.2

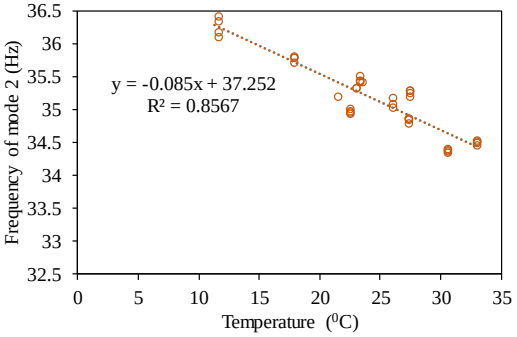


(c) Girder No.3

*Figure 4.5 Relation of frequencies of mode 2 to temperature.*

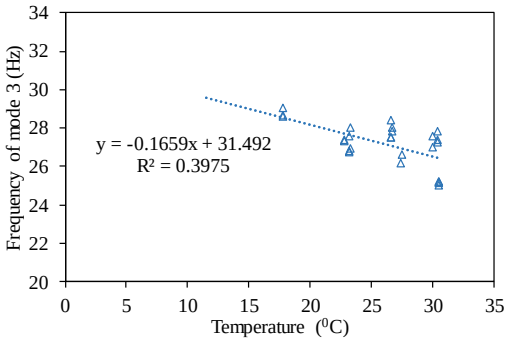


(a) Girder No.1

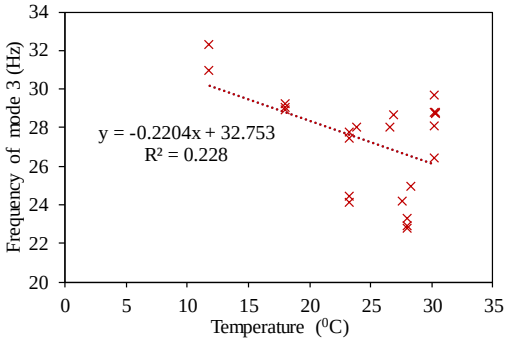


(b) Girder No.2

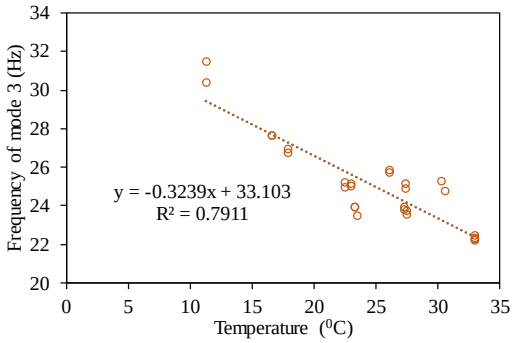


(c) Girder No.3

*Figure 4.6 Relation of frequencies of mode 3 to temperature.*

*Table 4.1 Coefficients of linear regression model (frequency ~ temperature) of girder No.1.*

| Mode | Intercept $\alpha_0$ | Gradient $\beta_t$ | Std. Error $\sigma_{\varepsilon_f}$ | $\sigma_{\varepsilon_f}/\alpha_0$ (%) | $\beta_t/\alpha_0$ (%) | Coefficient of determination $R^2$ |
|---|---|---|---|---|---|---|
| 1 | 9.3641 | -0.0132 | 0.0493 | 0.5269 | -0.1411 | 0.4111 |
| 2 | 36.9501 | -0.0802 | 0.1775 | 0.4803 | -0.2171 | 0.7218 |
| 3 | 31.4923 | -0.1659 | 1.0982 | 3.4872 | -0.5269 | 0.3975 |

*Table 4.2 Coefficients of linear regression model (frequency ~ temperature) of girder No.2.*

| Mode | Intercept $\alpha_0$ | Gradient $\beta_t$ | Std. Error $\sigma_{\varepsilon_f}$ | $\sigma_{\varepsilon_f}/\alpha_0$ (%) | $\beta_t/\alpha_0$ (%) | Coefficient of determination $R^2$ |
|---|---|---|---|---|---|---|
| 1 | 9.9069 | -0.0147 | 0.0581 | 0.5864 | -0.1489 | 0.3821 |
| 2 | 35.5043 | -0.0540 | 0.6280 | 1.7687 | -0.1520 | 0.1444 |
| 3 | 32.7528 | -0.2204 | 2.2470 | 6.8604 | -0.6729 | 0.2280 |

*Table 4.3 Coefficients of linear regression model (frequency ~ temperature) of girder No.3.*

| Mode | Intercept $\alpha_0$ | Gradient $\beta_t$ | Std. Error $\sigma_{\varepsilon_f}$ | $\sigma_{\varepsilon_f}/\alpha_0$ (%) | $\beta_t/\alpha_0$ (%) | Coefficient of determination $R^2$ |
|---|---|---|---|---|---|---|
| 1 | 10.2691 | -0.0177 | 0.0286 | 0.2785 | -0.1725 | 0.7932 |
| 2 | 37.2520 | -0.0850 | 0.1425 | 0.3825 | -0.2281 | 0.8567 |
| 3 | 33.1032 | -0.3239 | 0.8411 | 2.5408 | -0.9785 | 0.7911 |

From the above tables, the coefficients of determination $R^2$ for the three modes of girder No.3 were estimated at approximately 0.8. Moreover, in comparison to the other two girders, this coefficient was obtained at much lower values. Therefore, approximately 80% of the vibration-frequency variances of girder No.3 could be accounted for with respect to the ambient

temperature. In particular, a change of ~85.67% in the frequency of the second bending mode could be due to the change in temperature. However, changes of ~41.11, 72.18, and 39.75% in modes 1, 2, and 3, respectively, of girder No.1 were predictable, whereas the variance in the vibration frequency of girder No.2 was the least explainable among the three. The correlation levels were relatively moderate for girders No.1 and No.2 but fairly strong for girder No.3. **Figures 4.4, 4.5, and 4.6** show the fitted regression lines and corresponding equations. The standard deviations of the error (Std. Error $\sigma_{\varepsilon_f}$) were obtained as 0.0493, 0.1775, and 1.0982 for modes 1, 2, and 3 of girder No.1, respectively, as observed in **Table 4.1**. Dividing $\sigma_{\varepsilon_f}$ by the intercept ($\alpha_0$) yields 0.5269, 0.4803, and 3.4872%, which indicate the uncertainties due to other factors such as measurement noise, analysis error or effects of ambient humidity [8], and ASR-induced deterioration. Because the error ratio of the torsional mode was higher than that of the bending modes, it is found that the bending modes could be estimated more accurately than the torsional mode. Similar outcomes were also observed with respect to the vibration modes of the other two girders. To quantify the effect of the measured temperature on the frequency change, the gradients ($\beta_t$) were normalized to the intercepts ($\alpha_0$). The results show that, for all girders, the torsional frequencies decreased by 0.52–0.97% as the temperature increased by 1 ºC, whereas the measured frequencies of the bending modes decreased by approximately 0.1–0.2%.

**(2) Evaluation of ambient-humidity effects**

In this study, the effect of humidity variation on the change in the vibration frequency of the PC girders was analyzed. **Figures 4.7(a)–(c), Figures 4.8(a)–(c), and Figures 4.9(a)–(c)** show the correlations of all the identified data of the first three modal frequencies with respect to the ambient humidity (specified in percent throughout this study). These figures demonstrate that all the three frequencies decreased with the increase in the humidity. Moreover, the relationship between the measured frequencies and the humidity was relatively linear.

The linear regression analyses were performed to investigate the goodness of fit of the linear relationship using R [17]. A linear regression model was proposed. The corresponding empirical equation of the natural frequency (*f*) as a function of the humidity (*H*) is assumed as follows.

$$\mathrm{f} = \alpha_0 + \beta_h H + \varepsilon_f, \tag{4.2}$$

where *f* is the natural frequency, $\alpha_0$ and $\beta_h$ are the regression coefficients named the intercept and the gradient, respectively, and $\varepsilon_f$ is the regression error. With regard to the results of the statistical analyses, **Tables 4.4–4.6** list the estimated regression coefficients for girder No.1, No.2, and No.3, respectively.

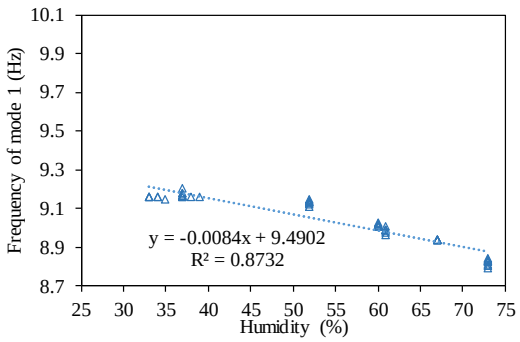


(a) Girder No.1

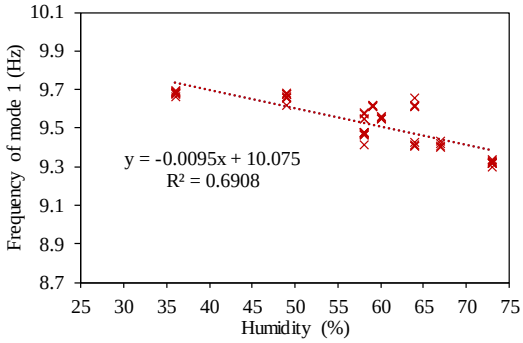


(b) Girder No.2

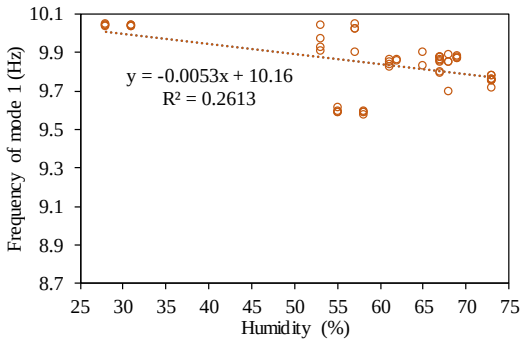


(c) Girder No.3

*Figure 4.7 Relation of frequencies of mode 1 to humidity.*

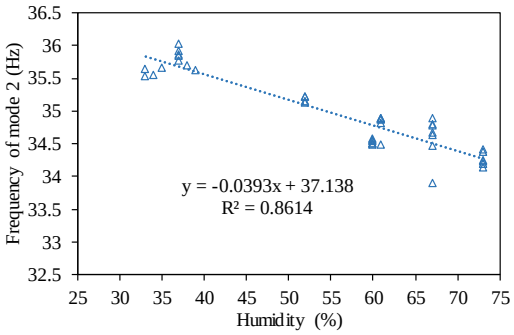


(a) Girder No.1

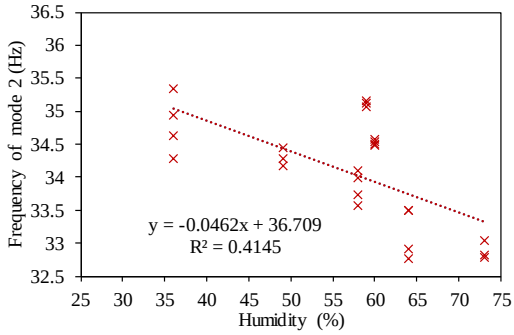


(b) Girder No.2

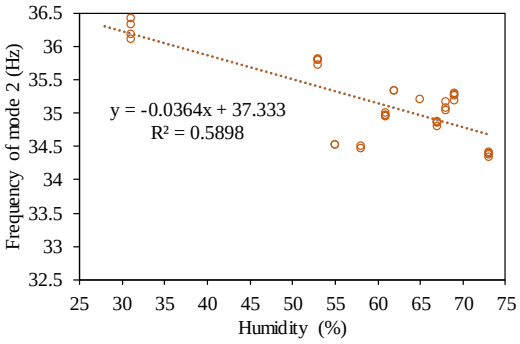


(c) Girder No.3

*Figure 4.8 Relation of frequencies of mode 2 to humidity.*

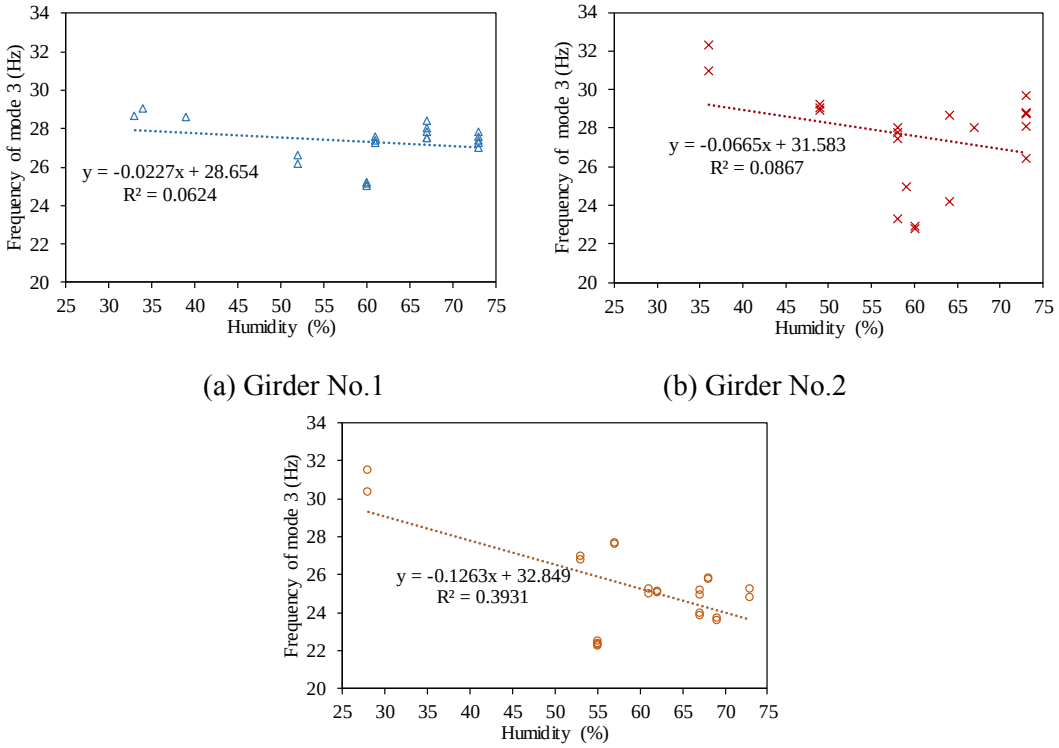


(a) Girder No.1 (b) Girder No.2

(c) Girder No.3

*Figure 4.9 Relation of frequencies of mode 3 to humidity.*

*Table 4.4 Coefficients of linear regression model (frequency ~ humidity) of girder No.1.*

| Mode | Intercept $\alpha_0$ | Gradient $\beta_t$ | Std. Error $\sigma_{\varepsilon_f}$ | $\sigma_{\varepsilon_f}/\alpha_0$ (%) | $\beta_t/\alpha_0$ (%) | Coefficient of determination $R^2$ |
|---|---|---|---|---|---|---|
| 1 | 9.4902 | -0.0084 | 0.0251 | 0.2643 | -0.0885 | 0.8732 |
| 2 | 37.1382 | -0.0393 | 0.1450 | 0.3904 | -0.1058 | 0.8614 |
| 3 | 28.6544 | -0.0227 | 1.2469 | 4.3514 | -0.0792 | 0.0624 |

*Table 4.5 Coefficients of linear regression model (frequency ~ humidity) of girder No.2.*

| Mode | Intercept $\alpha_0$ | Gradient $\beta_t$ | Std. Error $\sigma_{\varepsilon_f}$ | $\sigma_{\varepsilon_f}/\alpha_0$ (%) | $\beta_t/\alpha_0$ (%) | Coefficient of determination $R^2$ |
|---|---|---|---|---|---|---|
| 1 | 10.0751 | -0.0095 | 0.0504 | 0.5005 | -0.0940 | 0.6908 |
| 2 | 36.7092 | -0.0462 | 0.6605 | 1.7993 | -0.1260 | 0.4145 |
| 3 | 31.5830 | -0.0665 | 3.0309 | 9.5965 | -0.2107 | 0.0867 |

*Table 4.6 Coefficients of linear regression model (frequency ~ humidity) of girder No.3.*

| Mode | Intercept $\alpha_0$ | Gradient $\beta_t$ | Std. Error $\sigma_{\varepsilon_f}$ | $\sigma_{\varepsilon_f}/\alpha_0$ (%) | $\beta_t/\alpha_0$ (%) | Coefficient of determination $R^2$ |
|---|---|---|---|---|---|---|
| 1 | 10.1603 | -0.0053 | 0.0735 | 0.7236 | -0.0524 | 0.2613 |
| 2 | 37.3333 | -0.0364 | 0.3276 | 0.8774 | -0.0974 | 0.5898 |
| 3 | 32.8495 | -0.1263 | 2.0293 | 6.1777 | -0.3845 | 0.3931 |

The coefficients of determination $R^2$ for the three frequencies of girder No.3 were 0.2613, 0.5898, and 0.3931, respectively, and the corresponding correlation coefficients R were 0.5112, 0.768, and 0.627, respectively, implying that there was a moderate correlation between the two variables. For girders No.1 and No.2, the $R^2$ factors for the two bending modes were estimated respectively as 0.8732 and 0.8614 and 0.6908 and 0.4145, respectively, which yielded high values of the correlation coefficient R, i.e., 0.9345 and 0.9281 for girder No.1 and 0.8314 and 0.644 for girder No.2. Thus, there was a good correlation between the frequencies of the bending modes with respect to the ambient humidity with regard to the two girders. In contrast, with regard to the torsional modes, the linear relationships between the two variables were weak because of the low coefficients of determination $R^2$. The result of the regression analysis shows that the ambient humidity affected the frequencies of the bending modes of the girders No.1 and No.2 more significantly than that of girder No.3. As a previous study of Xia et al. [8], it was considered that the concrete could absorbed more water and thereby its mass would be increased in high humidity environment. The negative relation between the natural frequency and the humidity was also evaluated and confirmed in that study. In the present study, because of the ASR-induced cracks, it was believed that water could be absorbed and dispersed easily in the girders No.1 and No.2. Thus, these two girders were more sensitive to the ambient humidity than girder No.3 containing the fly ash. For a detailed comparison between the three girders, the gradients ($\beta_t$) were normalized to the intercepts ($\alpha_0$). It was found that the frequencies of the two bending modes of girder No.3 varied by ~0.052% and ~0.097% when the humidity changed by 1%. With regard to the frequencies of girders No.1 and No.2, the rates were calculated at higher values, which were 0.088–0.106% and 0.094–0.126%, respectively. For the torsional mode, the results differ significantly with the changes in the bending modes. **Figures 4.7, 4.8, and 4.9** show the fitted regression lines and corresponding equations.

**(3) Combined effect of ambient temperature and humidity**

As another form of the linear regression analysis, multiple linear regression was employed to explain the combined effect of the ambient temperature and humidity (independent variables) on the natural frequency (dependent variable). Assuming the humidity as the second variable,

the empirical equation of the frequency (*f*) as a function of the temperature (*T*) and humidity (*H*) is given as follows.

$$f = \alpha_0 + \beta_t T + \beta_h H + \varepsilon_f, \quad (4.3)$$

where *f* is the natural frequency, $\alpha_0$, $\beta_t$, and $\beta_h$ are the intercept and the gradients of the temperature and humidity, respectively, and $\varepsilon_f$ is the regression error. **Tables 4.7–4.9** list the outcomes for girders No.1, No.2, and No.3, respectively. The results of the $R^2$ statistics were estimated at 0.8815, 0.8725, and 0.8618 for the three vibration modes of girder No.3, and the corresponding correlation coefficients R were obtained respectively as 0.9389, 0.9341, and 0.9283, which are significantly higher than the previous results wherein the humidity and temperature were considered separately. The strong correlations between the three variables demonstrate that the ambient humidity and temperature significantly affected the changes in the frequencies of the vibration modes of girder No.3. In addition, the regression analyses for girders No.1 and No.2 yielded similar results because the coefficients of determination were high. The results of the uncertainty evaluation show that the percentage ratios between $\sigma_{\varepsilon_f}$ and $\alpha_0$ were largely lower than the previous errors. However, the uncertainties in the torsional mode of the three girders were obtained respectively as ~2.98, ~6.47, and ~2.95%, which were clearly higher than that of the two bending modes. The fluctuations in estimating the torsional properties are high because the torsional mode is not only affected by the environmental conditions and errors in the measurements and analyses but also governed by the shear rigidity of the structure, which differs from the bending rigidity in terms of the sensitivity to the temperature and humidity [8].

The selected regression models were only suitable for a temperature range of 11.45–33 ºC and a humidity range of 28–73% as presented in this study. Moser and Moaveni [18] showed that for a two-span continuous steel frame bridge, the relationships between the natural frequencies of six identified modes and the measured temperature were nonlinear when the temperature ranged from −14 ºC to 39 ºC.

*Table 4.7 Coefficients of linear regression model (frequency ~ temperature + humidity) of girder No.1.*

| Mode | Intercept $\alpha_0$ | Std. Error $\sigma_{\varepsilon_f}$ | $\sigma_{\varepsilon_f}/\alpha_0$ (%) | Coefficient of determination $R^2$ | Correlation coefficient R |
|---|---|---|---|---|---|
| 1 | 9.4809 | 0.0235 | 0.2483 | 0.8923 | 0.9446 |
| 2 | 37.2076 | 0.1291 | 0.3470 | 0.8954 | 0.9463 |
| 3 | 31.6610 | 0.9425 | 2.9768 | 0.6576 | 0.8109 |

*Table 4.8 Coefficients of linear regression model (frequency ~ temperature + humidity) of girder No.2.*

| Mode | Intercept $\alpha_0$ | Std. Error $\sigma_{\varepsilon_f}$ | $\sigma_{\varepsilon_f}/\alpha_0$ (%) | Coefficient of determination $R^2$ | Correlation coefficient R |
|---|---|---|---|---|---|
| 1 | 10.1880 | 0.0514 | 0.5046 | 0.7691 | 0.8770 |
| 2 | 38.7192 | 0.4317 | 1.1150 | 0.8454 | 0.9195 |
| 3 | 25.9808 | 1.6800 | 6.4663 | 0.7848 | 0.8859 |

*Table 4.9 Coefficients of linear regression model (frequency ~ temperature + humidity) of girder No.3.*

| Mode | Intercept $\alpha_0$ | Std. Error $\sigma_{\varepsilon_f}$ | $\sigma_{\varepsilon_f}/\alpha_0$ (%) | Coefficient of determination $R^2$ | Correlation coefficient R |
|---|---|---|---|---|---|
| 1 | 10.1673 | 0.0297 | 0.2923 | 0.8815 | 0.9389 |
| 2 | 37.3092 | 0.1855 | 0.4973 | 0.8725 | 0.9341 |
| 3 | 33.8330 | 0.9980 | 2.9499 | 0.8618 | 0.9283 |

**(4) Evaluation of the effects of ASR-induced deterioration**

Another important result is the difference in the frequencies of the three girders over the monitoring period. For each measurement, the vibration test was replicated eight times in total, and the average values were calculated. **Figures 4.10(a)–(c)** show the time histories of the average natural frequencies of the three modes over one and a half years. However, the frequencies of the torsional mode were similar. The differences in the measured frequencies of the three girders clearly manifested over time with regard to the two bending modes. Moreover, the bending frequency of girder No.3 was the highest as compared to the results obtained for girders No.1 and No.2 at each measuring time. In terms of the first bending mode, the frequencies of girder No.1 exhibited much lower values than those of the two other girders. In September 2016, as compared to the result obtained for girder No.3, the frequencies of girders No.1 and No.2 were lower by ~9.6 and ~4.5%, respectively. With regard to the second bending mode, the frequencies of the three girders were approximately the same at the initial measurements because the differences in the identified data were obtained as approximately 0.06% in May 2015. Since November 2015, the difference became pronounced, and until the end of the monitoring period, the frequencies of girder No.3 was ~4.54% greater than that of girder No.2. Because the cross sections of the three girders were the same with fairly similar mixtures, and were tested alternately in a short time during each measurement, the difference in the natural frequency of the bending modes was probably not due to the changes in temperature and humidity. One of the possible reasons for the difference is that girders No.1 and No.2 were affected by the ASR deteriorations, thereby forming many cracks that

propagated longitudinally on the top and both side surfaces of the girders and leading to the decrease in the Young's modulus of concrete. Sugiura et al. [19] studied the girders No.2 and No.3 and showed that the expansion rate of concrete in the transverse direction, which was the primary cause of the longitudinal ASR-induced cracks, increased significantly since early October 2015 in girder No.2. In addition, fracture mechanics states that the occurrence of a crack in a structure causes a local flexibility influencing its dynamic responses [20]. Dimarogonas [20] proposed that for a small crack depth, the local flexibility ($\Delta c$) is a function of $(a/h)^2$ where $a$ is the crack depth and $h$ is the height of the beam. Assuming that the intact beam has a flexibility ($c$), the total flexibility ($C$) after the formation of a crack and the corresponding structural stiffness ($K$) can be obtained as follows.

$$\mathrm{C} = \mathrm{c} + \Delta\mathrm{c}, \tag{4.4}$$

$$\mathrm{K} = \frac{1}{\mathrm{C}} = \frac{1}{c+\Delta C} = \frac{1}{c+\lambda\left(\frac{a}{h}\right)^2}, \tag{4.5}$$

where $\lambda = 1.86\left(\frac{6\pi h}{EI}\right)$ is a constant. Likewise, the radian frequency ($\omega_n$) of the crack-free beam will vary with respect to $\Delta\omega_n$, and the total radian frequency will be $\omega_n' = \omega_n + \Delta\omega_n$. In addition, because the natural frequency ($f_n$) can be obtained by dividing $\omega_n$ by 2π, the change ($\Delta f_n$) due to the formation of the crack should be equal to $\Delta\omega_n/2\pi$. For a single degree of freedom oscillator, the natural frequency depends on the system properties such as mass ($m$) and stiffness ($K$). Given that there is a small crack in the structure, the radian frequency ($\omega_n'$) can be defined using the following relationship.

$$(\omega_n')^2 = (\omega_n + \Delta\omega_n)^2 = {\omega_n}^2 + 2\omega_n\Delta\omega_n + {\Delta\omega_n}^2 = \frac{K}{m} = \frac{1}{m\left(c+\lambda\left(\frac{a}{h}\right)^2\right)} = \frac{1}{mc\left(1+\frac{\lambda}{c}\left(\frac{a}{h}\right)^2\right)}. \tag{4.6}$$

Assuming that $\frac{\lambda}{c}\left(\frac{a}{h}\right)^2 = \frac{\Delta c}{c}$ is much less than 1 and neglecting the higher order terms ${\Delta\omega_n}^2$, the following equation can be obtained.

$${\omega_n}^2 + 2\omega_n\Delta\omega_n = \frac{1}{mc} - \frac{\lambda}{c}\left(\frac{a}{h}\right)^2. \tag{4.7}$$

Therefore, the changes in the radian frequency ($\Delta\omega_n$) and natural frequency ($\Delta f_n$) can be obtained using **Eqs. (4.8) and (4.9)**, respectively.

$$\Delta\omega_n = -\frac{\lambda}{2\omega_n c}\left(\frac{a}{h}\right)^2, \tag{4.8}$$

$$\Delta\mathrm{f}_n = -\frac{\lambda}{4\pi\omega_n c}\left(\frac{a}{h}\right)^2. \tag{4.9}$$

Accordingly, the relationship between the occurrence of cracks and the decrease in the natural frequency is proved. Moreover, because the expansion of the ASR was effectively suppressed by the fly ash, the frequency variation of girder No.3 was largely due to the environmental

effects. Within one and a half years of investigation, as the ambient temperature and humidity varied by approximately 21.55 ºC and 45%, respectively, the bending modal frequencies of girder No.3 varied in the range of ~3–5%, which is considerable compared to those due to the structural damage. Hence, the effects of the environmental conditions should be considered carefully when using the variation in the vibrational frequency to evaluate the health of structures.

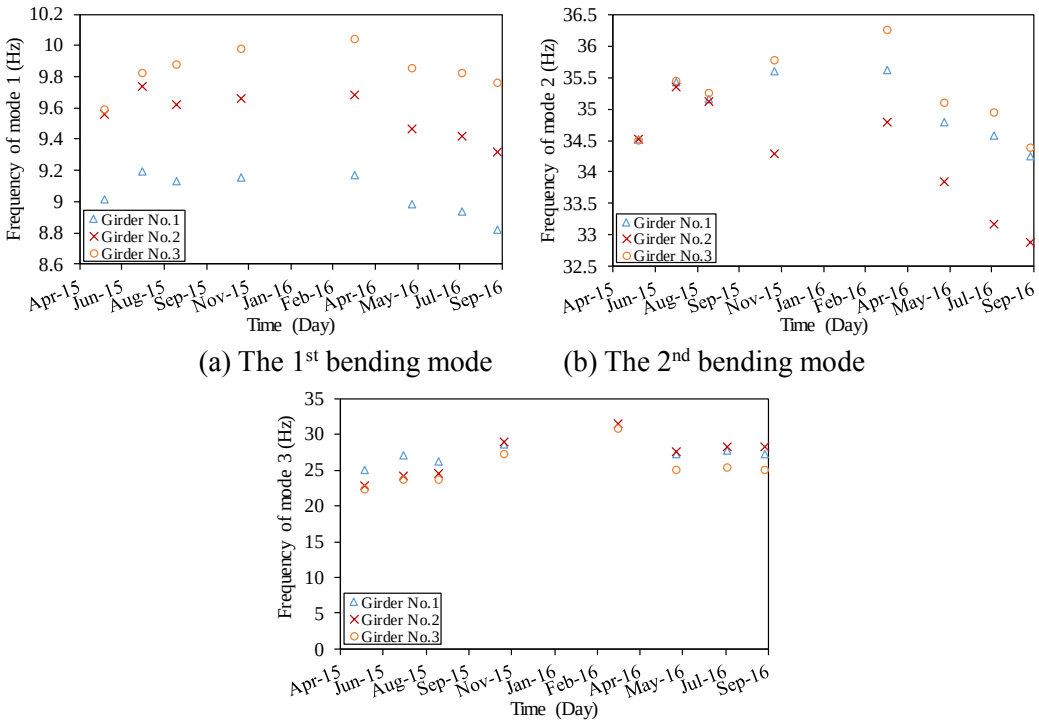


(a) The 1st bending mode (b) The 2nd bending mode

(c) The 1st torsional mode

*Figure 4.10 Difference in natural frequencies of three girders.*

### 4.3.2 Variation in damping ratio

The damping ratio was extracted from the measured data to examine the changes due to the ambient temperature and humidity. **Figures 4.11(a)–(c) and Figures 4.12(a)–(c)** show the identified damping ratios of the three vibration modes of girder No.3 with respect to the ambient temperature and humidity, respectively. Except for **Figure 4.12(a)**, which shows a weak positive relationship with the humidity, the rest of the figures demonstrate that the damping ratios relatively decrease with the increases in the environmental parameters.

Using R [17], the regression models were then developed to evaluate the linear correlations between the variables. A governing equation of the linear regression model of the damping ratio (d) as a function of the temperature (T) was proposed as follows.

$$\mathrm{d} = \alpha_0 + \beta_t T + \varepsilon_f, \tag{4.10}$$

where d is the damping ratio, $\alpha_0$ and $\beta_t$ are the intercept and the gradient, respectively, and $\varepsilon_f$ is the regression error. **Table 4.10** lists the results of the statistical analysis for girder No. 3. The gradients were obtained respectively as −0.0001, −0.0002, and −0.0007 for the three modes, indicating that the damping ratios increased slightly with the decrease in the temperature as described in **Figs. 4.13(a)–(c)**. In these figures, the average values were calculated for each measurement and plotted to find the pattern of the damping variation over time. However, the coefficients of determination $R^2$ were estimated at low values, which were 0.03, 0.2159, and 0.1843 for modes 1, 2, and 3, respectively. Additionally, the standard deviation of the errors occupied large proportions of the intercept, which were above ~6.4%. Attempts were made to evaluate the relationship between the damping ratios and ambient humidity. Another linear regression equation was similarly developed for the investigation. **Table 4.11** lists the coefficients of the linear regression model of the damping ratio with respect to the humidity. Because the $R^2$ statistics were low and the identified noises were rather high at approximately 12% for modes 1 and 3 and ~8% for mode 2, the results were similar to those obtained with respect to the ambient temperature. In addition, a multiple linear regression model was considered to analyze the variation in the damping ratio under the combined effect of the ambient temperature and humidity. As an outcome of the model for girder No.3, the $R^2$ statistics were estimated at 0.1843, 0.2499, and 0.2539 for the three vibration modes, and the corresponding correlation coefficient R were obtained respectively as 0.4293, 0.4999, and 0.5039, which were quite higher than the ones obtained for the single linear models. Based on the above statistical parameters, the effects of the measured humidity and temperature on the change in the damping ratio were evaluated as weak correlations in this study. Similar outcomes were found with respect to the damping ratios of the other two girders. Thus, the changes in the damping ratio were not only affected by the ambient temperature and humidity but also governed by other factors. However, it is difficult to determine the damping ratio with sufficient accuracy to estimate the correlations with the temperature, as reported in previous studies [8,18,20].

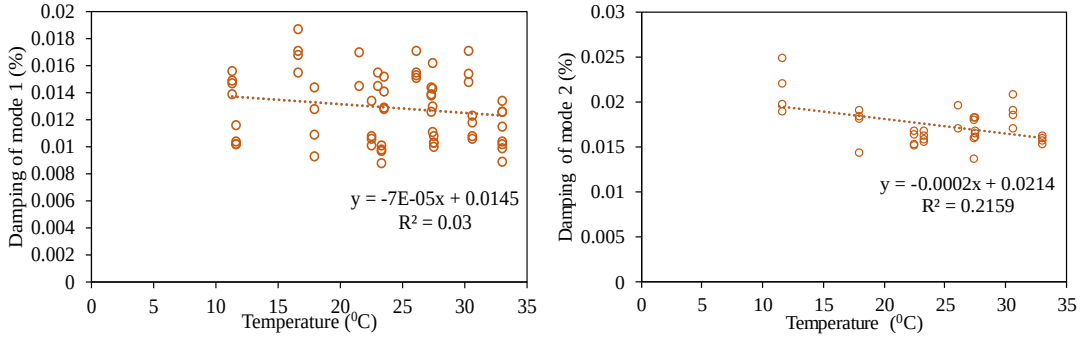


(a) mode 1 (b) mode 2

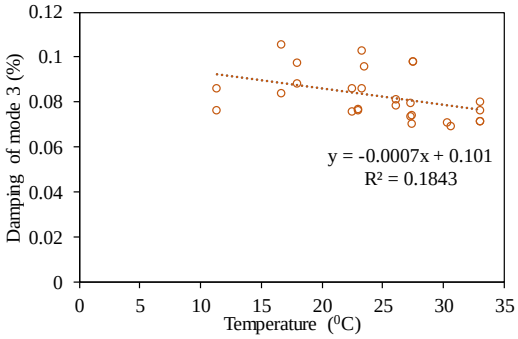


(c) mode 3

*Figure 4.11 Relation of damping ratios of girder No.3 to temperature.*

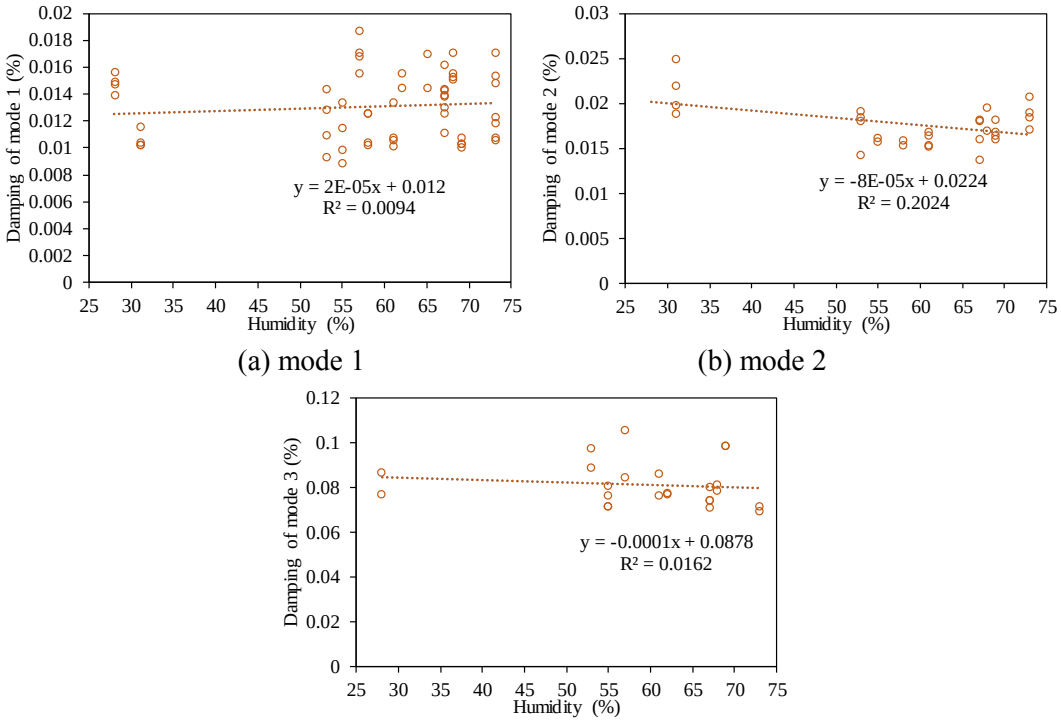


(a) mode 1 (b) mode 2

(c) mode 3

*Figure 4.12 Relation of damping ratios of girder No.3 to humidity.*

*Table 4.10 Coefficients of linear regression model (damping ratio ~ temperature) of girder No.3.*

| Mode | Intercept $\alpha_0$ | Gradient $\beta_t$ | Std. Error $\sigma_{\varepsilon_f}$ | $\sigma_{\varepsilon_f}/\alpha_0$ (%) | $\beta_t/\alpha_0$ (%) | Coefficient of determination $R^2$ |
|---|---|---|---|---|---|---|
| 1 | 0.0145 | -0.0001 | 0.0012 | 8.1397 | -0.4504 | 0.0300 |
| 2 | 0.0214 | -0.0002 | 0.0014 | 6.4610 | -0.7625 | 0.2159 |
| 3 | 0.1010 | -0.0007 | 0.0079 | 7.8235 | -0.7360 | 0.1843 |

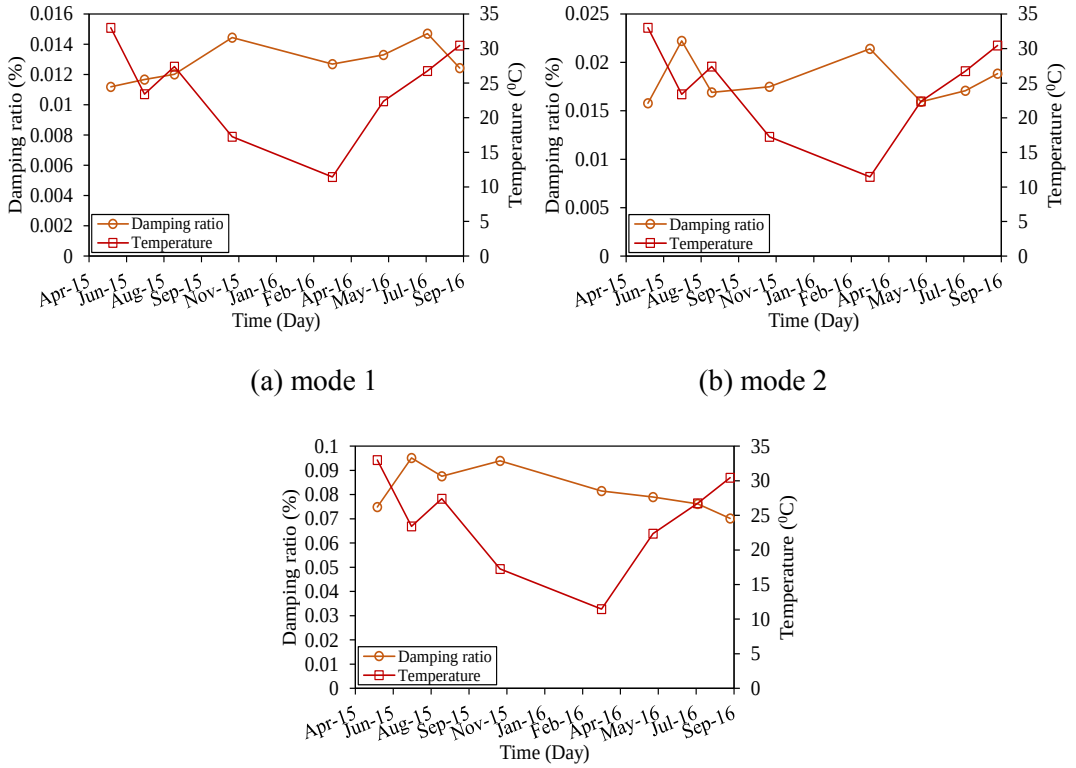


(a) mode 1 (b) mode 2

(c) mode 3

*Figure 4.13 Variations in average damping ratios of girder No.3 over one and a half years.*

*Table 4.11 Coefficients of linear regression model (damping ratio ~ humidity) of girder No.3.*

| Mode | Intercept $\alpha_0$ | Gradient $\beta_t$ | Std. Error $\sigma_{\varepsilon_f}$ | $\sigma_{\varepsilon_f}/\alpha_0$ (%) | $\beta_t/\alpha_0$ (%) | Coefficient of determination $R^2$ |
|---|---|---|---|---|---|---|
| 1 | 0.0120 | 0.00002 | 0.0015 | 12.5748 | 0.1482 | 0.0094 |
| 2 | 0.0224 | -0.00008 | 0.0018 | 8.2411 | -0.3624 | 0.2024 |
| 3 | 0.0878 | -0.00011 | 0.0111 | 12.6373 | -0.1255 | 0.0163 |

In addition, the cracks in a structure not only affect the structural stiffness [8,21,22] but also lead to variations in the structural damping ratio because of the appearance of plastic zones along the edges of the cracks [20]. Curadelli et al. [23] showed the difference in the instantaneous damping coefficient between the healthy and damaged condition of a reinforced concrete beam. They clearly demonstrated that the variation in the damping was considerable and the instantaneous damping coefficients of the undamaged state were lower than of the measured ones at the final loading step with respect to all the vibration amplitudes. In the present study, the difference in the damping ratios of the three girders over the monitoring period was analyzed accordingly. **Figures 4.14(a)–(c)** show the time histories of the average damping coefficients over the follow-up period. Apart from the first torsional mode (mode 3),

wherein the difference in the amplitude was insignificant, the damping ratios of the other modes changed considerably, representing the difference between the girders. With regard to the damping of the first bending mode (mode 1), all the identified values of girder No.1 were clearly higher than that of girders No.2 and No.3, which were similar in terms of the amplitude. With regard to the second bending mode (mode 2), the damping ratios of the three girders were largely equal at the three initial measurements. The differences became apparent since November 2015. From the data of September 2016, the average damping ratios of the girders No.2 and No.1 were approximately 2 and 1.5 times, respectively, greater than the identified value of girder No.3. As the correlations with the changes in the ambient environmental parameters were low, the difference in the damping coefficients in the two bending modes of the three girders was probably due to the increase in the longitudinal crack propagation due to the ASR-induced expansion, which led to the increase in the number of plastic zones in girders No.1 and No.2.

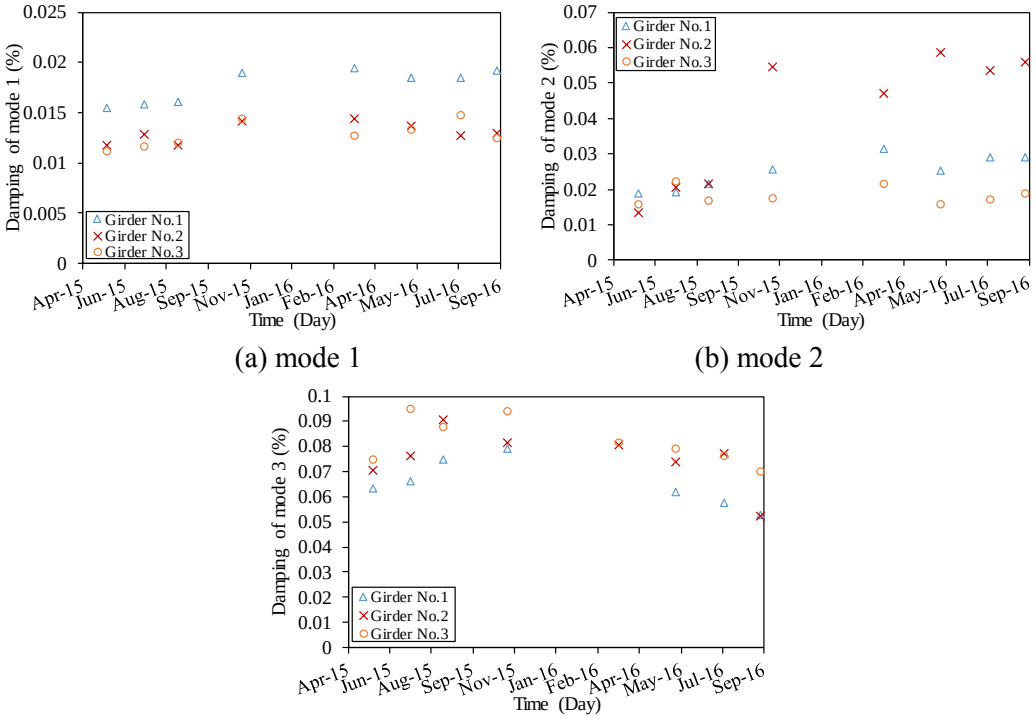


(a) mode 1 (b) mode 2

(c) mode 3

*Figure 4.14 Difference in damping ratios of three girders.*

### 4.3.3 Variation in mode shapes

In this study, the variations in the mode shape due to the environmental effects were examined using the modal assurance criterion (MAC) [24], which is a simple index used to characterize the effects of the damage on the mode shapes. The MAC reflects the degree of relationship between the two modal curves, which were extracted from the acceleration data obtained at

different states of a structure. The MAC can be computed as follows.

$$MAC = \frac{\left(\sum_{j=1}^{n} \psi_{Ij}\psi_{Dj}\right)^2}{\sum_{j=1}^{n} \psi_{Ij}{}^2 \sum_{j=1}^{n} \psi_{Dj}{}^2}, \quad (4.11)$$

where $\psi_{Ij}$ and $\psi_{Dj}$ *(j=1~n+1)* are the identified mode shape values at the $j^{th}$ point of the intact and damaged modal vectors, respectively, and *n* indicates the number of observation points of a vibration mode. In the case wherein there are no differences due to the structural change in the two sets of the mode shapes, the MAC value would be equal to unity. However, the MAC value might decrease in amplitude to zero if any variation exists in the structural properties, thereby reducing the correlation degree between the two mode shapes. To determine the MAC, the analytical mode shapes, as shown in **Figs 4.15(a) and 4.15(b)**, were used as reference lines. **Figures 4.16(a), 4.16(b), 4.17(a) and 4.17(b)** show the identified MAC values of the two bending modes with respect to the temperature and humidity. **Figures 4.16(a) and 4.16(b)** show that the scatters seen in all the MAC values are significant with no notable pattern reflecting the variation in the amplitude with respect to the ambient temperature. The obtained values are higher than 0.97 and 0.9 for the two bending modes, which are approximately close to unity. Similarly, **Figures 4.17(a) and 4.17(b)** show no clear trend in the MAC changes due to the measured humidity. Because all the coefficients of determination obtained from the multiple linear regression analysis were estimated to be lower than 0.2, the correlation levels with the temperature and humidity were weak in terms of the MAC values of the two bending modes. Although it is widely accepted that the MAC is a useful indicator of the changes in the structural performance, it is not sensitive to the uniform changes throughout the structure [8]. In fact, the ambient temperature and humidity affect the entire girder uniformly [8], and consequently, the effects of the environmental conditions on the MAC values were observed at low levels. The results obtained in this study help confirm this observation. **Figures 4.18(a) and 4.18(b)** show the time histories of the identified MAC values of the first and second bending modes, respectively, to compare between the three girders over the monitoring period. With regard to mode 1, the MAC values of girders No.1 and No.2 are relatively lower than those of girder No.3. However, no significant separation in the amplitude was observed. A similar observation regarding mode 2 was found for all the girders. Hence, no clear difference was found in the magnitude of the MAC values considered in this study. Because the torsional mode could not be estimated precisely for all the girders as mentioned in the previous section, its MAC values are not reported in this section.

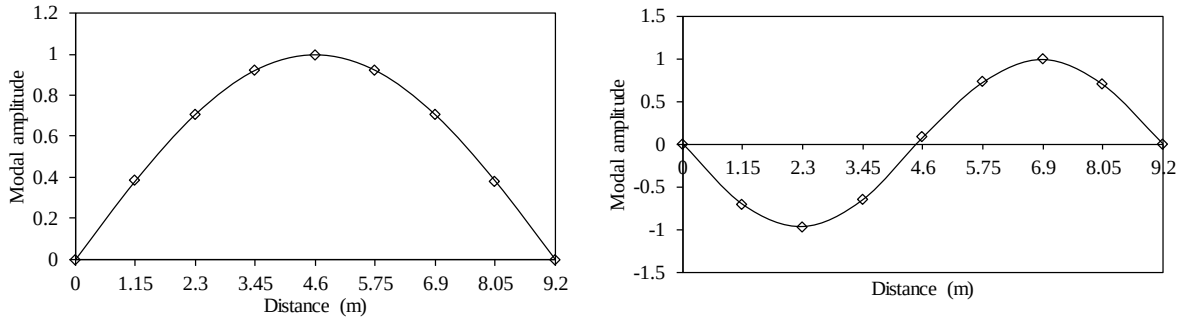


(a) The 1st bending mode (mode 1) (b) The 2nd bending mode (mode 2)

*Figure 4.15 Two analytical mode shapes.*

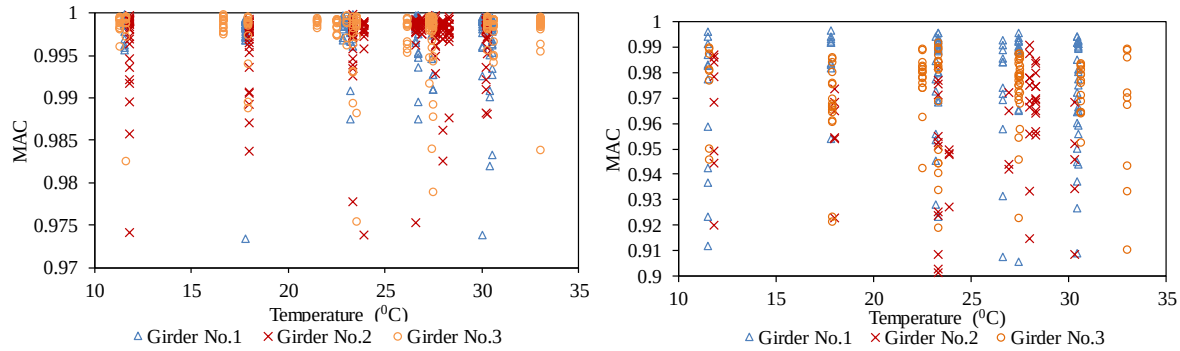


(a) The 1st bending mode (mode 1) (b) The 2nd bending mode (mode 2)

*Figure 4.16 Identified MAC values of two bending modes versus measured ambient temperature.*

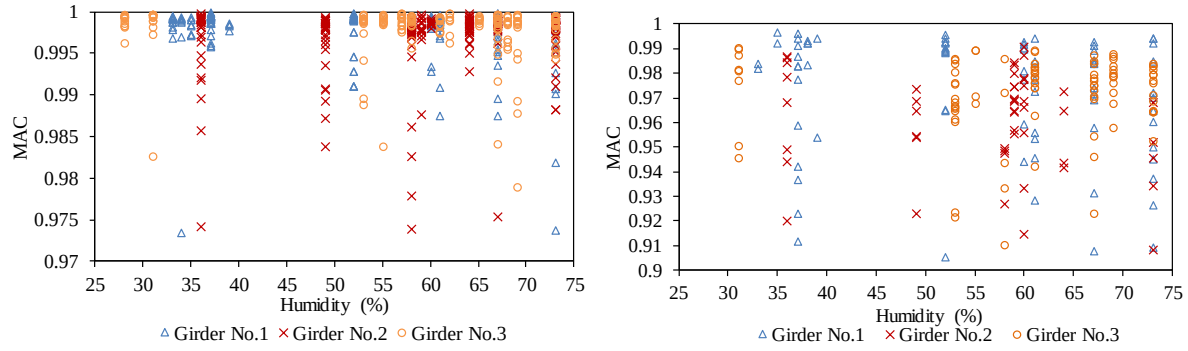


(a) The 1st bending mode (mode 1) (b) The 2nd bending mode (mode 2)

*Figure 4.17 Identified MAC values of two bending modes versus measured humidity.*

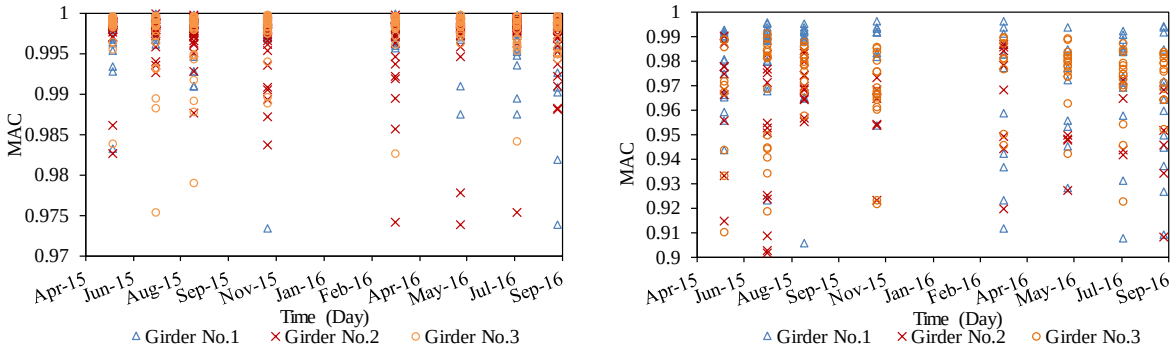


(a) The 1st bending mode (mode 1) (b) The 2nd bending mode (mode 2)

*Figure 4.18 Time histories of MAC values for three girders.*

## 4.4 Numerical modeling

### 4.4.1 Eigenvalue structural analysis

To evaluate the accuracy of the measurement, a three-dimensional (3D) model was produced using FX+ for DIANA, which is a commercially available program for FE analysis. The properties and boundary conditions of the numerical model were the same as those of the actual PC girder. **Figure 4.19** shows the diagram of a 3D model used for the eigenvalue structural analysis in DIANA [25]. The objective model was a PC girder supported by two points with a span length of 9200 mm. As a PC girder, it contained 16 PC steel strands (SWPR7BL1S 12.7 mm). The strands had D10-type stirrups arranged around them. The PC strands and stirrups were modeled as bars in the beam elements. The bonding forces between the concrete and strands were assumed complete. **Table 4.12** lists the parameters of the concrete for the analysis. Moreover, the stirrups were assumed as linear elastic materials with a Young's modulus $E_s = 210000\ \mathrm{N/mm^2}$ and Poisson's ratio ν = 0.3. Moreover, the PC steel material was considered made of steel with Young's modulus $E_s = 210000\ \mathrm{N/mm^2}$ and Von Mises yield stress $\sigma_y = 1580\ \mathrm{N/mm^2}$. The mass density for the steel materials was selected as 7.7e−9 T/mm$^3$. Regarding the prestressing force for reinforcement, a value of 1225.3 N/mm$^2$ was assigned to the first layer of PC strands in the compression area (4 strands) while the other two layers in the tension area (6 strands) were subjected to a presstress of 1166.7 N/mm$^2$. **Figures 4.20(a) and 4.20(b)** show the modal shapes of the two bending modes of girder No.3 and the corresponding frequencies, which are quite similar to the measured modes shown in **Figs. 4.3(a) and 4.3(b)**, respectively.

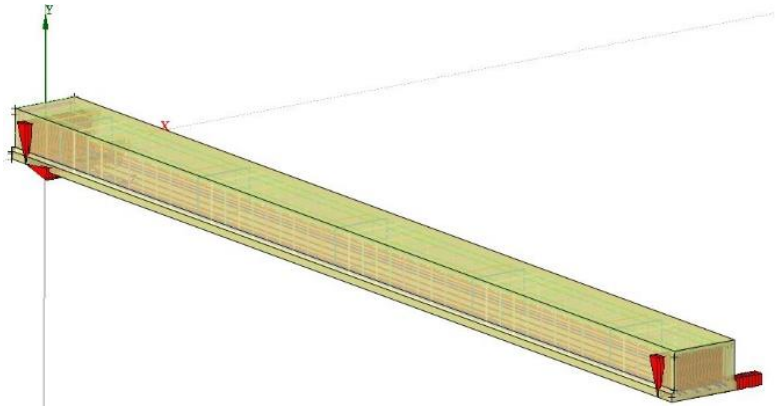

*Figure 4.19 A 3D model of the PC girder.*

*Table 4.12 Material parameters of concrete for eigenvalue analysis.*

| | | | |
|---|---|---|---|
| Young's modulus | $E_c$ | 38700 | $N/mm^2$ |
| Poisson's ratio | ν | 0.16 | |
| Mass density | ρ | 2.45e–9 | $T/mm^3$ |

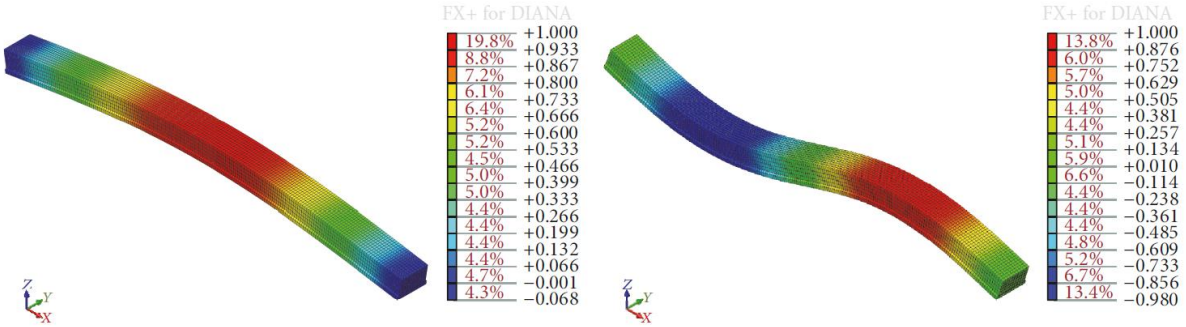


(a) Analytical 1st bending mode, f=9.576 Hz (b) Analytical 2nd bending mode f=37.054 Hz

*Figure 4.20 Analysis results of natural frequencies of girder No.3 in May 2015.*

### 4.4.2 Validation

Over the years, many researchers have proved that the temperature change affects not only the thermal properties but all the mechanical properties of the concrete such as the compressive strength, tensile strength, Young's modulus, and stress–strain relationship [26–28]. In particular, the variation in the compressive strength of the concrete at elevated temperatures (from 100 ºC to 1000 ºC) was considerable, whereas the variation was less in the range of 0–100 ºC because the relative compressive strength was close to unity [26]. The change in the tensile strength of concrete is much lower than that of the compressive strength. Conversely, the Young's modulus decreases significantly with the increase in the temperature [26]. Along with the increase in the

atomic thermal variations, the volume expansion will occur in concrete when the temperature increases, thereby changing the Young's modulus [28]. In addition, the effect of temperature on the properties of the steel materials was mentioned in the literature [29,30]. Because the temperature-induced change in the material properties is complex, which is not of concern in this study, the primary focus in this section is on the effect of the temperature on the Young's modulus of concrete, which leads to a variation in the natural frequency. Xia et al. [8] showed that the effects of the friction at the supports and the geometric change due to the temperature variation in the vibrational frequency were much lower than that of the temperature-induced variation in the Young's modulus. Hence, the numerical analyses were extensively validated against the measured changes in the natural frequencies of the PC girders due to the ambient temperature were conducted using FE commercial software. In this test, the 3D model of FX+ for DIANA described previously was used for the simulation. In this approach, a linear equation was employed wherein the Young's modulus of concrete is considered a function of the temperature. At each measurement, the Young's modulus with respect to the temperature was calculated and inputted to the DIANA model to obtain the modal parameters. The effect of temperature at the time of testing on the Young's modulus of concrete, at an age of 28 d without the exchange of moisture, can be obtained using **Eq. (4.12)** [31] as follows.

$$E_{ci}(T) = E_{ci}\left(1.06 - \frac{0.003T}{T_0}\right), \tag{4.12}$$

where $T$ is the temperature of the material (ºC), $E_{ci}$ is the Young's modulus of concrete at 20 ºC, $E_{ci}(T)$ is the Young's modulus of concrete at temperature $T$ ºC, and $T_0$ = 1 ºC. The previous results show that girder No.3 exhibited much lower levels of damage due to the ASR compared to the other two girders. The presence of a few cracks only slightly affected the vibrational responses because the correlation levels with the ambient temperature were clearly high for the three modal frequencies considered in this study. Therefore, the measured frequencies of girder No.3 were employed as a comparison with the simulation results. The Young's modulus of concrete at 20 ºC was assumed as 38700 $\mathrm{N/mm^2}$, which was obtained from the compression tests conducted on concrete cores collected from the middle section of girder No.3 along the direction perpendicular to the girder axis. **Table 4.13** lists the analytical results of the two bending modal frequencies of girder No.3. From this table, it is found that the numerical model yielded relatively similar values compared to the measurement. Therefore, the FE model can be calibrated to more closely match the experimental frequencies and provide more accurate predictions of the frequency in the future. There is a slight difference between the measurements and the analysis results because the Young's moduli used in the numerical analysis might not reflect the real moduli of the entire girder, particularly because the girder is PC. The results of the coring test [32] showed that the mechanical properties of the concrete cores varied based on their collecting positions and directions. In particular, because of the

effect of the restraining stress of the PC strands along with the low expansion rate of concrete, the concrete samples collected longitudinally from the central part exhibited lower compressive strengths compared to the samples collected from the transverse direction. When comparing the results obtained for the central and the end parts, the mechanical properties of the concrete cores of the end part are poorer than those of the central part. In addition, the ambient temperature, which was used as an input in the governing linear equation, did not significantly change the temperature of the girder instantaneously because of its large thermal mass. Therefore, the inputted temperature profile might not accurately reflect the temperature of the girder. Because the main objective of the simulations was to confirm the relationship between the frequency variation and the temperature-induced change in terms of the Young's modulus, the frequencies were normalized by the highest frequency in the monitoring period. **Figures 4.21(a) and 4.21(b)** show the variations in the relative vibrational frequencies of the two bending modes of girder No.3 with respect to time. The figures show that the trend in the frequency variation in both the experimental and analytical results with respect to the temperature is similar. Negative relationships between the frequencies and the ambient temperature were obtained in the results: the temperature increased with the decreases in the frequencies. In addition, both the relative frequencies followed an expected trend. In other words, they increased and reached the maximum values in March 2016 when the measured ambient temperature was the lowest over the monitoring period, and subsequently, decreased until September 2016. In particular, the temperature varied by ~21.55 ºC from approximately ~33 ºC in May 2015 to ~11.45 ºC in March 2016 (between summer and winter). This decrease led to a variation in the Young's modulus of concrete, thereby increasing the analytical frequency of mode 1 by ~3.1%. This rate was obtained at ~4.5% with respect to the measurement. The measured temperature then increased gradually by ~19 ºC from a low temperature to ~30.45 ºC in September 2016 (between winter and summer). Consequently, the experimental and analytical frequencies decreased by ~2.8 and ~2.7%, respectively. To make a consistent comparison with the other girders, this study assumed that the analytical frequencies of girders No.1 and No.2 varied linearly with the variation in the ambient temperature. Based on this assumption, the variation ratios of the analytical frequencies with respect to time of the girders No.1 and No.2 were estimated and plotted in **Figs. 4.22(a), 4.22(b), 4.23(a) and 4.23(b)**, respectively. As shown in these figures, the variations in the numerical frequencies are not in agreement with the changes in the measured one. In particular, the second bending mode of girder No.2, which is shown in **Fig. 4.23(b)**, exhibited a higher discrepancy compared to the other results. This noise is likely because of the ASR-induced deteriorations because many longitudinal cracks were observed on the top, bottom, and both side surfaces of the girders No.1 and No.2 whereas girder No.3 suffered only a few. In addition, it is difficult to estimate the higher order modes with precise accuracy. The results of the torsional modes were not shown because they were not identified with sufficient precision to

detect the environmental effects. These obstacles were reported in other studies as well [8,15,18]. The results of the extensive validations show that the correlation between the variations in the natural frequencies and the temperature-induced changes in the Young's modulus could be proved reasonably using the FE model developed in this study.

*Table 4.13 Numerical analysis and measured results of two bending modal frequencies.*

| Time | Average temperature | Young's modulus | Bending 1st mode | | Bending 2nd mode | |
|---|---|---|---|---|---|---|
| | | | Experiment | Analysis | Experiment | Analysis |
| Month | $^0$C | N/mm$^2$ | Hz | Hz | Hz | Hz |
| 25-May-15 | 33.00 | 37191 | 9.593 | 9.576 | 34.506 | 37.054 |
| 09-Jul-15 | 23.40 | 38305 | 9.822 | 9.713 | 35.453 | 37.583 |
| 18-Aug-15 | 27.40 | 37841 | 9.874 | 9.656 | 35.261 | 37.363 |
| 03-Nov-15 | 17.25 | 39019 | 9.981 | 9.799 | 35.787 | 37.918 |
| 16-Mar-16 | 11.45 | 39693 | 10.041 | 9.880 | 36.266 | 38.231 |
| 23-May-16 | 22.38 | 38424 | 9.855 | 9.727 | 35.112 | 37.639 |
| 21-Jul-16 | 26.75 | 37916 | 9.826 | 9.665 | 34.957 | 37.399 |
| 02-Sep-16 | 30.45 | 37487 | 9.759 | 9.613 | 34.385 | 37.195 |

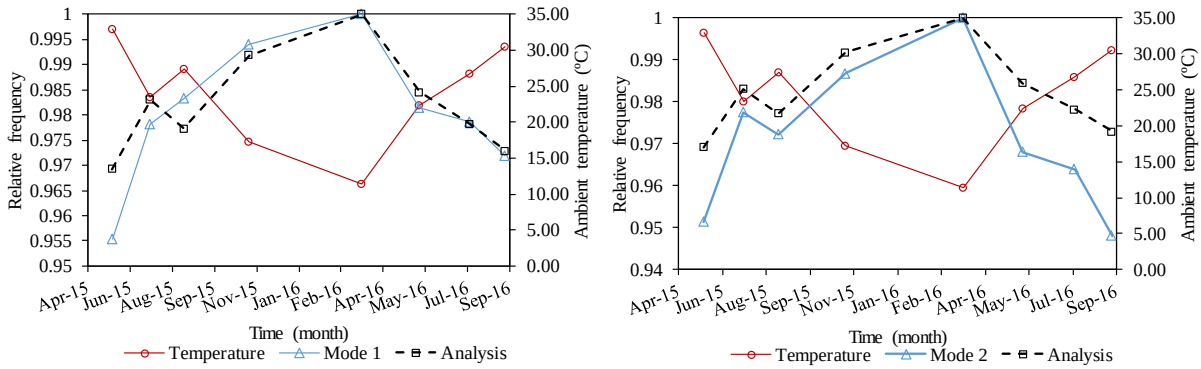


(a) The 1st bending mode (mode 1) (b) The 2nd bending mode (mode 2)

*Figure 4.21 Variations in two bending modal frequencies of girder No.3 over one and a half year.*

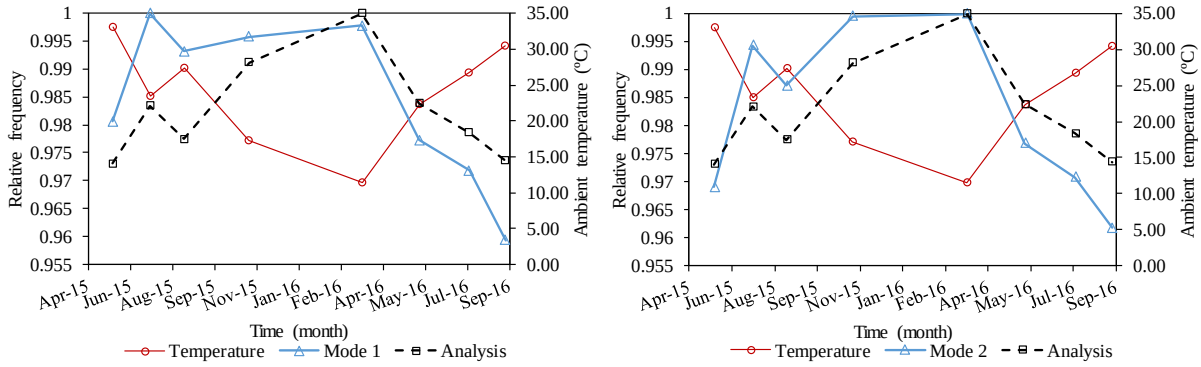


(a) The 1st bending mode (mode 1) (b) The 2nd bending mode (mode 2)

*Figure 4.22 Variations in two bending modal frequencies of girder No.1 over one and a half year.*

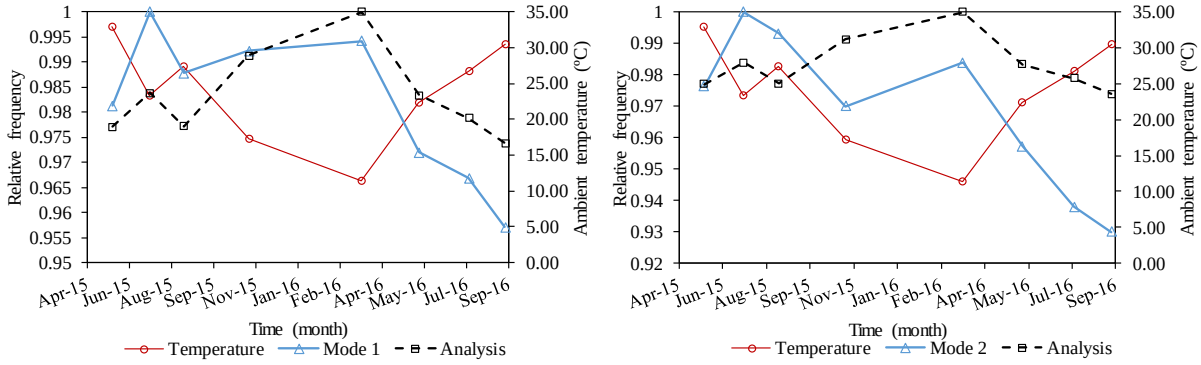


(a) The 1st bending mode (mode 1) (b) The 2nd bending mode (mode 2)

*Figure 4.23 Variations in two bending modal frequencies of girder No.2 over one and a half year.*

## 4.5 Conclusions

In this study, the combined effect of the changes in the environmental conditions and the ASR-induced deteriorations on the three PC girders with non-identical mixtures was monitored for one and a half years. The main conclusions drawn from this study are as follows.

- ✓ The environmental conditions strongly affected the changes in the frequencies of the vibration modes of the girders because the correlation coefficients between the variables were strong, as computed using the linear models. With regard to the relationship with the ambient temperature, the amplitude of the vibrational frequency decreased with respect to the increase in the ambient temperature. The correlation levels were comparatively moderate for girders No.1 and No.2 but fairly strong for girder No.3. With regard to the effect of humidity, relatively negative relationships between the measured frequencies and humidity were obtained. The ambient humidity affected the frequencies of the bending modes of girders No.1 and No.2 more significantly than those of girder No.3. This observation can be attributed to the influence of the ASR-

induced cracks because water could be absorbed and dispersed easily in girders No.1 and No.2. The results of the error analysis show that the bending modes could be estimated more accurately than the torsional mode because the error ratio of the torsional mode was higher than that of the bending modes.

- ✓ The effects of the measured humidity and temperature on the changes in the damping ratio were negligible, though some outcomes illustrate that the damping ratios decreased relatively with the increase in the environmental parameters. Moreover, because the identified measurement noises were rather high, it was concluded that the damping ratios were not determined with sufficient accuracy to distinguish the environmental impacts.
- ✓ A significant number of scatters can be seen in all the estimated MAC values with no notable pattern reflecting the variation in the amplitude with respect to the ambient temperature and humidity. The results proved that the ambient temperature and humidity affected the entire girder uniformly, and consequently, the effects of the environmental conditions on the MAC values were not meaningful.
- ✓ The outcomes of the comparison between the three girders show that the differences in the measured frequencies of the three girders manifested clearly over time in terms of the two bending modes, whereas no significant deviation was observed for the frequencies of the torsional mode. In particular, the bending frequencies of girder No.3 were higher than those of girders No.1 and No.2 at each measuring time. With regard to the damping ratio, similar observations were made. Although no significant difference in the amplitude of the torsional mode was obtained, the damping ratios of the other modes changed considerably. Within one and a half years of investigation, the damping ratio of girder No.3 was found to be lower than that of the other girders. The analysis of the MAC values shows that there is no clear discrepancy in the magnitude of the MAC values considered in this study.
- ✓ During the monitoring period, the bending modal frequencies of girder No.3 fluctuated in the range of ~3–5%, which is considerable compared to those due to structural damage. Hence, the effects of the environmental conditions should be examined thoroughly when using the variation in the vibrational frequency to assess the health of structures.
- ✓ Because the dynamic behaviors of the three girders were clearly observed to be different, the fly ash significantly affected the performances of the PC girders under the ASR damage.

## 4.6 References

[1] O. Huth, G. Feltrin, J. Maeck, N. Kilic, and M. Motavalli, "Damage Identification Using Modal Data: Experiences on a Prestressed Concrete Bridge," *J. Struct. Eng.*, vol. 131, no. 12, pp. 1898–1910, 2005.

[2] S. Hassiotis and G. D. Jeong, "Identification of Stiffness Reductions Using Natural Frequencies," *J. Eng. Mech.*, vol. 121, no. 10, pp. 1106–1113, 1995.

[3] Y. Xia, H. Hao, J. M. W. Brownjohn, and P. Q. Xia, "Damage identification of structures with uncertain frequency and mode shape data," *Earthq. Eng. Struct. Dyn.*, vol. 31, no. 5, pp. 1053–1066, 2002.

[4] Z. Y. Shi, S. S. Law, and L. M. Zhang, "Damage Localization by Directly Using Incomplete Mode Shapes," *J. Eng. Mech.*, vol. 126, no. 6, pp. 656–660, 2000.

[5] A. K. Pandey, M. Biswas, and M. M. Samman, "Damage detection from changes in curvature mode shapes," *J. Sound Vib.*, vol. 145, no. 2, pp. 321–332, 1991.

[6] A. K. Pandey and M. Biswas, "Damage Detection in Structures Using Changes in Flexibility," *J. Sound Vib.*, vol. 169, no. 1, pp. 3–17, 1994.

[7] L. M. Z. Z. Y. Shi, S. S. Law, "Improved Damage Quantification from Elemental Modal Strain Energy Change," *J. Eng. Mech.*, vol. 128, no. 5, pp. 521–529, 2002.

[8] Y. Xia, H. Hao, G. Zanardo, and A. Deeks, "Long term vibration monitoring of an RC slab: Temperature and humidity effect," *Eng. Struct.*, vol. 28, no. 3, pp. 441–452, 2006.

[9] J. H. G. Macdonald and W. E. Daniell, "Variation of modal parameters of a cable-stayed bridge identified from ambient vibration measurements and FE modelling," *Eng. Struct.*, vol. 27, no. 13, pp. 1916–1930, 2005.

[10] Z.-D. Xu and Z. Wu, "Simulation of the Effect of Temperature Variation on Damage Detection in a Long-span Cable-stayed Bridge," *Struct. Heal. Monit.*, vol. 6, no. 3, pp. 177–189, 2007.

[11] J. T. Kim, J. H. Park, and B. J. Lee, "Vibration-based damage monitoring in model plate-girder bridges under uncertain temperature conditions," *Eng. Struct.*, vol. 29, no. 7, pp. 1354–1365, 2007.

[12] P. Cornwell, C. R. Farrar, S. W. Doebling, and H. Sohn, "ENVIRONMENTAL VARIABILITY OF MODAL PROPERTIES," *Exp. Tech.*, vol. 23, no. 6, pp. 45–48, 1999.

[13] B. Peeters and G. De Roeck, "One-year monitoring of the Z24-bridge: Environmental effects versus damage events," *Earthq. Eng. Struct. Dyn.*, vol. 30, no. 2, pp. 149–171, 2001.

[14] T. M. Ha, S. Fukada, N. Arima, N. Moriyama, and T. Miyashita, "Study on vibration and structural performance of PC Girder removed due to salt damage," in *Proceedings of 14th East Asia-Pacific Conference on Structural Engineering and Construction*, 2016,

pp. 680–681.

[15] Y. Xia, Y. L. Xu, Z. L. Wei, H. P. Zhu, and X. Q. Zhou, "Variation of structural vibration characteristics versus non-uniform temperature distribution," *Eng. Struct.*, vol. 33, no. 1, pp. 146–153, 2011.

[16] J. N. Juang and R. S. Pappa, "An eigensystem realization algorithm for modal parameter identification and model reduction," *J. Guid. Control. Dyn.*, vol. 8, no. 5, pp. 620–627, 1985.

[17] The R Manuals, "The R Manuals." [Online]. Available: https://cran.r-project.org/manuals.html. [Accessed: 20-Jul-2004].

[18] P. Moser and B. Moaveni, "Environmental effects on the identified natural frequencies of the Dowling Hall Footbridge," *Mech. Syst. Signal Process.*, vol. 25, no. 7, pp. 2336–2357, 2011.

[19] N. Sugiura, K. Kobayashi, S. Fukada, and K. Torii, "Diagnosis the ASR deterioration of the prestressed concrete girder by cylinder cores," in *Proceedings of the JCI annual convention*, 2017.

[20] A. D. Dimarogonas, "Vibration of cracked structures: A state of the art review," *Engineering Fracture Mechanics*, vol. 55, no. 5. pp. 831–857, 1996.

[21] M. Rezaee and H. Fekrmandi, "A theoretical and experimental investigation on free vibration behavior of a cantilever beam with a breathing crack," *Shock Vib.*, vol. 19, no. 2, pp. 175–186, 2012.

[22] A. P. Bovsunovskii, "Numerical study of vibrations of a nonlinear mechanical system simulating a cracked body," *Strength Mater.*, vol. 31, no. 6, pp. 571–581, 1999.

[23] R. O. Curadelli, J. D. Riera, D. Ambrosini, and M. G. Amani, "Damage detection by means of structural damping identification," *Eng. Struct.*, vol. 30, no. 12, pp. 3497–3504, 2008.

[24] D. J. Ewins, *"Modal Testing: Theory, Practice and application."* 2000.

[25] Tnodiana.com, "User's manual of FX+ for DIANA version 9.6." [Online]. Available: https://support.tnodiana.com/manuals/d96/Diana.html. [Accessed: 01-Jul-2016].

[26] V. K. R. Kodur, "Properties of Concrete at Elevated Temperatures," *ISRN Civ. Eng.*, vol. 2014, pp. 1–15, 2014.

[27] P. J. Barr, J. F. Stanton, and M. O. Eberhard, "Effects of Temperature Variations on Precast, Prestressed Concrete Bridge Girders," *J. Bridg. Eng.*, vol. 10, no. April, pp. 186–194, 2005.

[28] W. Li, R. Wang, D. Li, and D. Fang, "A model of temperature-dependent Young's modulus for ultrahigh temperature ceramics," *Phys. Res. Int.*, 2011.

[29] European Committee for Standardization, "Design of concrete structures - Part 1-2: General rules - Structural fire design," *Eurocode 2*, vol. BS EN 1992, p. 97, 2004.

[30] V. K. R. Kodur and T. Z. Harmathy, "Properties of building materials," in *SFPE Handbook of Fire Protection Engineering, Fifth Edition*, 2016, pp. 277–324.

[31] C. CEB-FIP, "Model Code 1993," *Com. Euro-International Du Beton, Paris*, pp. 87–109, 1993.

[32] S. Fukada, T. M. Ha, K. Kobayashi, and K. Torii, "Influence on load carrying capacity of PC girder using reactive aggregate by fly ash," *Proc. Japan Concr. Inst.*, vol. 39, no. 2, pp. 355–360, 2017.

# Chapter | 5

# Long-Term Monitoring of the Variation in Temperature-Induced Camber of PC Girders with and without Fly Ash Considering ASR Deterioration

## 5.1 Introduction

### 5.1.1 Significance of the study

A bridge is a construction that is exposed during its lifetime to fluctuating weather conditions. Bridge temperature is, therefore, changing regularly. Materials, and thus also a superstructure, will expand when heated, and contracts when cooled. This thermal movement is together with deformation caused by shrinkage, the primary factor for the overall displacement of a superstructure. In conventional bridges, movement of the superstructure is accommodated with expansion joints. The bridge deck can then expand and contract freely. In integral bridges, the lack of expansion joints causes the movement to act on the bridge ends, freely displacing the abutments. The piles and approach fill are subjected to lateral loading and unloading, as the abutments are pushed and pulled away due to expansion and contraction. There will be repeating cycles of expansion and contraction throughout the bridge lifetime. Some trouble has been attributed to temperature variations within the structures [1,2]. In the main bridges, sudden displacement of ±50 mm has been recorded that has to be attributed to restoring forces of bearings being suddenly released [3]. This movement usually is within the normal limits of allowable displacement, but the sudden reaction might trigger unforeseen problems, such as restraints in the expansion joint. The frequency of such a phenomenon is not yet sufficiently documented, but in a 6-month record of a major steel bridge, three such occasions have been detected. Moreover, if the girders have too much camber or deflection, the driving surface will be rough and unpleasant for motorists using the bridge. Also, a downward deflection creates an aesthetically displeasing bridge for the public. Therefore, thermal actions on civil engineering structures due to climatic and operational temperature changes need to be considered in the design where there is a probability of the ultimate or serviceability limit state being exceeded due to thermal movement or stresses.

Camber [4] due to temperature gradients, also referred to as curling [5], is a well-documented behavior in many concrete elements. Curling has been studied in concrete pavements [6–8], prestressed concrete bridge girders [4,9,10], concrete slab track [11–13] and concrete crosstie [5]. A results of Wolf et al. [5] on concrete crossties showed that the variation in the shape of a curled crosstie could lead to significant changes (capable of causing negative center cracking) in the bending moments encountered by concrete crossties in service. Specifically, center negative bending moments were observed change to by up to 50% under variations in the temperature gradient of less than 30 ºF (16.7 ºC). The outcomes of numerical approach revealed that curl in concrete crossties could be related to the temperature gradient and the analytical or empirical methods allowed curl to be approximated utilizing only temperature data. Regarding concrete bridge girders, a comprehensive report by Imbsen et al. [9] gathered the results of many research projects on thermal gradients on concrete bridge superstructures. The report analyzed the design practices used in different states and countries to account for temperature gradients. Moreover, they indicated two ways in which temperature variation can produce stresses in concrete: temperature-caused distortions can induce internal bending moments when restrained, and nonlinear temperature gradients are prevented from generating nonlinear distortion as plane sections remain plane [9]. A study on standard prestressed, precast concrete I-beam shapes measured the temperature gradient and the deflection at midspan due to these gradients [4]. This temperature-caused deflection can lead to challenges in construction and induce stress in the superstructure. Also, the midspan vertical deflections and transverse temperature distributions were monitored for a segmental prestressed box girder bridge at the Pennsylvania Transportation Research Facility by Hoffman et al. [14] for 18 diurnal (daily) cycles during the period starting on October 25, 1978, and ending on October 16, 1979. The test bridge consisted of two curved, superelevated, prestressed box girders, each composed of 17 segments. From their results, the maximum upward deflection, 0.72 in. (18.29 mm), occurred on July 7, 1979, and the maximum downward deflection, 0.11 in. (2.79 mm), occurred on January 4, 1979. The thermal conditions on July 7, 1979, included a maximum air temperature of 86 ºF (30.0 ºC), a minimum temperature 64°F (17.8 ºC), a 24-hour wind movement of 60 miles (97 km) with no prevailing direction, a clear to hazy sky condition, and a cumulative solar radiation of 660.2 Langleys. On January 4, 1979, the weather was completely the opposite, with a temperature range of+12 to –2 ºF (-11.1 to 25.1 ºC), a 24-hour wind movement of 208 miles (1098 km) from the west, the presence of snow flurries, and a cumulative solar radiation of 122.9 Langleys.

In 2001, Usmani et al. [15] attempted to lay down some of the most important and fundamental principles that govern the behavior of composite frame structures in a fire in a straightforward and comprehensible manner. Basic principles introduced in the paper provide a method of estimating forces and displacements in real structures with appropriate idealizations. Such

estimates can be of considerable advantage in evaluating the results from more rigorous numerical analyses, or they can be employed for design calculations. In 2005, Barr et al. [4] summarized observations, during both fabrication and service, of temperature variations and their effects (e.g., changes in stresses, strains, and cambers) for a typical precast, prestressed concrete girder bridge. For their study, a new three-span bridge, which had span lengths of 24.4, 41.7, and 24.4 m, was instrumented during fabrication and monitored for three years while the bridge was in service [16]. The cast-in-place roadway deck was 190 mm thick, had a width of 11.6 m, and was supported by five lines of Washington State W74MG girders. Besides, a 20-ft long, statically determinate girder, designated the "test girder," was cast at the same time as the bridge girders and with the same cross section and materials. The measured values were obtained from the automated stretched-wire systems [17]. As the results, the camber changed during the day by 15 to 20 mm (0.6 to 0.8 in.). These variations in deflection were significant because they were almost equal to two-thirds of the deflection induced by casting the deck. Six years later, Debbarma and Saha [18] presented the effects caused in real structures due to development of strain on account of creep, shrinkage and atmospheric temperature by using the field data's collected from two PSC box girder bridges. Their results showed that the vertical deflection of pre-stressed concrete girders due to a loss in pre-stress was a natural phenomenon. In addition to this, it was observed that due to creep, shrinkage and daily atmospheric temperature variation in structural concrete there was a long-term deflection in pre-stressed concrete girders. These causes decreased in the service life of the bridge and, it required strengthening method such as external pre-stressing to secure its original load bearing capacity for the long term usage. In 2012, Lee and Kalkan [19] carried out a one-year experimental and analytical study on a prestressed concrete BT-1600 girder segment to examine both the vertical and lateral thermal gradients with changes in environmental condition. By using two-dimensional (2D) finite element heat transfer analysis, sensitivity analyses were performed to propose analytical equations that predict the vertical and lateral temperature differentials from daily climatic information provided by weather stations. The predicted temperature differentials agreed well with the measured values. Then, thermal deformations caused by the vertical and lateral thermal gradients were estimated using an analytical approach acquired from one-dimensional beam theory. In 2015, E.H. El-Tayeb et al. [20] studied the behavior of reinforced concrete beams and frames under thermal loads, with the presence of dead and live loads, to examine the effect of temperature variation. The beams and frames were modeled correctly by accounting for material nonlinearity, particularly cracking. Different temperature gradients, uniform, linear and nonlinear, were considered. The obtained results of the studied cases revealed that material modeling of reinforced concrete beams and frames played a vital role in how these structures react to temperature variation. Moreover, cracking contributed to the release of a significant portion of temperature restraint, which was almost omitted in some cases.

### 5.1.2 Factors affect the temperature profile of civil engineering structures

The parameters to be considered in the definition of bridge design temperatures can be classified into the following groups [21]:

- ✓ Climatic: solar radiation, air temperature, wind speed, nebulosity, etc.
- ✓ Geographical: altitude, latitude, etc.
- ✓ Time: hour of the day, day of the year, etc.
- ✓ Geometric: geometry of the cross section, bridge orientation, asphalt thickness, etc.
- ✓ Materials: thermal conductivity, density, specific heat, color, etc.

The first three categories are related to the environmental features of the location in which the bridge is located. The final two parameters are correlated to bridge components. Bridge characteristics relate in how the structure will respond to variations in weather conditions. A bridge with a slender open design will adapt more quickly to changes in temperature compared to a non-slender bridge with less exposed surfaces [22]. Regarding climatic parameters, the diurnal temperature usually relates to the shift in temperature from the daytime high to the night-time low. The daily temperature is measured by meteorological institutions around the world in a standardized way, which guarantees that the determined temperature is not altered by solar radiation, wind speed, precipitation. Diurnal temperature is also regarded as shade air temperature. Besides, annual seasonal air temperature variations may be as significant as 50 ºC (depends on local climate) [23]. Since temperature is the most notable of these factors [5,22], this study attempts to analyze the effects of ambient temperature on the change in upward displacement of prestressed concrete (PC) girders.

### 5.1.3 Daily and seasonal temperature change

The ambient temperature not only differs from season to season but also throughout any given day (diurnal cycle) [14]. As the sun rises and goes down in an endless cycle, so does the daily temperature fluctuate, and with it a continuous phase of contraction and expansion of the superstructure. This sequence of temperature variation happens every day and thereby be considered as the daily temperature variation. The seasonal temperature variation corresponds to the maximum mean temperature change expected to occur during the year. Therefore, the most considerable expansion of the superstructure will occur on summer days, while the most significant contraction will occur on winter nights [25]. These extreme temperature fluctuations induce the largest temperature related displacements.

For example, an extensive field study on two integral bridges – the Maple River bridge (composite) and the Boone River bridge (concrete) – in Iowa was performed by Girton et al. [26] in 1991. Both bridges were monitored for two years, from January 1987 to January 1989.

As the outcome, the mean temperature changed throughout the year in an annual cycle. This seasonal temperature change consisted of a period of high amplitude and low frequency, while the daily temperature vibrated around the mean temperature with a small amplitude and high frequency. In addition, there was a linear connection between temperature and thermal displacement and the temperature-induced displacement also resulted in a cyclic tendency. Hallmark [27] refers to a study of Russel and Gerken [28], in which they note that the annual temperature variations mainly affect the thermal displacement of the superstructure, while the daily fluctuations primarily affect the vertical temperature gradient. Therefore, in many cases can daily changes be ignored, as daily temperature displacements are small when compared to movements caused by seasonal temperature change.

### 5.1.4 Temperature distribution models

The aim of the following analysis is to review temperature related stresses according to the Euro code. Daily and seasonal variations in shade air temperature, solar radiation, re-radiation will lead to changes in the temperature distribution within individual components of a structure. Furthermore, volume differences and/or stresses due to temperature variations might be affected by shading of adjacent buildings, the performance of different materials with non-identical thermal expansion coefficients and heat transfer, use of various shapes of the cross-section with various uniform temperature [29]. The temperature distribution within an individual structural element can be split into primary components: a uniform temperature component; linear temperature difference components; a nonlinear temperature difference component (also referred to as Eigen-temperature component [22]). This results in a system of self-equilibrated stresses which produce no net load effect on the element [29].

The uniform temperature component is primarily responsible for the expansion and contraction of a bridge. This component governs longitudinal movement. A change in the average temperature will result in a change of length, as the material expands or shrink, as showed **Fig. 5.1**.


*Figure 5.1 Longitudinal displacement due to uniform temperature deviation from the reference- and the construction-temperature "$T_0$"*

The linear temperature components are responsible for curvature or rotation at the abutments (see **Fig 5.2**). Moreover, bending stresses will develop in the superstructure if the acting curvature, caused due to a linear temperature distribution, is hindered. The Eigen-temperature component shows no deformation, except for possible warping at the ends.

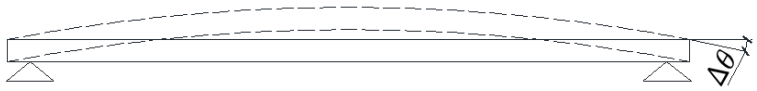


*Figure 5.2 Curvature of a beam due to a linear temperature component.*

The thermal-induced displacement does not generate stresses by itself unless movement is restrained. When movement is controlled, stresses are produced within a structure opposite to the direction of displacement. The expansion and shortening will induce compression- and tensile-stresses, respectively. These thermal-induced stresses can cause deterioration to the structure when it is not adequately planned to withstand these stresses.

### 5.1.5 Thermal-induced stresses

**(1) Average temperature**

As mentioned above, a change in the average temperature of a bridge will induce a global increase or decrease in volume of an element. In the case of a bridge girder, which can be represented as an element in which length governs width and thickness, the most significant deformation and problems associated with this deformation will be longitudinal. To define thermal induced strains, a reference point is needed [22]. The reference temperature for a girder was the temperature when it was installed or made. If the girder was produced continuous with a construction temperature of $T_0$, then every value above or under this reference temperature will cause expansion or contraction respectively. In other words, an element subjected to a temperature change of $\Delta T$ will vary in length by an increment $\Delta L$ if the movement is unhindered. The proportion of this increase depends on the thermal coefficient $\alpha$ and the thermal length of the element $L$. **Equation (5.1)** shows that the variation in length is directly proportional to the change in uniform temperature.

$$\Delta L = \alpha \times \Delta T \times L, \tag{5.1}$$

Since the structure cannot move freely in many practical cases, stresses will thereby occur within the girder. These stresses are dependent on the stiffness of the concrete $E_c$, the linear expansion coefficient $\alpha$, and the temperature difference $\Delta T$. Assuming that movement is completely constrained, these axial stresses can be determined by the following formula:

$$\sigma_{\Delta T} = \alpha \times \Delta T \times E_c, \tag{5.2}$$

**Equations (5.1) and (5.2)** show that while thermal displacement increase with increased length, thermal stresses remain the same. Thermal stresses are not dependent on dimensions of the girder or total construction length [22]. Consequently, if there is no change in the dimensions of the girder and the movement is completely restrained, the reactionary force needed to prevent displacement remains the same even if total thermal length triples.

$$F_{\Delta T} = \alpha \times \Delta T \times E_c \times A, \quad (5.3)$$

where, $\alpha=1.0\times10^{-5}(1/℃)$ is the linear expansion coefficient for concrete, $E_c$ (N/mm$^2$) stands for Young modulus for concrete, and $\Delta T = T\text{-}T_0$ (ºC) is the temperature difference.

**(2) Linear temperature**

An element will be subjected to a temperature-induced camber if there is a linear temperature profile over its height. Because heat penetration in a concrete element is limited in a relatively short period, stress at the outer fibers is mostly dependent on the profile height, which decreases as profile height increase. Therefore, the percentage of total area affected by a rapid variation in temperature will decrease as profile height ($h$) increase. For h ≥ 1.0 m and fck ≥ 50 N/mm$^2$, the linear moment caused by a rapid change of temperature only amounts to 5% of the cracking moment of a rectangular element [22]. Therefore, linear temperature according to the Euro code model can be considered negligible for large profiles, whereas it should still not just be ignored, especially for relatively small profile heights. **Figure 5.3(a)–(c)** shows a girder element is subjected to temperature gradient $\Delta T$ over its height.

$$\Delta T = T_t - T_b, \quad (5.4)$$

where $T_t$ and $T_b$ are temperature at the top and bottom of the girder.


(a) The girder under temperature gradient

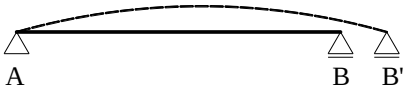


(b) Deflection of girder owing to temperature gradient

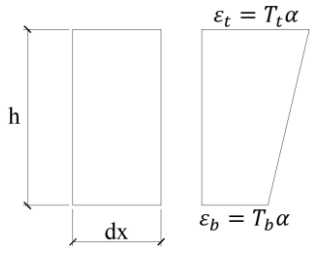


(c) Strain diagram

*Figure 5.3 A girder under linear temperature distribution.*

The deflection of the girder due to temperature variation is shown in **Fig. 5.3(b)**. It is assumed that temperature varies linearly through the height $h$, and $\alpha$ is the coefficient of thermal expansion of the material. Consider a small element of length $dx$. The strain at top and bottom of the small elements are

$$\varepsilon_t = \frac{T_t \alpha dx}{dx} = T_t \alpha \tag{5.5}$$

$$\varepsilon_b = \frac{T_b \alpha dx}{dx} = T_b \alpha \tag{5.6}$$

The curvature of the beam is given by

$$\frac{1}{\rho} = \frac{\varepsilon_m}{h} = \frac{\alpha(T_t - T_b)}{h} \tag{5.7}$$

$$\frac{d^2v}{dx^2} = \frac{\alpha(T_t - T_b)}{h} \tag{5.8}$$

**Equation (5.8)** can be used for finding out the bending deflection in beams due to temperature variation. If the beam is restrained from rotation, the moment induced in the beam will be given by

$$M_T = \frac{EI\alpha(T_t - T_b)}{h} \tag{5.9}$$

**Equation (5.9)** is obtained by equating the right hand side of **Eq. (5.8)** to $\frac{M_T}{EI}$ from the simple bending theory.

### 5.1.6 Objectives of this study

This study investigates the effects of environmental conditions on the static responses of prestressed concrete (PC) girders, which were affected by varying degrees of deteriorations induced by an alkali–silica reaction (ASR). Because the environmental conditions might cause complicated structural responses, the objective of this portion of the study was to monitor the long-term camber behavior at midspan of full-scale PC girder affected by ASR considering fluctuations due to change in ambient temperature gradient. This study focused on two concrete JIS A5373-AS09 girders, which were girders No. 1 and No. 3 in the previous chapters. In particular, girder No. 1 was affected by the ASR while girder No.3 was kept at an inactive state by suppressing the acceleration of the ASR using the fly ash. Girder cambers, and air temperatures were periodically monitored in one and a half years. The obtained data were then analyzed using linear regression models concerning the variations in measured ambient temperature. Moreover, the measured cambers were compared to predicted values obtained using finite element analysis procedures and trend line (empirical-linear). The finite element method was employed for conducting the analysis utilizing the computer code DIANA. This study presents preliminary considerations for estimating the long-term displacement behavior of PC girders and attempts to proposed recommendations about measurement noise when using static responses as input for structural damage detection.

## 5.2 Experimental procedure

Laboratory experimentation was performed to quantify actual camber magnitudes. Three simply supported PC girders were placed outside the laboratory, exposed to outdoor weather conditions, one of which had a selected amount of fly ash in its mixture to mitigate the ASR. The length and height of each girder were 9600 and 450 mm, respectively. The upper and lower edge widths of the cross-section of each girder were 640 and 700 mm, respectively. The present study reports the camber behaviors of girders No.1 and No.3. **Figure 5.4** shows a graphic of the laboratory set-up used to investigate this upward movement. To obtain the static responses, especially temperature-induced displacements, seven displacement meters were mounted at different points under the girder with a constant interval of 1.15 m, as shown in **Fig. 5.5**. Moreover, the ambient temperature was recorded simultaneously during the test using a thermometer. To track the variation in camber owing to diurnal temperature, the signal was collected once automatically from the sensor every 30 minutes, 24 hours an observation day. In addition, to track the variation concerning seasonal changes, seven measurements were performed from October 2015 to September 2016 in Kakuma campus with 14762 valid sets of data.


*Figure 5.4 Measured point layout under the PC girder (Unit: mm)*

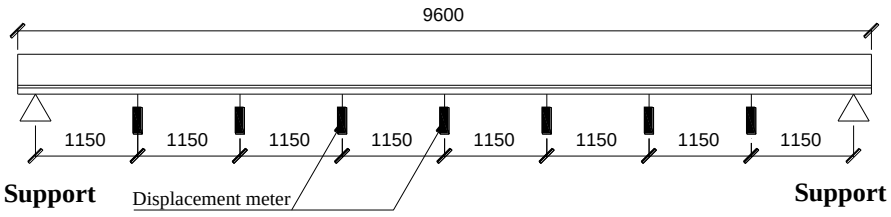


*Figure 5.5 Experiment layout.*

## 5.3 Observed behavior

This section provides observation results of camber variations of girders No. 3 and No. 1 throughout the monitoring period. Ambient temperature was collected in addition to the vertical displacement of the girders. A direct relationship between the movement at midspan and the

ambient temperature is evident in the data (**Fig. 5.6(a)–(g)**); as the ambient temperature increases, so does camber. In these figures, the initial signal obtained from the sensor at each period of monitoring was utilized as the reference line for the camber estimation. The measured temperature followed an expected cycle, increasing and reaching its maximum positive value in the mid-afternoon, then dropping down to a relatively constant maximum negative value in the early morning hours. The camber of both girders also followed the similar trend. The daily repetition of the same deflection pattern in the girders might lead to the formation of mini cracks and further deterioration [18]. However, the temperature change saw some noise within certain short period at high positive and negative value. This noise is likely caused by intermittent cloud cover or wind throughout the day. Moreover, this noise did not significantly affect the camber of the girder instantaneously because of the large thermal mass of the girder.

The downward deflection pattern of girders No.1 and No.3 as obtained at different measurements of a day is shown in **Figs. 5.7(a) and 5.7(b)**, respectively. In these figures, the illustrated data were collected every 30 minutes when the ambient temperature decreased by 8.1 ºC from 32.4 ºC at 2:30 pm on September 1st 2016 to 24.3 ºC at 5:40 am on September 2nd 2016. From the plotted figures, it can be observed that, on account of temperature decrease, there was a development of downward movement in both girders. This result can be attributed to the fact that the top of the girder releases heat and cools faster in the evening, causing a linear temperature gradient and tensile stresses on the bottom side.

Besides, seasonal changes in camber were well confirmed in **Figs. 5.6(a)–(g), and 5.8(a)–(d)**. From the measured data, the displacement at midspan fluctuated in the broader range on summer days (July and August) as compared to the results obtained in the low-temperature months such as March and April. Specifically, the variation range was estimated to be under ~2.5 mm for both girders in October 2015 and March 2016. This value was obtained as around 5 mm in July and August 2016. Therefore, there was a positive correlation between camber and ambient temperature, in which the displacement of the girder increased with the rise in ambient temperature and decreased as the temperature drops down.

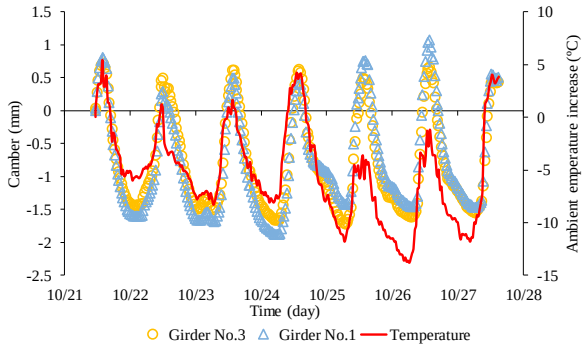


(a) 21st ~ 27th October 2015

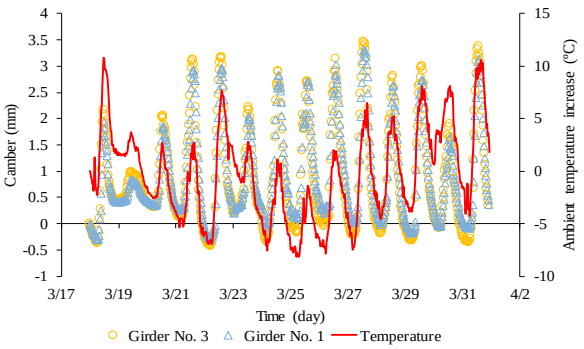


(b) 18th ~ 31st March 2016

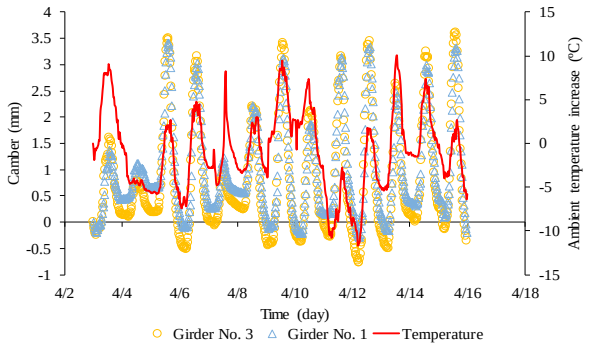


(c) 3rd ~ 15th April 2016

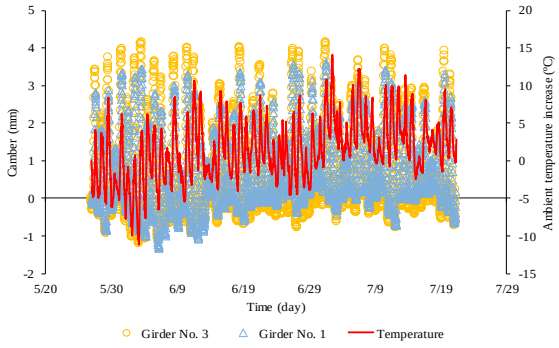


(d) 27th May ~ 21st July 2016

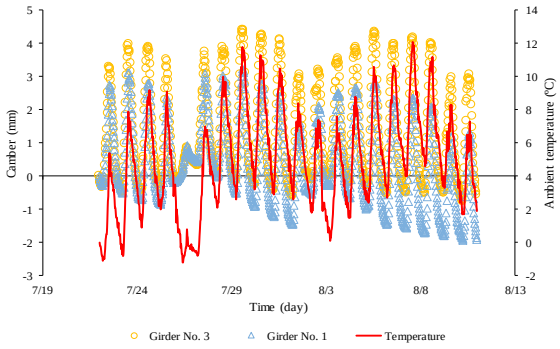


(e) 22nd July ~ 10th August 2016

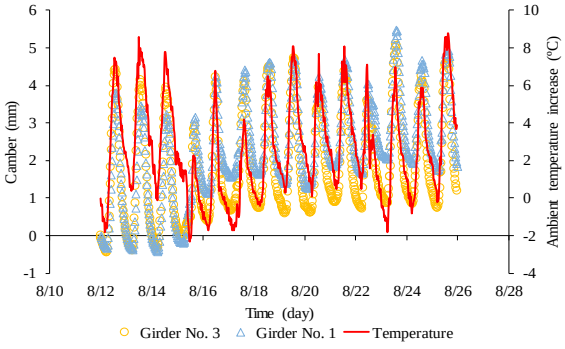


(f) 12th ~ 25th August 2016

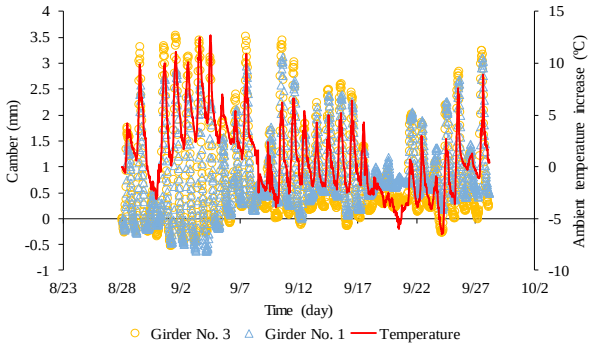


(g) 28th August ~ 28th September 2016

*Figure 5.6 Changes in nodal displacement at span center during monitoring period*

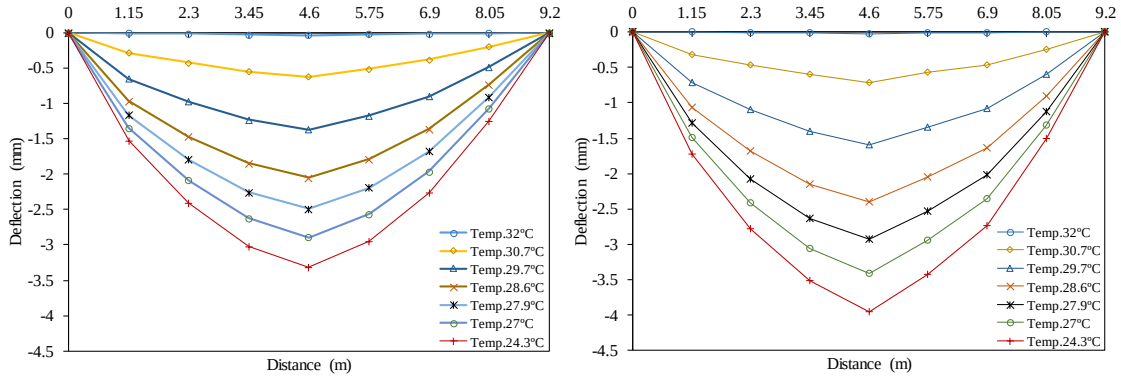


(a) Girder No.1 (b) Girder No.3

*Figure 5.7 Changes in nodal displacement at span center when the ambient temperature decrease*

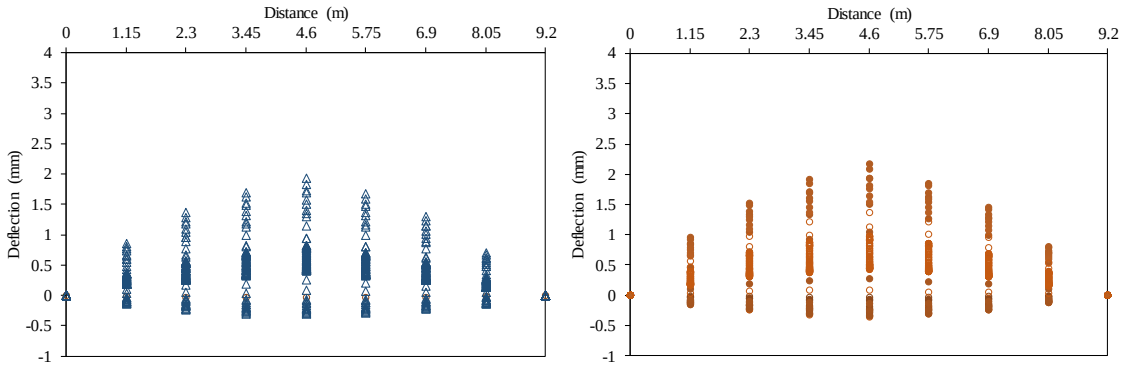


(a) Girder No.1 (March 2016) (b) Girder No.3(March 2016)

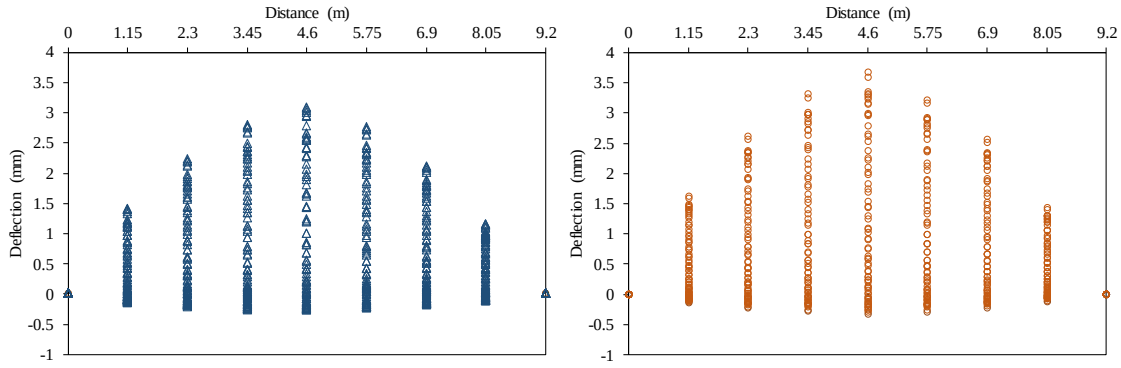


(c) Girder No.1 (September 2016) (d) Girder No.3(September 2016)

*Figure 5.8 Seasonal changes in nodal displacement at the observation points*

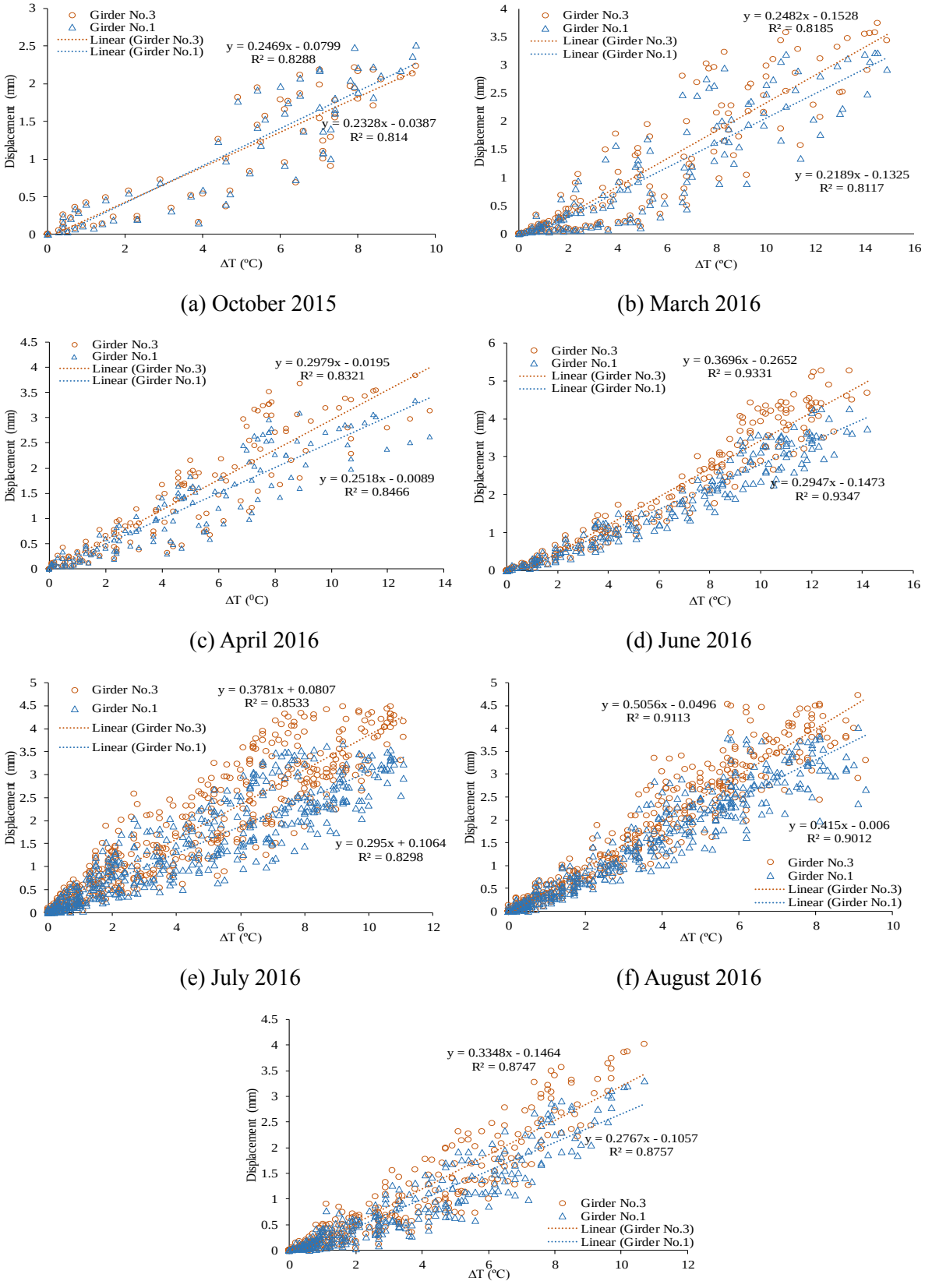


*Figure 5.9 Linear relation between the camper at midspan and the increase in ambient temperature*

*Table 5.1 Coefficients of linear regression model of girder No.1*

| Time | Intercept $\alpha_0$ | Gradient $\beta_t$ | Coefficient of determination $R^2$ | Correlation coefficient R |
|---|---|---|---|---|
| Oct-15 | -0.080 | 0.247 | 0.829 | 0.910 |
| Mar-16 | -0.132 | 0.219 | 0.812 | 0.901 |
| Apr-16 | -0.009 | 0.252 | 0.847 | 0.920 |
| Jun-16 | -0.147 | 0.295 | 0.935 | 0.967 |
| Jul-16 | 0.106 | 0.295 | 0.830 | 0.911 |
| Aug-16 | -0.006 | 0.415 | 0.901 | 0.949 |
| Sep-16 | -0.106 | 0.277 | 0.876 | 0.936 |

*Table 5.2 Coefficients of linear regression model of girder No.3*

| Time | Intercept $\alpha_0$ | Gradient $\beta_t$ | Coefficient of determination $R^2$ | Correlation coefficient R |
|---|---|---|---|---|
| Oct-15 | -0.039 | 0.233 | 0.814 | 0.902 |
| Mar-16 | -0.153 | 0.248 | 0.819 | 0.905 |
| Apr-16 | -0.019 | 0.298 | 0.832 | 0.912 |
| Jun-16 | -0.265 | 0.370 | 0.933 | 0.966 |
| Jul-16 | 0.081 | 0.378 | 0.853 | 0.924 |
| Aug-16 | -0.050 | 0.506 | 0.911 | 0.955 |
| Sep-16 | -0.146 | 0.335 | 0.875 | 0.935 |

**Figure 5.9(a)–(g)** shows positive correlations between the measured camber at midspan of the girders and the ambient temperature (specified in degree Celsius throughout this study), which was estimated during the monitoring period. These figures show that the amplitude of the upward movement increased with respect to the increased ambient temperature. For more information about the linear relationships of the camber concerning the temperature, a linear regression model was proposed. In this examination, camber variation from the lowest temperature time to the highest one of each regular day under the change in ambient temperature was studied. The corresponding empirical equation of the camber ($y$) as a function of the increase in temperature ($\Delta T$) is as follows.

$$y = \alpha_0 + \beta_t \Delta T + \varepsilon_f, \tag{5.10}$$

where y is the camber, $\alpha_0$ and $\beta_t$ are the regression coefficients named the intercept and the gradient, respectively, and $\varepsilon_f$ is the regression error. The measured ambient temperature increase was used as an explanatory variable. In this study, R was employed for statistical

computing [30]. With regard to the results of the statistical analyses, **Tables 5.1 and 5.2** list the estimated regression coefficients for girders No.1 and No.3, respectively.

From the above tables, the coefficients of determination $R^2$ for the cambers of girder No.3 and girder No.1 were estimated at high values, which was higher than 0.8. Therefore, more than 80 percent of the camber variances of the girders could be accounted for concerning the increase in ambient temperature. In particular, a change of ~93 % in the measured upward movement of the girders in June 2016 could be due to the change in temperature. Consequently, the corresponding correlation coefficient R was obtained over 0.9, which was significantly high values. Thus, there was a good relationship between the variation in camber at midspan and the temperature increase. These results demonstrate that the ambient temperature significantly affected the changes in the camber of the girders. Moreover, the fitted data regression line of girder No.1 had a slightly higher gradient than that one of the girder No.3 in October 2015, which was 0.247 compared to 0.233, respectively. However, since March 2016, the slopes of regression lines of girder No.3 had performed higher values than those of girder No.1. This observation results can be attributed to the increase in ASR-induced deterioration in girder No.1. As mentioned in the previous chapter, the three PC girders had been constructed in April 2015 and the initial measurement, which was carried out after the construction only six months, led to a conclusion that girder No.1 was more sensitive to temperature than girder No.3 by comparing the gradient of both girders in October 2015. As the ASR causes mini cracks on the upper surface of girder No.1 and leads to a reduction in the modulus of elasticity as well as the difference in expansion behavior of the top and bottom of the girder, the convex curvature occurs and keeps increasing in girder No.1 during the followed period. Therefore, girder No.1 was already likely in an upward curl shape during the measurements. In contrast to girder No.1, girder No.3 had a slight sign of cracks and a small convex upward shape. Based on the observation results, it can propose that the difference in upward curl shape between girders No.1 and No.3 might affect the variation in monitored camber, and led to the higher values in temperature-induced displacement in girder No.3 as compared to the results of the girder No.1 since March 2016. Besides, it was found that during a year of monitoring, the measured camber of girder No.1 increased by ~0.21 mm – ~0.41 mm when ambient temperature increased by one degree, this variation of girder No.3 was observed as ~0.23 mm – ~0.5 mm. Moreover, the regression model also provided a conclusion that approximately ~81% – ~93% of measured displacement could be accounted for by temperature, which indicated the ambient temperature increase was not the only factor that influenced the upward movement. Thus, it is believed that this static response was also affected by other factors such as the humidity, ASR-induced degradation, noise from equipment and the calculation process. This conclusion should be considered in structural damage detection using only changes in displacement data in practice because the environmental conditions might cause unexpected errors in measured responses in

the measurement field.

### 5.4 Displacement variation ratio

The difference in upward curl shape between girders No.1 and No.3 made the comparison of the cambers of two girders become more complicated. In other words, it was difficult to figure out the effect of ASR deterioration on the change in camber of the girder by evaluating the measured data of girder No. 3, which had fly ash in the mixture to mitigate the ASR acceleration, and girder No. 1 affected by ASR. Therefore, to make a consistent comparison in temperature-induced camber between the girders, this study assumed that the camber varied linearly with the variation in the ambient temperature. Based on this assumption, the displacement variation ratios of the girders No.1 and No.3 were estimated and plotted in **Fig. 5.10(a)–(f)**. The cambers were normalized by the first camber caused by the first temperature increase in the monitoring period. As shown in these figures, before May 2016, the variations in the cambers were similar in both girders since no significant difference between two girders were obtained. From May 2016, the differences in the estimated variation ratios manifested over time. In particular, girder No.1 exhibited a higher discrepancy and more obvious scatter with no notable trend compared to the results of girder No.3, as shown in **Fig. 5.10(d)–(f)**. This noise is likely because of the ASR-induced deteriorations because many longitudinal cracks were observed on the top, bottom, and both side surfaces of the girders No.1 whereas girder No.3 suffered only a few throughout one year of monitoring. Therefore, from the observation results, it has been shown that, from May 2016, the vertical displacement at midspan of girder No.1 caused by the ambient temperature variation did not vary with the linear rate during the measurements when compared to that of girder No.3. Because the cross-sections of the two girders were the same with similar mixtures, and were placed at the same place and tested concurrently during each measurement, the difference in the displacement variation ratio was probably not due to the changes in temperature. This difference can be attributed to the increased development of cracks caused by ASR that makes the behavior of girder No.1 more complex.

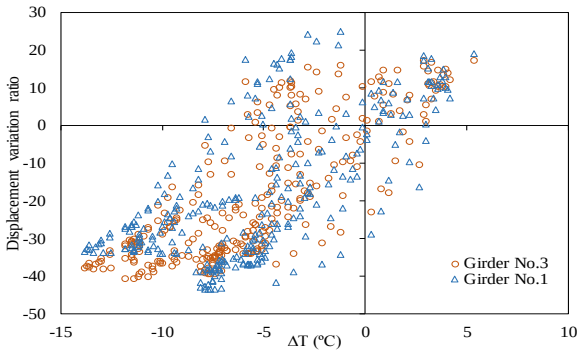


(a) 21st ~ 27th October 2015

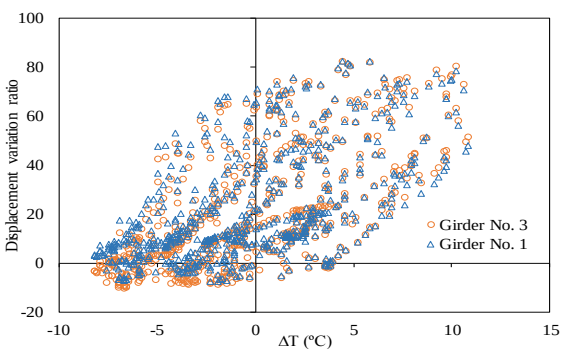


(b) 18th ~ 31st March 2016

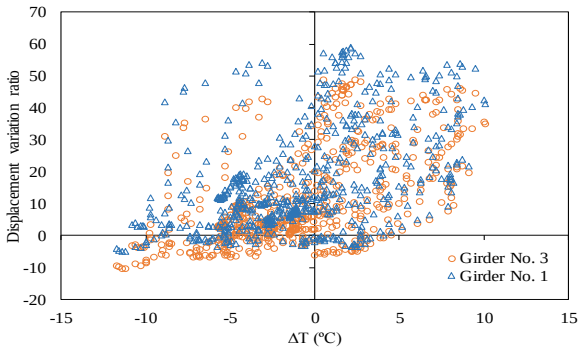


(c) 3rd ~ 15th April 2016

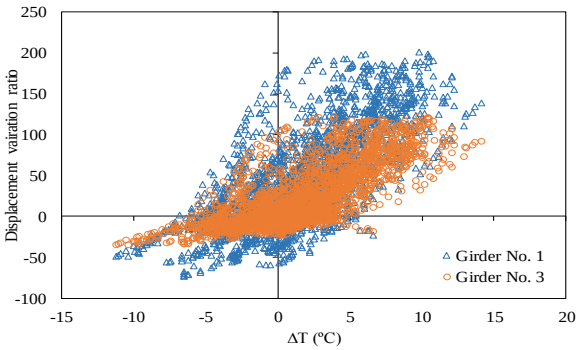


(d) 27th May ~ 21st July 2016

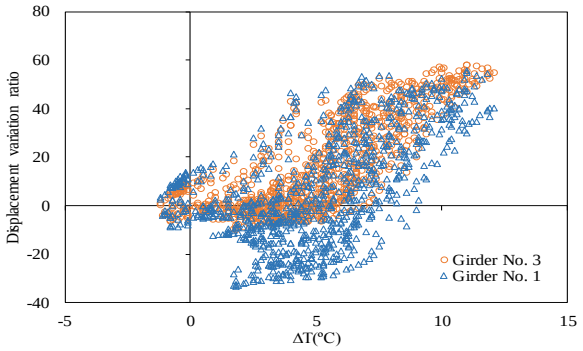


(e) 22nd July ~ 10th August 2016

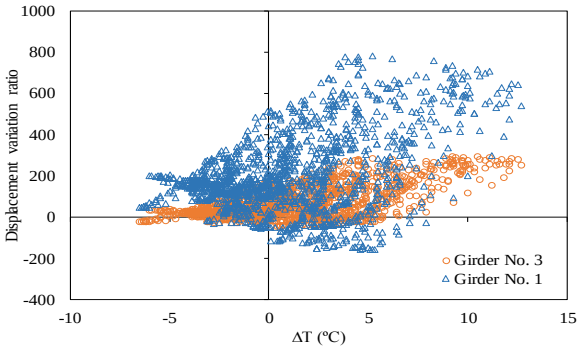


(f) 28th August ~ 28th September 2016

*Figure 5.10 Changes in displacement variation ratio at span center during monitoring period.*

## 5.5 Numerical modeling

Once camber behavior was observed experimentally, it was expected that numerical upward displacement would vary directly with temperature and would be similar in magnitude to the experimental results. A finite element (FE) model previously developed in **Chapter 4** was used to perform preliminary FE simulations of temperature-induced changes in camber of the PC girders. The primary purpose of the simulations was to confirm that camber occurs in PC girders and to estimate the magnitude of this camber. Therefore, this study performed a structural linear static analysis including thermal effects on this model using the FE software DIANA. The critical parameters governing the numerical model were the coefficients of thermal expansion of the concrete and steel were assumed as 1e–5 and 1.2e–5 1/ºC, respectively. The model was constrained at both ends by a pinned support and a roller support, as shown in **Fig. 5.11(a)**. The FE simulations involved a combination of three loads, which were the self-weight load, pretensioning forces, and a temperature gradient. This gradient varied in magnitude and was assumed to be linear based on studies of Armaghani et al. [6] and Wolf et al. [5]. The temperature gradient was obtained from the measured ambient temperature and input to the numerical model as the difference in the temperature at the top of the girder and the temperature

at the bottom of the girder. The camber caused by an increase in ambient temperature was numerically defined by taking the difference in camber caused by two reference temperature gradients. Firstly, a reference gradient of temperature ($\Delta T$) was inputted to the model by assigning elemental temperature throughout the height of the cross-section (450 mm) from $T_1$ at the top elemental layer to $T_2$ at the bottom layer of the girder (see **Fig. 5.11(b)**). Then, the temperature-induced displacement ($u$) was calculated by linear numerical analysis. When there is an increase in temperature, a new reference gradient of temperature ($\Delta T'$) was inputted to the girder in the same way to the previous one. The corresponding movement ($u'$) was also estimated numerically. The target increase in camber was derived from two estimated displacement curves by making the difference $\Delta u = u - u'$ between them.

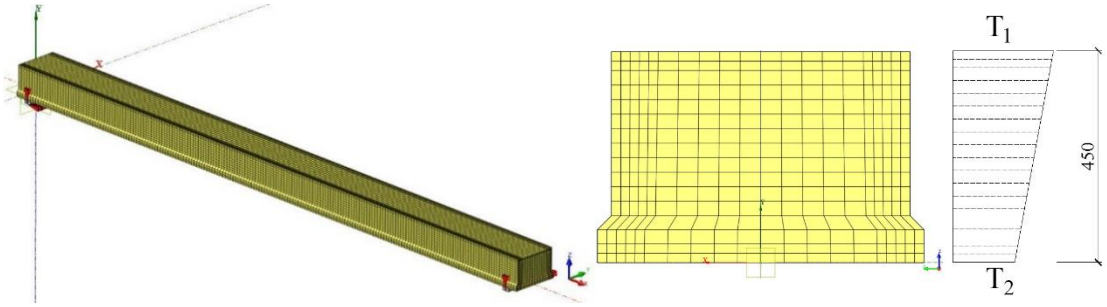


(a) FE model (b) Assumption of the temperature gradient

*Figure 5.11 FE model set up*

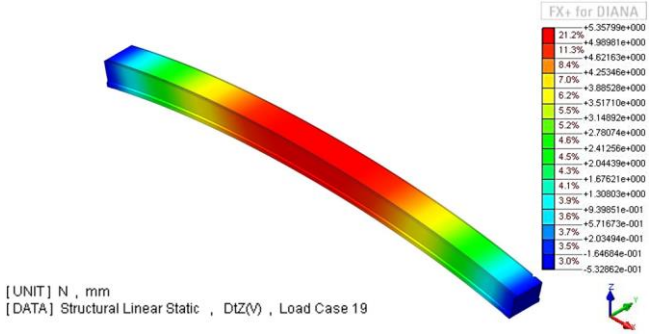


*Figure 5.12 Temperature-induced camber when $T_1 > T_2$*

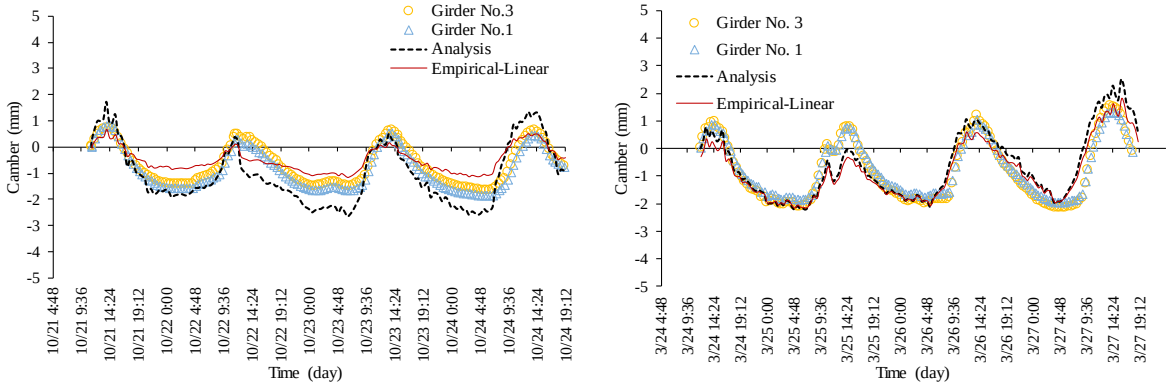


(a) 21st ~ 24th October 2015 (b) 24th ~ 27th March 2016

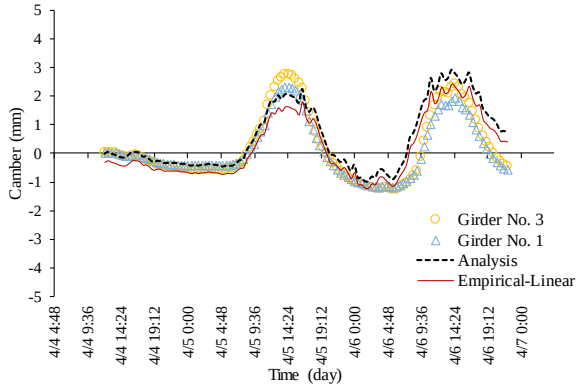


(c) 4th ~ 7th April 2016

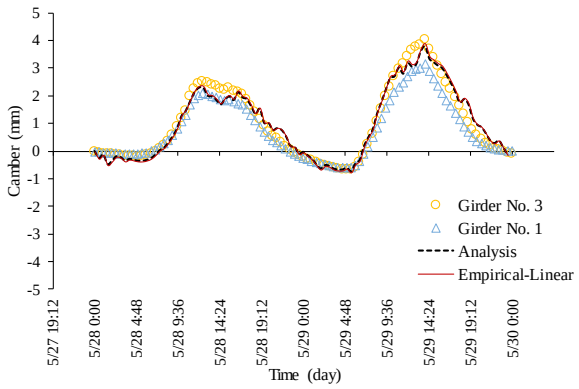


(d) 28th ~ 30th May 2016

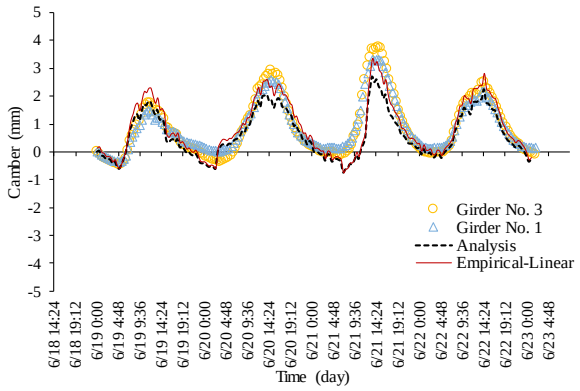


(e) 19th ~ 23th June 2016

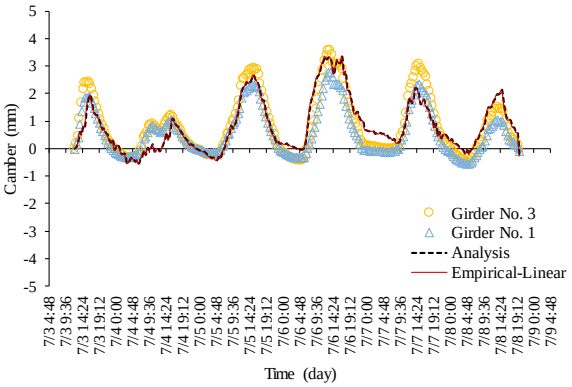


(f) 3rd ~ 9th July 2016

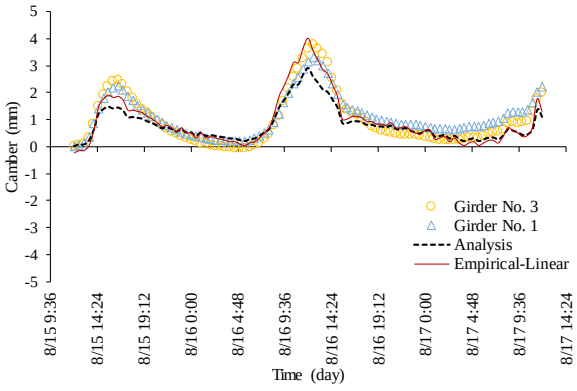


(g) 15th ~ 17th August 2016

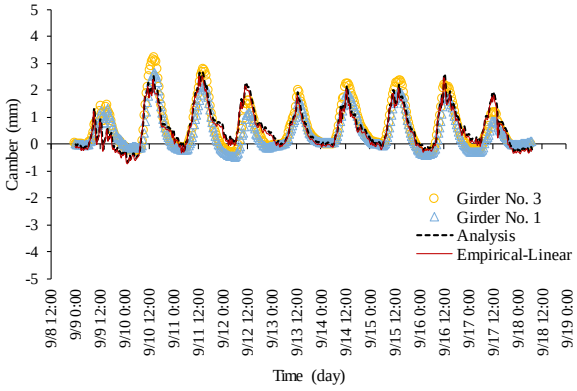


(h) 8th ~ 18th September 2016

*Figure 5.13 Comparison of measured and computed camber.*

**Figure 5.12** shows an illustration of an upward analytical camber when the temperature at the top is higher than the temperature at the bottom of the girder. Also, **Fig. 5.13(a)–(h)** provides a graphical comparison between the measured camber, analytical camber, and camber computed with the trend line (empirical-linear). The numerical model produced comparatively similar

values compared to the measurement. Therefore, the FE model can be calibrated to more closely match the experimental camber and provide more accurate predictions of the camber in the future. Positive relationships between the camber and the ambient temperature were obtained in the results: the temperature increased with the increases in the cambers. Also, both the numerical values and the values obtained from the empirical equation of the camber ($y$) as a function of the increase in temperature ($\Delta T$) followed an expected trend. Regarding **Fig. 5.13(d)** showing the results obtained in May 2016, the cambers increased and reached their maximum positive value in the mid-afternoon, then dropping down to a relatively constant maximum negative value in the early morning hours. In particular, the temperature varied by ~7.2 ºC from approximately ~18.1 ºC at 0 a.m. to ~25.3 ºC at 12 p.m. in 28$^{th}$ May 2016. This increase led to variations in the analytical camber and the empirical-linear camber by ~2.3 and ~2.33 mm, respectively. This rate was obtained at ~2.03 and ~2.43 mm with respect to the measurement of girders No.1 and No.3, respectively. The measured temperature then decreased gradually by ~9.1 ºC from a high temperature to ~16.2 ºC at 5 a.m. on 29$^{th}$ May 2016. Consequently, the experimental cambers of girders No.1 and No.3 decreased to ~0.6, ~0.66 mm, respectively. The analytical value and the value obtained from empirical equation were estimated at ~0.6 and ~0.65 mm, respectively. These FE simulations showed that the camber at midspan of the PC girders was directed related to the temperature gradient and was not small. Based on these results and the graphical comparison, it is seen that both analytical camber and empirical-linear camber can be used to estimate camber using temperature data. Moreover, the correlation between the variations in the camber and the ambient temperature could be proved rationally using the FE model developed in this study.

There was a slight discrepancy between the measurements and the numerical results because Young's moduli applied in the analysis might not match the exact moduli of the whole girder, particularly because the girder is PC. As presented in Chapter 2, mechanical characteristics of the concrete cores altered based on their collecting positions and directions. In particular, due to the restraining stress of the PC strands along with the low expansion rate of concrete, the concrete samples obtained longitudinally from the central part presented weaker compressive strengths compared to the specimens gathered from the transverse direction. When analyzing the outcomes achieved for the central and the end parts, the mechanical features of the concrete cores of the end portion were smaller than those of the central part. Besides, the ambient temperature, which was used as the input in the governing linear equation and the FE model, did not significantly changes the temperature of the girder instantaneously because of its large thermal mass. A study of T.E. van der Meer [22] showed that an element that is subjected to a different temperature would not immediately adjust its temperature. It will take time for the heat of a body to approach that of its surrounding, due to the thermal inertia of the same body. In other words, the transfer of energy throughout the element is not immediate. If the

temperature is measured inside a material, a damping effect of the temperature changes should be observed. Therefore, the entered temperature profile might not precisely follow the heat of the girder.

The selected regression model and the analysis model were only suitable for a temperature range and the monitoring period as presented in this study. Because during winter under the effect of frost attack, the behavior of the girder might become more complex and unpredictable. Moreover, if the follow-up time is extended further, the change in the position of supports and the effect of ASR might affect the measurement results undoubtedly.

### 5.6 Conclusions

In this study, the effect of the changes in the ambient temperature and the ASR-induced deteriorations on the camber variation of two PC girders with non-identical mixtures was monitored for almost one year. The main conclusions drawn from this study are as follows.

- ✓ The ambient temperature not only varied from season to season but also throughout any given day. Daily and seasonal variations in ambient temperature led to changes in the camber of the girders. All values measured from displacement meters had positive correlations with temperature. In other words, the amplitude of the camber increased with respect to the increase in the ambient temperature.
- ✓ As another result of the linear regression model, the ambient temperature gradient strongly affected the changes in the cambers of the girders because the correlation coefficients between the variables were strong, as computed using the linear model. The measured camber of girder No.1 increased by ~0.21 mm – ~0.41 mm when ambient temperature increased by one degree, this variation of girder No.3 was observed as ~0.23 mm – ~0.5 mm. Approximately ~81% – ~93% of measured displacement could be accounted for by measured temperature. This conclusion should be considered in structural damage detection using only changes in displacement data in practice because the environmental conditions might cause unexpected errors in measured responses in the measurement field.
- ✓ The camber could be related to temperature gradient using analytical or empirical methods. These approaches allowed camber to be approximated using only ambient temperature data. In this study, cambers in PC girders were accurately modeled and predicted in finite element simulations.
- ✓ Because the static behaviors of the two girders were observed to be quite different, the fly ash significantly affected the performances of the PC girders under the ASR damage.

## 5.7 References


[1] M. Priestley, "Thermal gradients in bridges - some design considerations," *New Zeal. Eng.,* vol. 27, pp. 228–233, 1972.

[2] W. J. Price, "Introductory Note, Bridge Temperatures*," TRRL Report SR 442, Transport and Road Research Laboratory*, 1978.

[3] H. Wenzel, "*Health Monitoring of Bridges*," 2009.

[4] P. J. Barr, J. F. Stanton, and M. O. Eberhard, "Effects of Temperature Variations on Precast, Prestressed Concrete Bridge Girders," *J. Bridg. Eng.,* vol. 10, pp. 186–194, 2005.

[5] H. E. Wolf, Y. Qian, J. R. Edwards, M. S. Dersch, and D. A. Lange, "Temperature-induced curl behavior of prestressed concrete and its effect on railroad crossties," *Constr. Build. Mater.,* vol. 115, pp. 319–326, 2016.

[6] J. M. Armaghani, T. J. Larsen, and L. L. Smith, "Temperature response of concrete pavements," *Transp. Res. Rec.,* vol. 1211, pp. 23–33, 1987.

[7] H. T. Yu, L. Khazanovich, M. I. Darter, and A. Ardani, "Analysis of concrete pavement responses to temperature and wheel loads measured from intrumented slabs," *Transp. Res. Rec.,* vol. 1639, pp. 94–101, 1998.

[8] S. Rao and J. R. Roesler, "Characterizing Effective Built-In Curling from Concrete Pavement Field Measurements," *J. Transp. Eng.,* vol. 131, pp. 320–327, 2005.

[9] R. A. Imbsen, D. E. Vandershaf, R. A. Schamber, and R. V. Nutt, "*Thermal effects in concrete bridge superstructures*," 1985.

[10] M. T. Ha and S. Fukada, "Vibration and structural performance of PC deteriorated girder under varying environmental conditions," in *Mechanics of Structures and Materials: Advancements and Challenges* (eds. Hao, H. & Zhang, C.), pp.767–773, Taylor & Francis Group, London, 2017.

[11] C. Zhao, X. Song, and X. Zhu, "Temperature Deformation Analysis of CRTS II Ballastless Slab Track," *V001T01A016*, 2013.

[12] J. Ren, R. Yang, P. Wang, P. Yong, and C. Wen, "Slab Upwarping of Twin-Block Slab Track on Subgrade-Bridge Transition Section: Parameter Study and Repair Method," *Transp. Res. Rec. J. Transp. Res. Board,* vol. 2448, pp. 115–124, 2014.

[13] X. Song, C. Zhao, and X. Zhu, "Temperature-induced deformation of CRTS II slab track and its effect on track dynamical properties," *Sci. China Technol. Sci.,* vol. 57, pp. 1917–1924, 2014.

[14] P. C. Hoffman, R. M. McClure, and H. H. West, "Temperature Study of an Experimental Segmental Concrete Bridge," *PCI J.*, pp. 78–97, 1983.

[15] A. S. Usmani, J. M. Rotter, S. Lamont, A. M. Sanad, and M. Gillie, "Fundamental principles of structural behaviour under thermal effects," *Fire Saf. J.,* vol. 36, pp. 721–

744, 2001.

[16] P. J. Barr, M. O. Eberhard, J. F. Stanton, B. Khaleghi, and J. C. Hsieh, "*High Performance Concrete in Washington State SR 18/SR 516 Overcrossing: Final Report on Girder Monitoring,"* 2000.

[17] J. F. Stanton, M. O. Eberhard, and P. J. Barr, "A weighted-stretched-wire system for monitoring deflections," *Eng. Struct.,* vol. 25, pp. 347–357, 2003.

[18] S. R. Debbarma and S. Saha, "Behavior of pre-stressed concrete bridge girders due to time dependent and temperature effects," in *First Middle East Conference on Smart Monitoring, Assessment and Rehabilitation of Civil Structures,* 2011.

[19] J.-H. Lee and I. Kalkan, "Analysis of Thermal Environmental Effects on Precast, Prestressed Concrete Bridge Girders: Temperature Differentials and Thermal Deformations," *Adv. Struct. Eng.,* vol. 15, pp. 447–460, 2012.

[20] E. H. El-Tayeb, S. E. El-Metwally, H. S. Askar, and A. M. Yousef, "Thermal analysis of reinforced concrete beams and frames," *HBRC J.,* vol. 13, pp. 8–24, 2015.

[21] D. Banks, "*An introduction to thermogeology: Ground source heating and cooling: Second edition*," 2012.

[22] T. E. van der. Meer, "Temperature Regulated Concrete Bridges An alternate approach to reduce temperature load," Delft University of Technology, 2015.

[23] Dutch standard organization, "*Eurocode 1: Actions on structures – part 1-5: General actions – Thermal actions*," vol. NA NEN-EN 1991-1-5, Delft, 2011.

[24] E. J. Hoppe, "*Evaluation of Virginia's First Heated Bridge (No. FHWA/VTRC 01-R8)*," 2000.

[25] S. Arsoy, "Experimental and Analytical Investigations of Piles and Abutments of Integral Bridges," Doctoral Thesis, Virginia Polytechnic Institute and State University, Blacksbug, Virginia, 2000.

[26] D. D. Girton, T. R. Hawkinson, and L. F. Greimann, "Validation of Design Recommendations for Integral-Abutment Piles," *J. Struct. Eng.,* vol. 117, pp. 2117–2134, 1991.

[27] R. Hällmark, "Low-cycle fatigue of steel piles in integral abutment bridges," Lulea University of technology, Lulea, 2006.

[28] H. G. Russel and L. J. Gerken, "Jointless bridges – The known and the unknown," *Concr. Int.,* vol. 16, pp. 44–48, 1994.

[29] European Committee for Standardization, "Actions on structures – part 1-5: General actions – Thermal actions," *Eurocode 1,* vol. EN 1991-1-5.

[30] The R Manuals, "The R Manuals." [Online]. Available: https://cran.r-project.org/manuals.html. [Accessed: 20-Jul-2004].

# Chapter | 6

# Application of Damage Detection Method Using Displacement Data for Deteriorated Girder

## 6.1 Introduction

Civil engineering structures inevitably experience material degeneration, environmental corrosion, traffic loads, and even natural hazards such as earthquakes and typhoons. Damage detection is an essential tool for structural health monitoring and health assessment. For many years, many kinds of damage detection techniques have been thoroughly improved as presented in the literature review section of **Chapter 3**. These approaches employed the variations in vibrational components and static responses of a structure before and after damage.

In this chapter, efforts have been performed to utilize Displacement Assurance Criterion (DAC) proposed in **Chapter 3** on practical cases. DAC demonstrates the level of relationship between two displacement curves at different states of a structure and is employed for detecting the existence of a stiffness loss. Therefore, destructive tests were performed on the PC girders to evaluate the feasibility of DAC approach on damage detection by analyzing the displacement curves obtained from the experiments. During the destructive test presented in **Chapter 2**, the vertical displacement was measured at seven pointed on the lower extreme fiber for calculating the deflection curve at each loading step. Then, the obtained curves were analyzed to estimate the variation in the DAC value. Besides, nonlinear finite-element models of the PC girders were produced to verify the relation between the variations in DAC with respect to structural degradation owing to applied loads in practice. From the obtained results of the numerical and experimental approaches, this study aims to propose a threshold of DAC index for the sound structure. If a structure performs a higher value of DAC than the threshold, it can be judged as safety structure. Conversely, the system will give warnings about the health of that structure.

## 6.2 Loading test

### 6.2.1 Outline of loading test set-up

After one and a half years of the outdoor exposure, loading test was carried out on girders No.2 and No.3 by using the equipment shown in **Fig. 6.1**. For the loading method, a simply supported

specimen was subjected to the four-point bending test. A 1500 kN hydraulic jack and one load cell were placed at midspan for applying and measuring the loading. Additionally, the loading positions were located at 4.1 m from both supports and the interval between two loading points was 1 m. Wire displacement meters (**Fig. 6.2(a)**) and the high-sensitive displacement meters (**Fig. 6.2(b)**) were also placed at seven positions under the girder to measure the flexural deformation of the investigated girder depending on the applied load. Then, for obtaining the bending crack opening load, 26 Pi-shaped displacement gauges were arranged on the bottom of lower flange and in the range of 1.5 m around the middle of the span, as shown in **Fig. 6.2(c)**. Additionally, 12 strain gauges were pasted on the top and bottom surfaces of the girder at the center of the span.

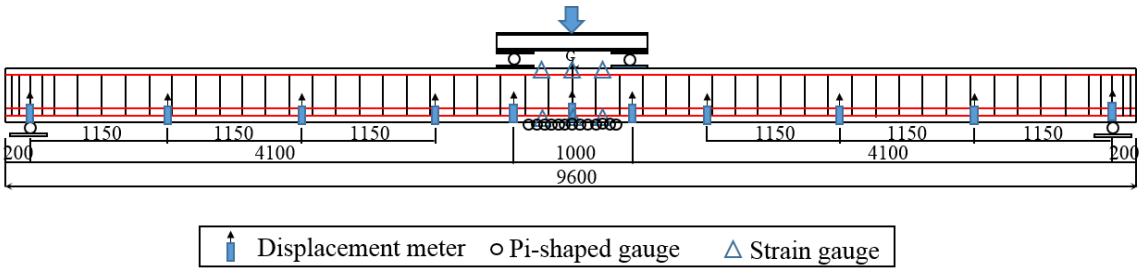


*Figure 6.1 Overview of loading test setup (unit: mm).*

(a)Wire displacement meters

(b) High-sensitive displacement meters

(c) Pi-shaped displacement gauge

*Figure 6.2 Measuring devices*

### 6.2.2 Loading Test Results of Girders No. 2 and No. 3

The deflections of both girders under each loading step are presented in **Fig. 6.3**. In this figure, at the same loading step, all the measured displacement data of girder No. 2 exhibited larger values compared to the ones of girder No. 3. Moreover, the relationship between the applied load and the displacement at the center of the span are shown in **Fig. 2.12** (see **Chapter 2**). According to the result of girder No. 2, the profile of displacement distribution was linear when the applied load was approximately less than 170 kN but nonlinear when the applied load was more than 180 kN. This result, therefore, shows that the girder No. 2 started yielding from around 170 kN. On the other hand, girder No. 3 provided higher structural performances at all loading states, as compared to girder No. 2 without fly ash. At the end of the loading process, the maximum applied load of girder No. 2 and girder No. 3 were recorded at approximately 313 kN and 330 kN, respectively. In other words, the addition of fly ash increased the load-bearing capacity of the objective girder by 5% at the final state.

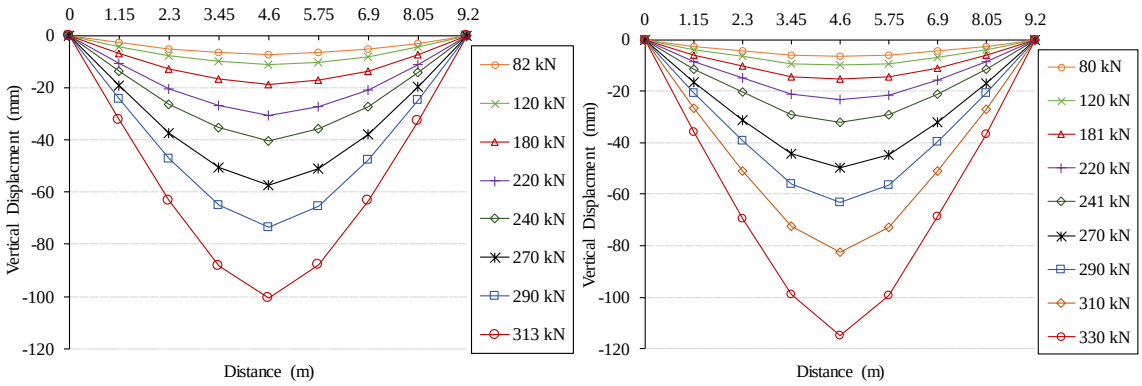


(a) Girder No.2 (b) Girder No.3

*Figure 6.3 The measured deflection curves*

### 6.2.3 Variation in Displacement Assurance Criterion (DAC) under applied load

In this chapter, the displacement assurance criterion (DAC) proposed in **Chapter 3** is used to analyze the effect of damage on static displacement curve. The DAC expresses the correlation degree of two displacement curves at different states of a structure and is simply calculated by **Eq. (3.2)** in **Chapter 3**. The displacement of each measured position was extracted from the measurement and normalized with the largest one, at each loading step. Then, the normalized displacement curve of some of the nominated load cases can be estimated and represented in **Fig. 6.4**. In this figure, a decrease in the magnitude of the normalized displacement curve can be observed. In other words, the normalized displacement curve shows a narrow tendency, in agreement with the increase in applied load. For determining DAC indices, the normalized

displacement curve of the girder when it undergoes an applied load of 70 kN was regarded as the reference curve. As results of the calculation, the variation of DAC values in each load case are shown in **Fig. 6.5**. According to **Fig. 6.5**, along with the increase of applied load, DAC exhibits a decrease in amplitude, which is observed in both girders. It should be noted that the DAC values show relatively small changes in amplitude and close to unity when the applied load is lower than the crack opening loads, which were measured at 170 kN and 190 kN on girder No. 2 and No. 3, respectively. After the occurrence of cracks, the DAC values decline until the end. Moreover, the calculated DAC values of girder No. 3 are higher than those of girder No. 2. This result indicates that girder No. 3 had a better correlation degree of displacement curves among loading states by comparing with girder No. 2. Therefore, it was cleared that there is a correlation between the variation of DAC and damage states. Through these results, DAC can be proposed as an index to figure out the occurrence of damages and more studies should be conducted to apply this indicator in practice.

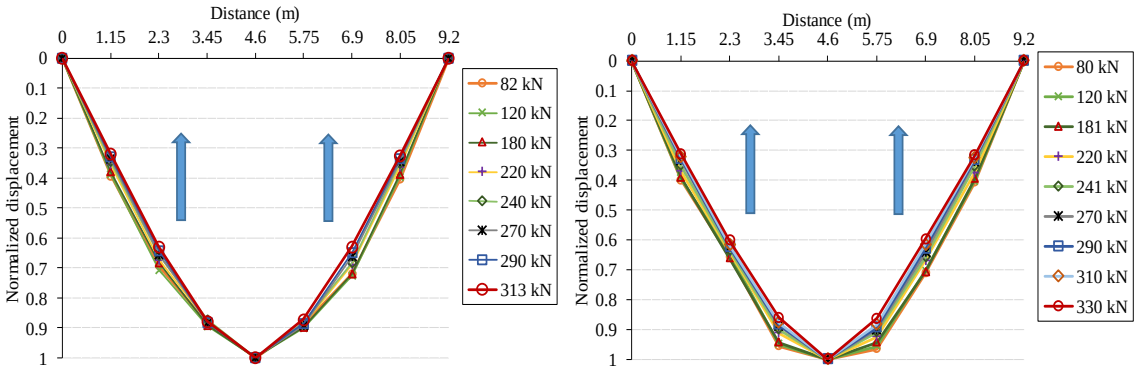


(a) Girder No.2 (b) Girder No.3

*Figure 6.4 The normalized deflection curves*

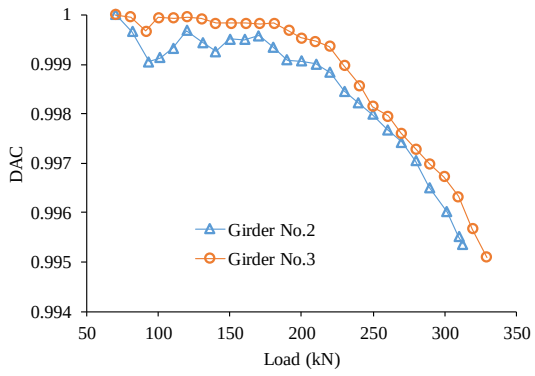


*Figure 6.5 Variation in DAC index of both PC girders*

## 6.3 Numerical analysis

### 6.3.1 Overview of the numerical models

Regarding numerical simulation, a commercial finite element code having precise capabilities of nonlinear analysis was operated to reproduce the plastic behavior of the PC girders and to verify results of DAC variation. In the numerical procedure, first and foremost the models were validated by comparing the results with those obtained in real-scale experiments. The emphasis here is on the methodology; i.e., how to apply the FE analysis to reproduce the behavior of girder No.2 which have many ASR-induced cracks. Because the destructive test itself contains a structural nonlinear characteristic and significant deformation, modeling the behavior of the specimen until the final state requires the consideration of both high order geometrical and nonlinear mechanical parameters, and particularly on selected nonlinear models. The developed model considered the nonlinear mechanical properties of concrete and steel. To facilitate simulation, some simplifying assumptions for mechanical properties of materials, and supports were adopted.

From observation results on the cut cross-sections, the depth of ASR-induced cracks along the girder-axis direction varied from 5 to 20 mm on the side surfaces and the top surface, whereas no crack was found out in the area surrounded by stirrups. Moreover, no breaking of tendons was confirmed. After the bending test, for ascertaining the corrosion condition of PC strands, peeled concrete areas of both samples were taken away. However, no steel corrosion could be observed. Therefore, the property values should be different between the surface and the inside regions with respect to the numerical model of girder No.2. This modeling approach for the ASR-affected beam structure was proposed by Hiroi et al. [1] for the reproduction of the loading test on a real-scale large prestressed concrete beam specimens exposed to 7.5 years of ASR deterioration. Their results showed that the proposed method was capable of reproducing the loading test results in initial stiffness, maximum load, and strains of the ASR specimen. Thus, this study assumed the thickness of the surface layer affected by ASR-induced cracks as 20 mm in the 3D model. Because the previous results show that girder No.3 exhibited much lower levels of damage due to the ASR compared to the other two girders, the material properties of the surface and inside regions were assumed to be the same in the numerical model. In contrast, the material properties were different between the surface and inside regions of the model for girder No.2.

As shown in **Fig. 6.6**, a 3D numerical model is produced following the specifications of the actual specimen by FX+ For DIANA, which is a commercially available program for nonlinear finite element analysis. Regarding element types employed for the investigation, the concrete was modeled as solid elements, while the bar in beam elements reproduced the stirrups and the PC strands. The bonding force between the concrete and steel materials was assumed as

complete. Self-weight and prestress were assigned as the initial load step. The energy-controlled convergence norm and the regular Newton-Raphson were selected for iterative method. The analysis was carried out by applying incremental load factor with specified sizes.

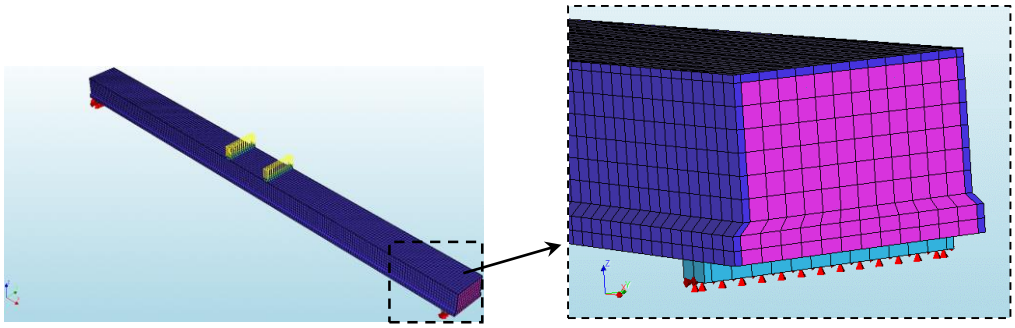

*Figure 6.6 3D analysis model*

### 6.3.2 Material properties of concrete

The rotating total strain crack model for the concrete [2], which includes the JSCE tension softening model for tensile behavior and the multi-linear model for compressive behavior, was employed here. Parameters of concrete for the rotating strain crack model with rotating crack orientation are presented in **Table 6.1**. Specifically, Young's modulus and compressive strength of concrete of girder No.3 and inner region of girder No.2 were obtained from compression tests on concrete cores collected from the actual samples. The stress-strain curves of concrete of girder No.3, which were used for the multi-linear model, were illustrated in **Fig. 6.7**. The fracture energy of concrete is the energy consumed to form cracks per unit area, and is calculated by **Eq. (3.7)** [3]. Also, owing to the absence of experimental data, the estimation of the tensile strength of concrete $f_{tk}$ can be done by **Eq. (3.8)** based on the characteristic compressive strength $f'_{ck}$ [3].

*Table 6.1 Concrete properties for the total strain crack model*

| Girder | Part | Young's modulus ($N/mm^2$) | Poisson's ratio | Compressive Strength ($N/mm^2$) | Tensile Strength ($N/mm^2$) | Maximum size of coarse aggregate (mm) | Fracture energy (N/mm) |
|---|---|---|---|---|---|---|---|
| No.2 | Surface layer | 23920 | 0.16 | 70.018 | 3.907 | 20 | 0.1119 |
| | Inside region | 29900 | 0.16 | 87.678 | 4.539 | 20 | 0.1206 |
| No.3 | Surface layer | 36450 | 0.16 | 106.228 | 5.159 | 20 | 0.1286 |
| | Inside region | 36450 | 0.16 | 106.228 | 5.159 | 20 | 0.1286 |

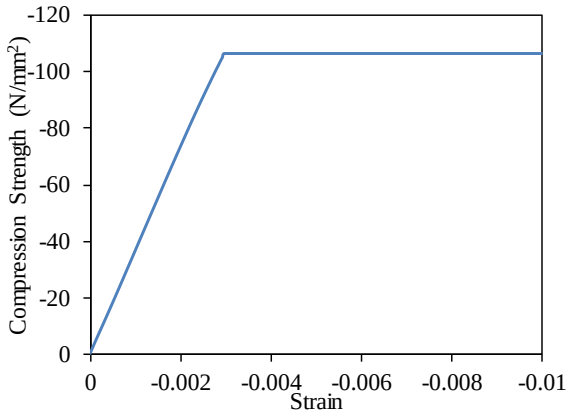


*Figure 6.7 Stress-strain relationship of concrete of girder No.3*

### 6.3.3 Steel materials

The stirrups were assumed as in the linear elastic material model with a Young's modulus $E_s$=191000 N/mm$^2$, and Poisson ratio $\nu = 0.3$. Regarding the PC strands, Von Mises plasticity was employed to simulate the nonlinear behaviors. Specifically, the strands were defined by a property with a Young's modulus $E_s$=191000 N/mm$^2$, and Poisson ratio $\nu = 0.3$. The yield stress was defined as 1797 N/mm$^2$ based on results of the tensile test. Regarding the prestressing force for the PC strands, a value of 1225.3 N/mm$^2$ was assigned to the first layer of PC strands in the compression area (4 strands) while the other two layers in the tension area (6 strands) were subjected to a presstress of 1166.7 N/mm$^2$. In addition, the prestress was applied to the numerical model as the initial stress at the execute start step.

### 6.3.4 Load-displacement relationship and crack pattern

**Figure 6.8** shows the experimental and numerical results of the load-displacement relationship extracted at midspan of the models. From this figure, the displacement increases in agreement with the growth in loading up to approximately 170 kN with respect to the numerical result of girder No.2. After the strands had yielded and the slope of the curve had changed, the displacement increased moderately, and the load was later terminated when the movement at the observed point reached approximately 98.32 mm with the corresponding applied load of 315 kN. Regarding experimental results, these values were measured at 100.6 mm and 312.72 kN for the maximum displacement and loading, respectively. The 3D model developed for girder No.3 also provided good agreement with the experimental results as shown in **Fig. 6.8(b)**. The numerical crack pattern at maximum loading is shown in **Fig. 6.9**. From the obtained results, it can be asserted that the FE model provides reasonable conclusions on the ultimate strength behavior of the specimen and is useful for further parametric analyses. Iterative execution

allows us to explore the structural role of each component at the proposed connection and how these parts cooperate with one another during the test. For the next steps, a series of numerical simulations will be carried out to examine the relation between damage severity and changes in nodal displacement, and to verify the feasibility of DAC.

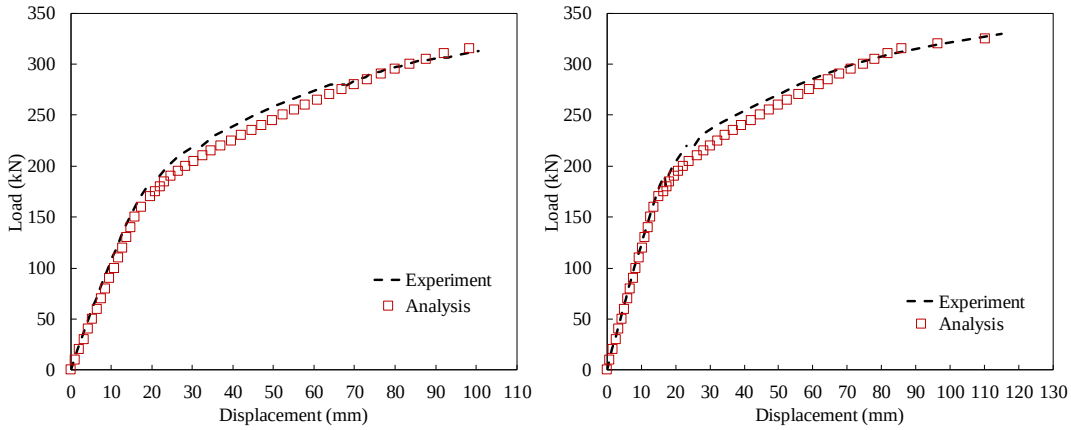


(a) Girder No.2 (b) Girder No.3

*Figure 6.8 Displacement-load relationship at midspan of the numerical models*

*Figure 6.9 Crack pattern after the destructive load*

### 6.3.5 Variations of numerical values of DAC with the increased loading

The relation between the variations in DAC with the structural degradation of the actual PC girders has been proven experimentally in **Subsection 6.2.3**. This section aims to verify the experimental results of the DAC calculation and to clarify the sensitivity of the factor DAC in detecting the existence of deterioration. To identify the changes in structural responses caused by the presence of damage, the deflections of seven points marked under the target girder were obtained.

The displacement at each finite-element node is normalized with the largest one, at each loading step. Then, the normalized displacement curve of some of the nominated load cases can be

estimated and represented in **Fig. 6.10**. In this figure, a decrease in the magnitude of the normalized displacement curve can be observed. In other words, the normalized displacement curve presents a narrow tendency, in agreement with the increase in applied load. This result was also confirmed by evaluating the experimental data shown in **Subsection 6.2.3**. For determining DAC indices, the normalized displacement curve of the numerical model when it undergoes an applied load of 5 kN was regarded as the reference curve. The effect of increased applied load on DAC values relating to FE models of girders No.2 and No.3 are presented in **Fig. 6.11**. The decreases in the analytical results of DAC of girders No.2 and No.3 in **Fig. 6.11** agree well with the results of loading test. Furthermore, after the elastic stage, DAC values of girder No.3 are higher than those of girder No. 2, and the deviations increase significantly with the increased loading. These results demonstrate the standpoint that there is a relation between damage severity and changes in nodal displacement, represented in this study as the factor DAC. In addition, the employed approach for numerical calculation could reproduce the loading tests on the PC girder affected by ASR and provide reasonable results.

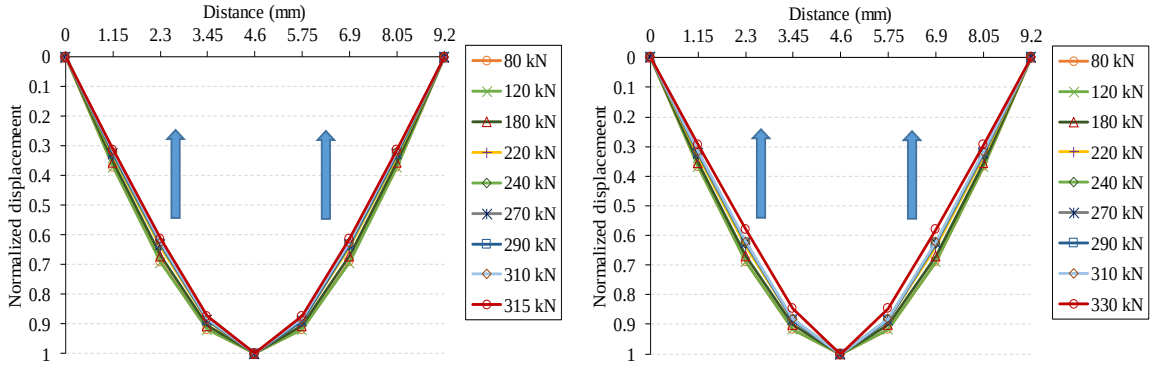


(a) Girder No.2 (b) Girder No.3

*Figure 6.10 The normalized analytical deflection curves*

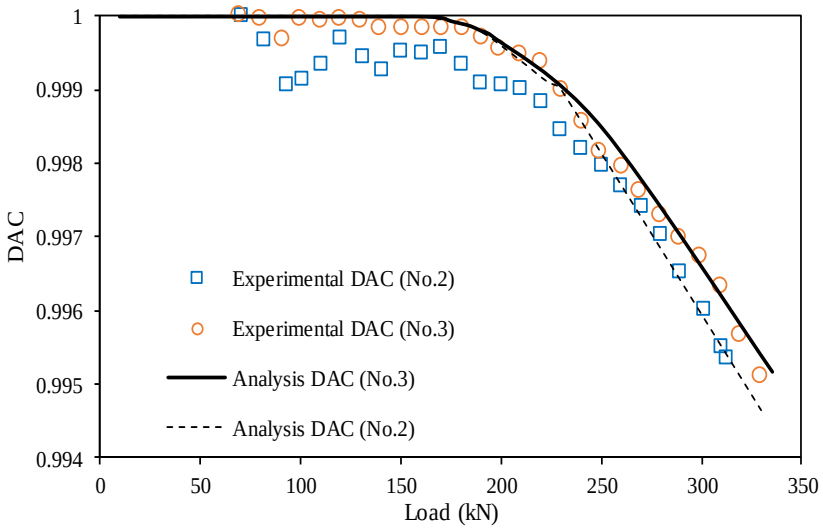


*Figure 6.11 Variation in DAC with respect to the increased loading*

## 6.4 Threshold for DAC variation

The results of the DAC calculation from the numerical simulation results and the experimental results of the destructive loading test showed the whole change in the DAC value from the time of soundness to the time when the critical load damaged the girders. In the elastic phase, the DAC value was almost equal to unity, then decreased as the cracks appeared. Moreover, after a gradual decrease to approximately 0.9985, the value of the DAC dropped sharply until the structure was damaged (see **Fig. 6.11**). As mentioned earlier, this study aims to propose a limit value for the reduction of the DAC. From the obtained results on both experimental and analytical examinations, the DAC value of 0.9985 is considered and proposed as the initial value for the limit for the reduction of the DAC in this study. If a structure performs a lower value of DAC than 0.9985, the system will give warnings about the health of that structure. In the future, further studies about DAC need to be implemented in practice in order to produce the most accurate threshold value for DAC index. From now on, by using the DAC value obtained from the loading test as the threshold value (such as 0.9985), there is a possibility that the proposed method that can express change of displacement shape due to change of rigidity as one numerical value and find abnormal value.

## 6.5 Conclusions

This study proposed the displacement assurance criterion (DAC) method that can represent the change in rigidity of a structure by one numerical value. In this chapter, attempts have been made to utilize Displacement Assurance Criterion (DAC) proposed in **Chapter 3** on practical cases. Therefore, destructive tests on the PC girders were carried out to evaluate the feasibility of DAC approach on damage detection by analyzing the displacement curves obtained from the experiments. The main conclusions drawn from this chapter are as follows.

- ✓ Regarding the results of loading tests, girder No. 3 had a better correlation degree of displacement curves among loading states by comparing with girder No. 2. Therefore, it was cleared that there was a correlation between the variation of DAC and damage states. Besides, it can be asserted that the numerical models provided reasonable results on the ultimate strength behavior of the specimen and reproduced the variation in DAC owing to the applied loads, and was useful for further parametric analyses. Therefore, DAC can be proposed as an index to figure out the occurrence of damage and more studies should be conducted to apply this indicator in practice.
- ✓ Furthermore, it is possible to utilize displacement curves as the input for DAC calculation to identify the occurrence of damage. From now on, by employing the DAC value obtained by the loading test as the threshold value (such as 0.9985), there is a

possibility that the proposed method that can express change of displacement shape due to change of rigidity as one numerical value and find abnormal value.

- ✓ In the future, further studies about DAC need to be implemented in practice in order to produce the most accurate threshold value for DAC index.

## 6.6 References

[1] Y. Hiroi, T. Yamamoto, Y. Toda, H. Manabe, and T. Miyagawa, "Experimental and analytical studies on flexural behaviour of post-tensioned concrete beam specimen deteriorated by alkali-silica reaction (ASR)," in *15th International Conference on Alkali-Aggregate Reaction*, 2016.

[2] Tnodiana.com, "User's manual of FX+ for DIANA version 9.6." [Online]. Available: https://support.tnodiana.com/manuals/d96/Diana.html. [Accessed: 01-Jul-2016].

[3] Japan Society of Civil Engineers Concrete Committee, *Standard specifications for concrete structures: design code*. Concrete committee, 2012.

# Chapter | 7

# Conclusions

Among difference approaches developed for structural damage detection, changes in the measures static parameters have shown promise for identifying the occurrence and location of structural damage. With the aim of contributing to efficient structural health monitoring approaches, this study focused on experimental and numerical examples of using only displacement data for structural damage detection. The approach was exclusively based on the correlation between two displacement curves which can be obtained rapidly on site by inexpensive tools of measurement. Specifically, two new damage indicators—displacement assurance criterion (DAC) and displacement based index (DBI)—were introduced and employed in numerous scenarios to determine damage properties. The outcome of numerical studies revealed that the DAC value decreased with the increasing structural damage and DBI could point out the locations of simulated damage. Therefore, DAC can be utilized as an indicator of the presence of structural degradation and DBI can be employed for damage localization. For the kind of structures analyzed, their performance has shown that they are potentially useful. From the theoretical standpoint, the number of measurements does not play a major role in the change in DAC when there are more than seven observation points. Consequently, when considering the effectiveness and the economy of using the DAC coefficient to identify the occurrence of structural damage, the seven-point measuring system can provide relatively reasonable judgments. Besides, there is no correlation between the DBI values and the intensity of applied loads when using DBI as a damage localization approach. The limitation of the proposed approaches is that the input data needs to be determined with high accuracy. A sufficient number of points provides more accurate results than a rough measurement case. Moreover, regarding DBI, the most critical factors for determining damage location are the selection of observed points at or near the damage locations, and the accuracy of measurements. For preventing uncertainty in the results, this study suggests that the number of measures should be as fine as possible. At the moment, the DBI method is useful for damage detection only when the measurement noise is less than 0.1%. Therefore, the nodal displacement should be measured with high accuracy when using DBI for identifying structural deterioration.

Regarding actual examinations, this study constructed three full-size prestressed concrete (PC)

girders from the high-early-strength Portland cement and reactive aggregates, and then exposed them to outdoor environmental conditions. Two of the specimens were affected by the ASR whereas the third one was maintained at an inactive state by suppressing the acceleration of the ASR using the fly ash. Destructive loading tests on the PC girders were carried out to evaluate the feasibility of DAC approach on damage detection by analyzing the displacement curves obtained from the experiments. Specifically, during the destructive test of the PC girders presented in **Chapter 2**, the vertical displacement was measured at seven pointed on the lower extreme fiber for computing the deflection curve at each loading step. Then, the obtained curves were analyzed to estimate the variation in the DAC value. Regarding the results of loading tests, the girder with fly ash (girder No.3) had a better correlation degree of displacement curves among loading states by comparing with the girder without fly ash (girder No. 2). Therefore, it was cleared that there was a correlation between the variation of DAC and damage states. Besides, a nonlinear finite-element model of the PC girder was produced to verify the relation between the variations in DAC with respect to structural degradation owing to applied loads in practice. Validations of the numerical analyses against the results of loading test showed that the developed model offered reasonable simulations on the ultimate strength behavior of the bridge regarding load-carrying capacity, deflection response, and failure modes. Thus, numerical model can be appropriated not only as supplements to or substitutes for the full-scale test but also in parametric study and design. Besides, it can be asserted that the numerical models provided reasonable results on the variation in DAC owing to the applied loads, and was useful for further parametric analyses. Therefore, DAC can be proposed as an index to figure out the occurrence of damage and more studies should be conducted to apply this indicator in practice. From the obtained results of the numerical and experimental methods, this study proposes a threshold of DAC index for the sound structure. If a structure performs a higher value of DAC than the threshold, it can be judged as safety structure. Conversely, the system will give warnings about the health of that structure. From now on, by using the DAC value obtained by the loading test as the threshold value (such as 0.9985), there is a possibility that the proposed method can express change of displacement shape due to change of rigidity as one numerical value and find abnormal value. For long-term prospects, further studies about DAC need to be implemented in practical cases in order to obtain the suitable DAC threshold value for each kind of structure.

Besides, structural responses have been used as inputs in the evaluation procedures of civil structures for many years. Changes in environmental conditions also affect structural dynamic and static responses in a complicated manner. Indeed, apart from the degradation of a structure itself, changes in the environmental conditions alter its characteristics. For adequate maintenance, it is significant to quantify the environment-induced changes and discriminate them from the effects due to damage. Therefore, this study also aims to present preliminary

considerations for estimating the long-term behavior of ASR-affected structures and attempts to proposed recommendations about measurement noise when using structure responses as input for structural damage detection.

With regards to lab-scale efforts, this study investigated the combined effect of the changes in the environmental conditions and the ASR-induced deteriorations on the dynamic and static responses of the three PC girders, which were periodically tested for one and a half years. From the obtained results, the environmental conditions strongly affected the changes in the frequencies of the vibration modes of the girders because the correlation coefficients between the variables were high, as computed using the linear models. With regard to the relationship with the ambient temperature, the amplitude of the vibrational frequency decreased with respect to the increase in the ambient temperature. The correlation levels were comparatively moderate for the girders without fly ash (girders No.1 and No.2) but reasonably high for the girder with fly ash (girder No.3). With regard to the effect of humidity, relatively negative relationships between the measured frequencies and humidity were obtained. The ambient humidity affected the frequencies of the bending modes of girders No.1 and No.2 more significantly than those of girder No.3. The results of the error analysis show that the bending modes could be estimated more accurately than the torsional mode because the error ratio of the torsional mode was higher than that of the bending modes. The effects of the measured humidity and temperature on the changes in the damping ratio were negligible, though some outcomes illustrate that the damping ratios decreased relatively with the increase in the environmental parameters. The results also proved that the ambient temperature and humidity affected the entire girder uniformly, and consequently, the effects of the environmental conditions on the MAC values were not meaningful. A finite element model was proposed for numerical verification, the results of which were in good agreement with the measured changes in the natural frequencies. During the monitoring period, the bending modal frequencies of girder No.3 fluctuated in the range of ~3–5%, which is considerable compared to those due to structural damage. Hence, the effects of the environmental conditions should be examined thoroughly when using the variation in the vibrational frequency to assess the health of structures. Regarding the effects of environmental conditions on the static responses of the PC girders, daily and seasonal variations in ambient temperature led to changes in the camber of the girders. All values measured from displacement meters have positive correlations with temperature. In other words, the amplitude of the camber increased with respect to the increase in the ambient temperature. The measured camber of girder No.1 increase by ~0.21 mm – ~0.41 mm when ambient temperature increases by one degree, this variation of girder No.3 was observed as ~0.23 mm – ~0.5 mm. Approximately ~81% – ~93% of measured displacement could be accounted for by measured temperature. As another result, the camber can be related to temperature gradient using analytical or empirical methods. This conclusion allows camber to be approximated using only temperature data. In

this study, cambers in PC girders were accurately modeled and predicted in finite element simulations. The obtained results in both dynamic and static responses should be considered in structural damage detection using changes in structural responses in practice because the environmental conditions might cause unexpected errors in measured responses in the measurement field.

Towards the sustainable development of structures in the Hokuriku region, another concern of the present study was the possibility of applying fly ash to the PC girders deteriorated by ASR to increase their service lives. After one and a half year of monitoring of cracks, an addition of fly ash played a significant role in mitigating the cracks caused by the expansion due to ASR. From observation results of cut cross-section after the loading test, the depth of ASR-induced cracks along the girder-axis direction varied from 5 to 20 mm on the side surfaces and the top surface. However, no crack was found out in the area surrounded by stirrups, and no breaking of tendons was confirmed. An increase of convex curvature (up to ~13 mm) was observed in the girder without fly ash. Meanwhile, almost no change in convex curvature over time was found in the specimen mixed with fly ash. As an attractive outcome, an addition amount of fly ash did not only increase the load bearing capacity by nearly 5% but also enhance the initial bending stiffness of the objective PC girder by 10% after more than one year under ASR deteriorations. Therefore, from results of the long-term exposure and the tests, the flexural strength and the rigidity of the specimen with fly ash were not degraded while ASR was also suppressed efficiently. In addition, the outcomes of the comparison between the three girders show that the differences in the measured frequencies of the three girders manifested clearly over time regarding the two bending modes, whereas no significant deviation was observed for the frequencies of the torsional mode. In particular, the bending frequencies of the girder with fly ash were higher than those of the girders without fly ash at each measuring time. With regard to the damping ratio, similar observations were made. Although no significant difference in the amplitude of the torsional mode was obtained, the damping ratios of the other modes changed considerably. Within one and a half years of investigation, the damping ratio of girder No.3 was found to be lower than that of the other girders. Besides, the static behaviors of the girders were observed to be quite different in this study. Because the dynamic and static behaviors of the three girders were observed to be different, the fly ash significantly affected the performances of the PC girders under the ASR damage. As another investigation, cylindrical concrete cores were taken at various positions of the girders to analyze the relationship between mechanical properties of concrete such as compressive strength, static elastic modulus, and ultrasonic wave propagation speed. Proportional correlations between the compressive strength, the static elastic modulus and the ultrasonic propagation velocity of the core were found. Moreover, the mechanical properties of concrete cores varied according to their collecting positions and directions. Therefore, when assessing the load-carrying capacity and mechanical properties of

PC girder under ASR deterioration, it is necessary to make appropriate corrections according to the confinement degree due to prestressing instead of using measured values of the concrete core as they are.

As a final remark, structural health monitoring has a strong similarity exists between it and medical activity. Structures instrumented with sensors and equipped with a central processor were compared to the nervous system of living beings. After detection of the damage by the sensors embedded in the structure, the central processor can build a diagnosis and a prognosis and decide of the actions to undertake. Today, the development of damage detection methods in civil engineering structures is one of the most pressing issues. However, structural characteristics are unavoidably affected by environmental factors, particularly temperature load, during long-term structural monitoring. The emphasis here is that “A miss is as good as a mile.” If the evaluation system gives a false diagnosis about structural health, it will cause unpredictable consequences. Therefore, to provide an effective and accurate determination of the structure, it is crucial to quantify the environment-induced noises and discriminate them from the effects due to damage. This study is a start point for two simple damage identification based on only displacement curve evaluation, and further research is needed on the subject. Regarding long-term prospects, further research should be carried out to enhance the accuracy of DAC and DBI in actual situations, and future projects can target improvements in relation to dynamic strain and displacement influence lines.

# Acknowledgements

Three and a half years have passed since I entered Kanazawa University with the desire to become a lecturer at a university, and finally, I am able to summarize my work in this dissertation. It is not such a long time; however, it is enough to familiarize me with the academic environment and colleagues and to make me fascinated with research themes of the structural laboratory. With this acknowledgment, I would like to express the deepest appreciation and honest gratitude to my academic supervisor, Professor Fukada Saiji, for his guidance, unconditional help, and visions which strongly inspired and encouraged me to overcome obstacles and to reach the outcome of the doctoral course. His thoughtful recommendations and advice are precious things that will stay with me throughout my future career. I am also grateful to Professor Maegawa Koji, Professor Torii Kazuyuki, Professor Masuya Hiroshi, whose expertise, understanding, generous guidance and supports made it possible for me to be a student of Kanazawa University and to work on my desired aspect. Honestly, I greatly appreciate not only valuable opportunities which Fukada sensei, Maegawa sensei, Torii sensei, Masuya sensei have so kindly given to me but also encouragements and advice whenever I have troubles in both study and daily life. Moreover, I would like to express my sincere gratitude to Associate Professor Yamamoto of Kyoto University for valuable advice and guidance for technical improvement of my dissertation. I am extremely fortunate to have got this all long the completion of my work.

I would like to express my great thanks to the Japanese government, SIP project and Kanazawa University for providing financial supports throughout my study as a master student and a doctoral student at Kanazawa University. It is also my duty to record my thankfulness to Mrs. Katayama, Mrs. Tanbo, Mr. Arima, Mr. Kobayashi, Mrs. Hasegawa for finding out time to reply my e-mails, for giving kind supports regarding the topic of my research and my daily life.

I acknowledge with thanks the kind supports which I have received from Mr. Yukio Abe, Mr. Mi Tetuo, and Vietnamese friends since I started a new life in Japan. I also express deep and sincere gratitude to my dear Japanese friends, my laboratory mates, my tutors (Ono-san, Koike-san, Uesugi-san) who always assist, answer my questions and help me whenever I have difficulty in Japan.

Finally, I take this opportunity to express my great appreciation and respect to my lovely parents, my younger sister, my beloved wife and my daughter for giving me moral supports, unconditional loves, patience, encouragements, inspirations which motivate me to continue my study.